A Handheld Bias-Switchable Top-Orthogonal-to-Bottom Electrode (TOBE) 2D Array for Ultrasound and Photoacoustic Applications

by

Mohammad Rahim Sobhani

A thesis submitted in partial fulfillment of the requirements for the degree of

Doctor of Philosophy

in

Microsystems and Nanodevices

Department of Electrical and Computer Engineering
University of Alberta

Abstract

Ultrasound imaging is a noninvasive and widely utilized technique for soft tissue imaging in various medical diagnostic and treatment applications. However, conventional ultrasound machines face challenges regarding imaging speed and quality due to their small probe size, whereas a bigger probe requires many electrical channels for data acquisition and processing.

Deploying a fully-connected 2D array in ultrasound probes is critical for achieving high-quality 2D/3D ultrasound images. However, this approach becomes impractical when dealing with larger ultrasound arrays. On the other hand, the acquisition and processing of data with a higher number of channels result in a reduction in imaging speed. Numerous strategies have been developed to address this issue, employing multiplexing techniques to limit the number of active elements on arrays. Nevertheless, these methods still suffer from lower signal-to-noise ratios (SNR) compared to fully connected arrays, leading to smaller aperture sizes and, consequently, restricted spatial resolution.

This doctoral dissertation endeavors to overcome these limitations by pioneering the fabrication of unprecedented large bias-sensitive arrays. The focus is on top-orthogonal-to-bottom electrode (TOBE) arrays, also called row-column arrays, which have demonstrated significant potential as an alternative to fully-wired 2D arrays. They offer a substantial reduction in the number of channels required. Previous research has shown that innovative imaging techniques involving bias-switchable TOBE arrays hold promise compared to earlier non-bias-switchable row-column imaging methods and existing Explososcan approaches. However, they often relied on

extensive coherent compounding.

In this work, along with TOBE array fabrication, we introduce "Ultra-Fast Orthogonal Row-Column Electronic Scanning" (uFORCES), an ultrafast coded synthetic aperture imaging method. Unlike its FORCES precursor, uFORCES can achieve coherent compounding with only a few transmit events, potentially making it more robust in the presence of tissue motion. We demonstrate that uFORCES has the potential to offer enhanced resolution when compared to Matrix probes with beamformers constrained by paraxial approximation. Additionally, unlike current Matrix probe technology incorporating microbeamforming, uFORCES enables ultrafast imaging at speeds of thousands of frames per second using only row- and column-based addressing when coupled with bias-switchable TOBE arrays.

A hand-held form factor of the TOBE array has been developed and successfully tested on cyst phantom targets, and the results are compared with commercial ultrasound machines. Also, the feasibility of fabricating a transparent/translucent variant of the TOBE array has been briefly investigated, along with reporting some preliminary through-illumination photoacoustic imaging from crossed gold wires. This bias-switchable TOBE innovation promises to significantly improve ultrasound imaging systems' efficiency and image quality.

Preface

This thesis is a combination of original work by Mohammad Rahim Sobhani as well as previously published works. Chapters 3 and 4 consist of peer-reviewed research publications by M. Rahim Sobhani et al. titled “Bias-sensitive transparent single-element ultrasound transducers using hot-pressed PMN-PT” and ”Ultrafast Orthogonal Row–Column Electronic Scanning (uFORCES) With Bias-Switchable Top-Orthogonal-to-Bottom Electrode 2-D Arrays”.

Chapter 5 consists of a conference proceeding and presentation titled ”Bias-Sensitive 128x128 hand-held TOBE ultrasound probe based on electrostrictive PMN-PT for photoacoustic applications” and presented in IEEE IUS 2022 and SPIE ECBO 2023.

Chapter 6 summarizes developments in the handheld TOBE array fabrication, characterization, and imaging performance comparison with the commercial ultrasound probes. This chapter was partially presented in IEEE IUS 2022 and 2023. The related presentation in IEEE IUS 2023 was selected as a finalist in the best student paper competition.

And finally, Chapter 7 was partially presented in IEEE IUS 2021.

Acknowledgements

As always, I praise almighty God for the given health, knowledge, and family and for coming to me in the coldest moments during this long journey.

First and foremost, I'd like to express my deep gratitude to my supervisor, Dr. Roger Zemp, for his invaluable guidance and never-ending support. I will never forget when he replied to my email and accepted me as a Ph.D. student in his fantastic group.

I'm deeply grateful to the committee members, Dr. Vien Van and Dr. Mahdi Tavakoli, to the examiners, Dr. Jeremy Sit, Dr. Hyun-Joong Chung, Dr. Meng-Lin Li, to the committee chair, Dr. Jie Han, and to the research collaborator, Dr. Jeremy Brown, for providing valuable guidance and feedback, shaping the direction of my research and this dissertation.

I extend my heartfelt thanks to my lovely wife, Negar, for her unwavering support. She's been there through countless early mornings and late nights, even when it meant sacrificing our time together.

I also want to show my appreciation to my beautiful daughter, Serenay, who may one day read this dissertation when she grows up. Her endless questions and curiosity about my work, even when I was busy on my laptop, have been a constant source of motivation and joy.

I'd also like to thank my friends, colleagues, and nanoFAB's staff whose support, discussions, and shared experiences enriched my academic life. Lastly, my sincere thanks go to everyone who has shown kindness and support during this journey, both within and beyond the academic community. Your encouragement and belief in my work have been a constant source of motivation.

Table of Contents

List of Tables

List of Figures

Chapter 1

Introduction

In recent years, ultrasound imaging has grown considerably, driven by the need for increased resolution and deeper penetration capabilities. Conventional ultrasound technology has been key in diagnostics, primarily counting on linear and Matrix probes; however, they exhibit considerable limitations. Linear probes, characterized by their 1D smaller apertures, struggle with limited depth and resolution in image production. Their elevational focusing is only optimal at certain imaging depths defined by an acoustic lens. On the other hand, Matrix probes, despite their complex 2D array design and implementation of wide-beam walking aperture (WA) imaging schemes, face challenges in dynamic focusing capabilities due to their smaller active aperture sizes and used microbeamformers. Moreover, their fabrication, especially for larger 2D arrays, remains a complicated task.

In contrast, the proposed innovative bias-switchable TOBE array made from electrostrictive material, utilizing advanced aperture-encoded FORCES and uFORCES imaging schemes, marks a significant improvement. These imaging schemes enable full and sparse synthetic aperture imaging capabilities, preserving focus across the entire imaging plane during both the transmit and receive stages. This approach addresses the limitations of WA imaging schemes, which focus on a single depth at a time, providing a more detailed and uniform image across different depths.

1.1 Key Contributions

1.1.1 Bias-Sensitive Transparent Single-Element and TOBE Ultrasound Arrays on a Testbench

Transparent ultrasound transducers have emerged as a key innovation in biomedical applications, significantly improving the capabilities of photoacoustic imaging. These transducers allow light to pass through, enabling more effective imaging of biological tissues. The integration of bias-sensitivity into these transducers additionally grows their utility in biomedical applications, offering dynamic adjustment of sensitivity and the chance of utilizing aperture encoding.

In this thesis, we introduce an innovative bias-sensitive transparent/translucent ultrasound array composed of electrostrictive material. When polished perfectly on both sides, the investigated electrostrictive material (PMN38, TRS Technology) provides excellent transparency. This feature distinguishes it from capacitive micromachined ultrasound transducers (CMUTs), which, while transparent, have a different fabrication process and are cheaper to fabricate. Fabricating these electrostrictive materials shares similarities with the well-established process used for conventional piezoelectric (PZT) materials, making it a cost-effective alternative. Furthermore, these materials necessitate less complexity in the imaging system architecture with existing medical ultrasound diagnostic machines.

A notable part of this thesis revolves around developing and characterizing a novel transparent bias-sensitive single-element ultrasound transducer out of PMN38. This development marks a step forward in ultrasound technology, opening new avenues for through-illumination photoacoustic applications. Furthermore, the thesis reports the progress in developing a Top-Orthogonal-to-Bottom-Electrode (TOBE) array. The TOBE array, an advancement of the single-element transducer, incorporates aperture encoding, which allows for individual element readouts. This feature enhances the array's functionality, enabling 3D photoacoustic imaging.

1.1.2 An Ultrafast Aperture-Encoded Sparse Synthetic Aperture Imaging Technique

In recent years, the development and application of Top-Orthogonal-to-Bottom Electrode (TOBE) arrays, also known as Row-Column Arrays (RCAs), illustrate a significant advancement. These arrays have drawn more attention as a practicable alternative to the traditional fully-wired 2D arrays, primarily due to their capability to substantially reduce the needed electrical channels. This channel reduction directly improves the efficiency of the ultrasound machines and paves the way to high-speed imaging capabilities.

Introducing bias-switchable TOBE arrays has further enhanced the capabilities of these systems. Earlier research around bias-encoding imaging schemes has shown considerable promise, especially compared to non-bias-switchable row-column imaging techniques and existing Explososcan approaches [1, 2]. However, a limitation of these earlier approaches was the need for extensive coherent compounding to achieve high-quality images (FORCES), where for a 128×128 TOBE array, 128 transmit events are needed.

We introduce the Ultra-Fast Orthogonal Row-Column Electronic Scanning (uFORCES) imaging technique to address this challenge. This method is an ultrafast coded synthetic aperture imaging technique that develops the previous FORCES method. A key advancement with uFORCES is its ability to achieve coherent compounding with only a few transmit events, potentially making it more robust against tissue motion, a critical factor in medical imaging. In this thesis, through simulations, we have demonstrated that uFORCES might offer improved resolution compared to state-of-the-art Matrix probes, whose beamformers are limited by paraxial approximation. This potential for higher resolution is a significant step forward in ultrasound imaging technology, a marked improvement over current Matrix probe technology incorporating microbeamforming. More importantly, fabricating a high-frequency Matrix probe has its own challenges, where the implemented beamformer and electronics behind the array would generate more heat and degrade the image quality. In contrast, the proposed TOBE array can be easily fabricated at higher frequencies and is massively scalable to unprecedented large sizes.

1.1.3 A Handheld Bias-Sensitive Ultrasound TOBE Array

Although the fabrication process for making a TOBE array from electrostrictive materials has some similarities, it is still challenging to fabricate a large aperture handheld TOBE array. In this thesis, we have developed our unique fabrication process where the bulk PMN38 mounts on a custom rigid-flex PCB, adds some support to the TOBE array and provides electrical routing and connections. This innovative handheld probe addresses the limitations of traditional linear and Matrix ultrasound arrays, offering a superior alternative with its bias-switchable capabilities. Unlike linear arrays with limited depth and resolution due to smaller apertures and an acoustic lens optimal for only specific depths and Matrix probes constrained by their complex fabrication challenges and limited dynamic focusing capabilities, the fabricated bias-sensitive handheld TOBE probe shows superiority in both these areas.

The fabricated handheld TOBE probe utilizes advanced aperture-encoded FORCES and uFORCES imaging schemes, enabling comprehensive and uniform focusing across the imaging plane. This is a marked improvement over the single-depth focus limitation of wide-beam walking aperture (WA) imaging schemes used in traditional probes. Moreover, the TOBE probe offers adjustable and steerable transmit beams in the elevational plane, providing two-way focusing capabilities that are impossible with the fixed acoustic lens of linear probes. Additionally, the design of the TOBE probe allows for larger apertures without sacrificing imaging speed or increasing cabling complexity, overcoming a significant challenge faced by traditional ultrasound imaging technologies. The fabricated prototype handheld TOBE probe represents a groundbreaking development in ultrasound imaging, paving the way for more efficient, high-resolution, and deep-penetrating diagnostic capabilities.

1.2 Thesis Outline

Chapter 2 of this thesis provides some background information on ultrasound transducers and commonly used commercial ultrasound probes and their imaging schemes, such as walking aperture and synthetic aperture. Also, different strategies for 3D ultrasound imaging are summarized, as well as their advantages and disadvantages.

Chapter 3 of this thesis describes the feasibility of fabricating a bias-sensitive transparent single-element transducer from electrostrictive material (PMN-PT or PMN38). Characterization and the simple through-illumination photoacoustic imaging results are shown here.

Chapter 4 introduces the Ultrafast Orthogonal Row-Column Electronic Scanning (uFORCES) imaging scheme implemented on a TOBE array, and the results were compared with the state-of-the-art Matrix probes through simulations. Also, a fabrication of a 128×128 TOBE array on a testbench was reported with conducted simple resolution and cyst phantom imaging.

Chapter 5 shows the steps taken towards the fabrication of a transparent/translucent bias-sensitive TOBE array for through-illumination photoacoustic applications. This chapter shows the preliminary photoacoustic images of a crossed gold target and describes the challenges of such a transparent TOBE array made of electrostrictive PMN38.

Chapter 6 of this thesis describes the progress on fabricating a handheld form of the factor for opaque bias-sensitive TOBE arrays for ultrasound applications. FORCES imaging scheme was implemented on the fabricated handheld TOBE array. The results showed outperforming performance compared to the commercial linear and Matrix probes, as we showed them through simulations in Chapter 4.

Finally, chapter 7 of this thesis concludes the thesis and provides some suggestions through numerical simulations for future works to further improve the performance of the TOBE arrays.

Chapter 2

Background

Ultrasound imaging is a noninvasive imaging technique that utilizes Megahertz range ultrasound waves for soft tissue imaging with many medical diagnosis and treatment applications. However, ultrasound imaging machines suffer from low framerate imaging and are expensive, bulky devices due to their fully-connected probes with many electrical channels required for data acquisition and processing. An ultrasound probe with a fully-connected 2D array is essential to obtain high-quality 3D ultrasound images. However, it becomes impractical for a broader array. On the other hand, acquiring the data and processing time for larger channel counts drops the imaging framerate. Many approaches have been made to decrease the channel counts by multiplexing techniques, limiting the number of active elements on arrays [3–6]. However, they still suffer from lower SNR than fully-connected arrays and smaller aperture sizes, limiting their spatial resolution. This thesis addresses these limitations by fabricating the 128×128 bias-sensitive arrays. A novel imaging technique has been developed to improve the frame rate further, while the results are comparable with state-of-the-art MATRIX probes in terms of resolution and signal-to-noise ratio.

2.1 Ultrasound Imaging and Beam Forming

Ultrasound imaging utilizes non-ionizing acoustic waves for medical diagnosis and treatments in the range of 20 kilohertz to up to a couple of hundred megahertz. These imaging techniques are safer, cheaper, and faster than X-ray and magnetic resonance imaging (MRI). In principle, an ultrasound imaging machine calculates the round trip time of the flying acoustic waves (transmitted and received) to form an image from a region of interest in the body. This is accomplished by getting the scattered acoustic waves from different tissues with different acoustic impedances. The axial resolution of an ultrasound probe depends on the transducers' center frequency and their fractional bandwidth. However, for a wide bandwidth transducer, the axial resolution can be approximated as 2λ, where λ is the wavelength of ultrasound used. The higher the operating frequency, the higher the axial resolution, the higher the attenuation, and the lower the depth of imaging.

A single-element transducer can only be used for A-mode (Amplitude) scanning without lateral resolution. This scanning mode (single transducer) can be combined with a focus rastering light beam to form photoacoustic microscopy (PAM). A single-element transducer can also be mechanically scanned to create a 2D image. However, mechanical translational scanning is slow, so the typical ultrasound probes usually use an array of single elements. The array's elements allow for resolution to be obtained in a lateral direction. The lateral resolution can be approximated by $1.4\ \lambda\ \mathrm{F}\ /\ \mathrm{D}$, where F and D are the focal distance and the aperture size, respectively. F/D is also known as the f-number.

In order to reconstruct a 2D image (B-mode scanning), the time-of-flight needs to be calculated for an acoustic signal transmitted from each element to a desired spatial location and way back to each element on the receiving side. This process is known as beamforming, with a standard algorithm of delay-and-sum (DAS) [7]. In this beamforming method, the value of each pixel is obtained by summing the signals received on all the elements on an array with applied delays corresponding to the pixel's spatial location. A transmitted beam can also be steered or focused in the same way by adding delays to each element on the transmit side. An ultrasound array should generally have a higher operational frequency with a large aperture size for a finer lateral resolution. Higher frequency arrays require smaller pitch sizes to suppress the side lobes, and the larger aperture requires more elements together [8]. These lead to having more active elements on a linear array probe, which requires more active front-end electronics. Considering these roles makes the fabrication more challenging for a 2D array, with the number of functional elements of N^2 for an N by N array.

2.1.1 Conventional Ultrasound Linear Array

Conventional ultrasound machines usually provide 2D ultrasound images (B-scan mode). For this purpose, the commercial ultrasound probes are primarily fabricated in a linear fashion where long single elements are placed beside each other in the azimuth plane. To deliver higher ultrasound energy into the body at specific depths, an acoustic lens is fabricated on the surface of the linear array. The ultrasound lens provides a fixed elevational focus to the arrays, as shown in Fig. 2.1. The operational frequency, size of the array, and the elevation focusing (f-number in elevation) are mostly application-specific. One of the limitations of linear arrays is being stuck to a fixed focus on the elevational plane.

2.1.2 Walking Aperture Imaging

The Walking Aperture (WA) imaging scheme is the most used imaging scheme on commercial ultrasound machines. The WA imaging method aims to improve the lateral resolution and signal-to-noise ratio (SNR) in ultrasound imaging with better contrast. This technique involves the dynamic selection and activation of transducer elements in a linear array to form the transmitted and received ultrasound beams. Unlike conventional imaging, where all the elements are used for every transmission, the Walking Aperture Technique ”walks” along the array, activating a subset of elements for each transmission, as shown in Fig. 2.2.

The selected subset of elements forms an aperture that moves or ”walks” along

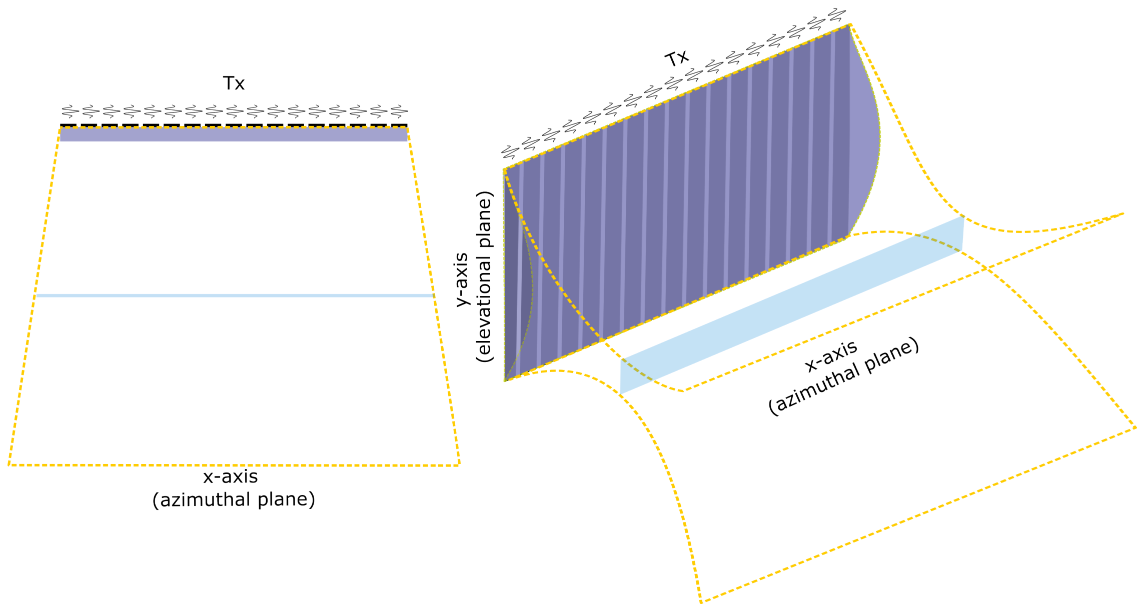

Figure 2.1: Schematic of a linear array with an acoustic lens.

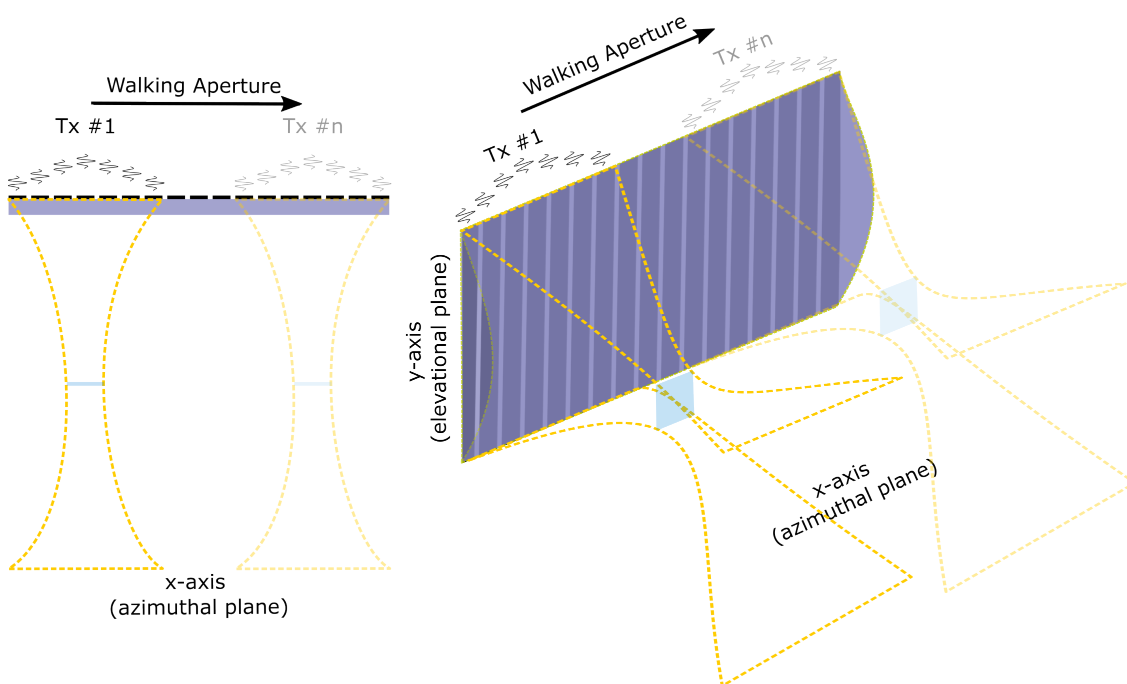

Figure 2.2: Schematic of the Walking Aperture (WA) imaging scheme implemented on a linear array.

the array, transmitting ultrasound pulses and receiving the echoes. The received signals are then coherently combined to form the image. This dynamic aperture selection ensures that the transmitted and received beams are optimally focused, enhancing image quality. This selective engagement of elements results in varying aperture configurations during the scanning process, which is designed to concentrate the ultrasound beam more precisely on the area of interest and improve the SNR. The improved SNR is a result of enhancing the signal strength relative to the noise with a focused beam in the azimuthal plane and a fixed acoustic lens in the elevation plane. Unlike the synthetic aperture, the image is usually good only in the focal zone.

To implement the Walking Aperture Technique, the ultrasound system's beamforming algorithms dynamically select a subset of adjacent elements to form the aperture for each transmission. The size and position of the aperture are adjusted for each transmission to optimize the beam characteristics. The lateral focusing depends on the size of the active aperture.

The finer pitch size on the linear array allows for fine adjustments in aperture size and position, resulting in improved lateral resolution and image quality. However, there is a trade-off between imaging frame rate and acceptable lateral resolution. So, scanning through the image plane with a finer lateral resolution will require more transmit events to cover the entire image, resulting in a lower frame rate. The frame rate of commercial ultrasound machines is usually less than 70 fps.

2.1.3 Synthetic Aperture Imaging

Synthetic Aperture Imaging (SAI) is a sophisticated technique in ultrasound imaging that aims to enhance image resolution and quality, especially in medical and industrial applications. This technique emulates a larger aperture by synthesizing data from multiple transducer positions, thus providing finer details and improved image clarity. The basic principle of Synthetic Aperture Imaging involves the sequential transmission and reception of ultrasound waves from an array of transducer

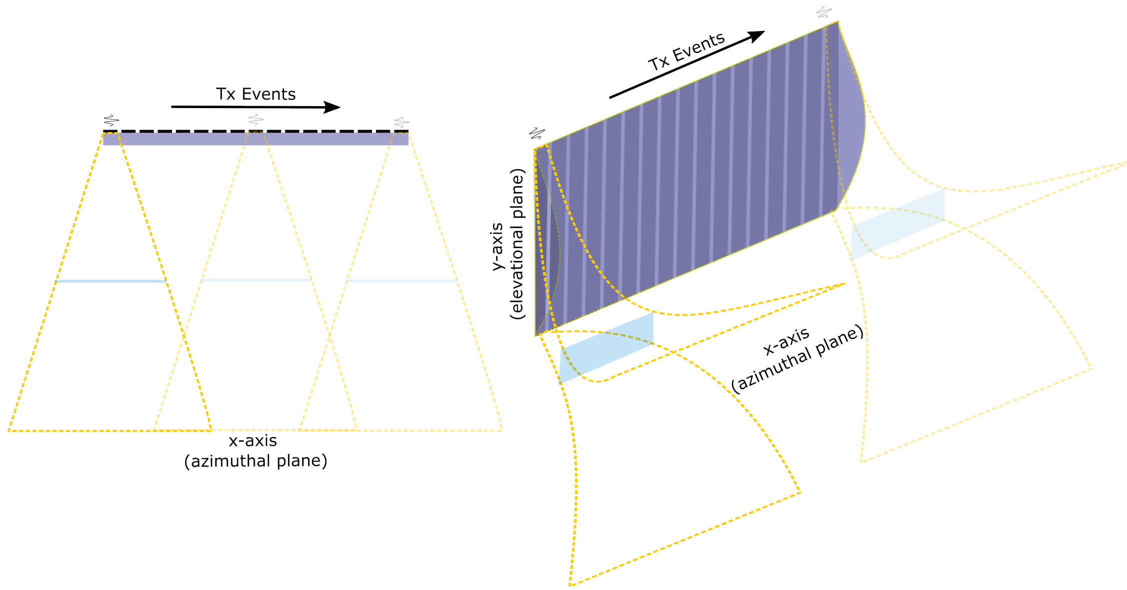

Figure 2.3: Schematic of the Synthetic Aperture Imaging (SAI) scheme implemented on a linear array.

elements. Unlike conventional imaging, where each element transmits and receives signals independently, SAI combines data from multiple transducer positions. The process involves transmitting a beam from each transducer element (usually with an elevational focusing using a fixed acoustic lens), receiving the backscattered signals on all elements, and then combining these signals coherently. Fig. 2.3 illustrates the schematic of SAI implemented on a linear array with an acoustic lens.

The combination of signals is a critical step that requires precise synchronization and alignment of the data. The synthesized aperture results in narrower main lobes and reduced side lobes, leading to improved lateral resolution and reduced artifacts in the final image. In other words, for a 2D image obtained by SAI, everywhere in the image is in azimuthal focus during the transmit and receive. Hence, higher-quality images are obtained compared to the walking aperture imaging scheme (WA). However, the acoustic energy is not focused everywhere in the elevational plane except at the focal zone defined by the acoustic lens. This is one of the limitations of the linear array, that the elevational focusing can not be changed.

In medical ultrasound, SAI is used to obtain high-resolution images of internal organs and tissues, facilitating accurate diagnosis and monitoring of diseases. One application of the SA can be in cardiology, where high-resolution images of the heart and surrounding blood vessels are essential for assessing cardiac function and detecting abnormalities. However, the imaging frame rate should be fast enough not to get any effects from the beating heart, where coherency of the received signals is essential.

Additionally, SAI has the capability to provide images with a uniform resolution throughout the field of view, unlike conventional imaging, which may suffer from resolution degradation at deeper regions and far from the focal zone. Furthermore, Synthetic Aperture Imaging allows for the use of smaller transducer arrays without compromising image quality. This is particularly advantageous in applications with space constraints, as it enables the development of compact and portable ultrasound systems.

Despite its numerous advantages, the SA technique requires precise synchronization and alignment of the received signals, which can be complex and computationally intensive. In addition, the quality of the synthesized image is highly dependent on the accuracy of the beamforming algorithms used. Errors in the algorithms can result in image artifacts and degradation of image quality. Moreover, the motion of the target or the transducer during the imaging process can also introduce errors and artifacts, necessitating the development of high-frame-rate imaging machines, which is a part of this thesis.

2.2 3D Ultrasound Imaging

3D ultrasound imaging is essential in some applications where the size and location of biological organs or cysts are a matter of surgery or therapy. Unlike 2D imaging (B-mode), where a linear array is required, 3D imaging can be done in a few ways, as described. Despite the great possible applications for 3D ultrasound imaging, clinicians usually don't prefer to use it as the current 3D imaging techniques and equipment have a slow frame rate and lower quality.

2.2.1 Mechanically-Scanned 1D Array

A 1D array can be mechanically swept to acquire multiple slices to form a volumetric (3D) image, as shown in Fig. 2.4 (a) and (b), for a linear translation and rotation, respectively. It can be done by manually scanning the array or using fixed motors [9–12]. Although a high-frequency large 1D array can be used to get high-resolution images, the imaging can be slow and may contain more imaging artifacts due to the probe's movement. The commercially available 3D probes often use this method to create a volumetric image.

2.2.2 2D Fully-Wired Array

Unlike the 1D arrays, where the elements are distributed in one direction, the 2D arrays are composed of elements distributed in two directions. Fabrication of such 2D arrays is more challenging because of the higher density of the active elements, more complex front-end electronics, and wire bonding issues. Although fully wired (fully connected) arrays can provide idealistic image quality in 2D and 3D, they become impractical for a large aperture array where the number of active elements is N^2 for an N by N array. A few approaches have been made to reduce the channel count, such as multiplexing, sparsely distributing the active elements, and Matrix probes with integrated microbeamformers. However, they usually suffer from a lower SNR and slow volumetric imaging frame rate [4, 13–15].

To the best knowledge of us, at the time of writing this thesis, a maximum of 32x32 fully-wired 2D arrays for a total of 1024 elements is available in the market from Vermon (Tour, France), which would require four Vantage256 ultrasound platforms (Verasonics Inc., USA) to be fully functional. However, such a fully connected 2D array has a small aperture size, limiting the penetration and lateral resolution. Fig. 2.5 (A) illustrates the schematic of a fully connected 2D array with 32×32 channels for a total of 1024 active elements.

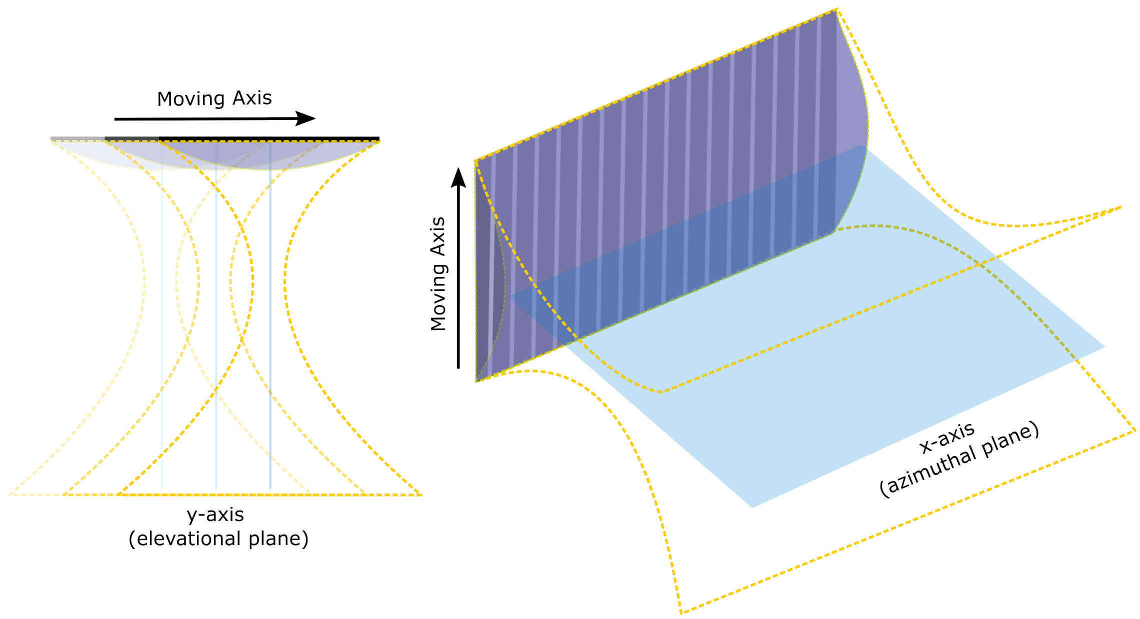

(a)

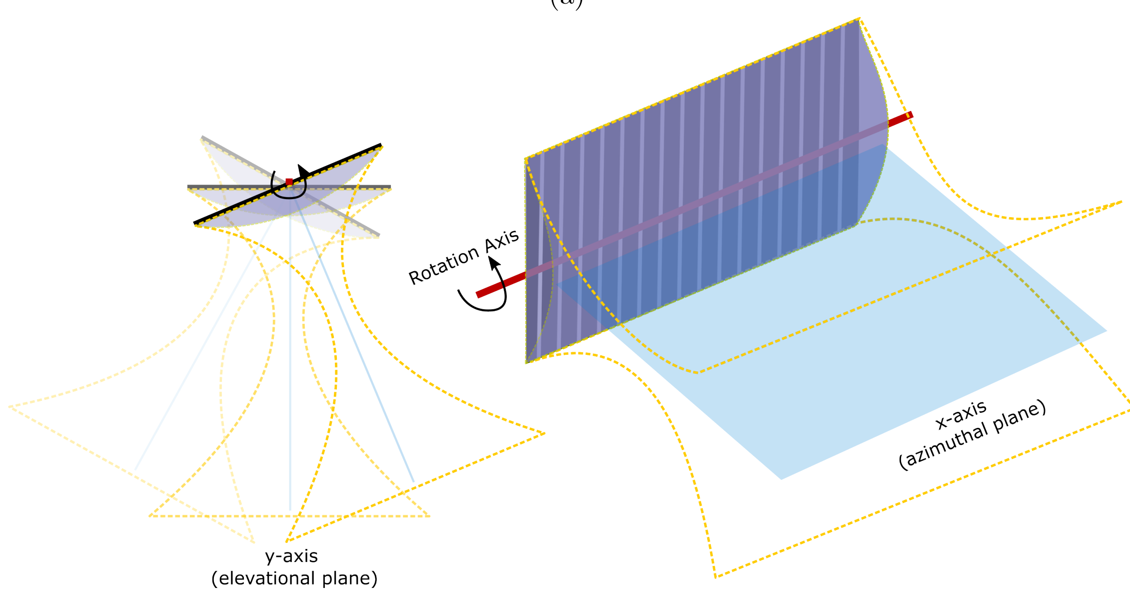

(b)

Figure 2.4: Schematic of 3D imaging with a linear array by (a) translating and (b) rotating the array.

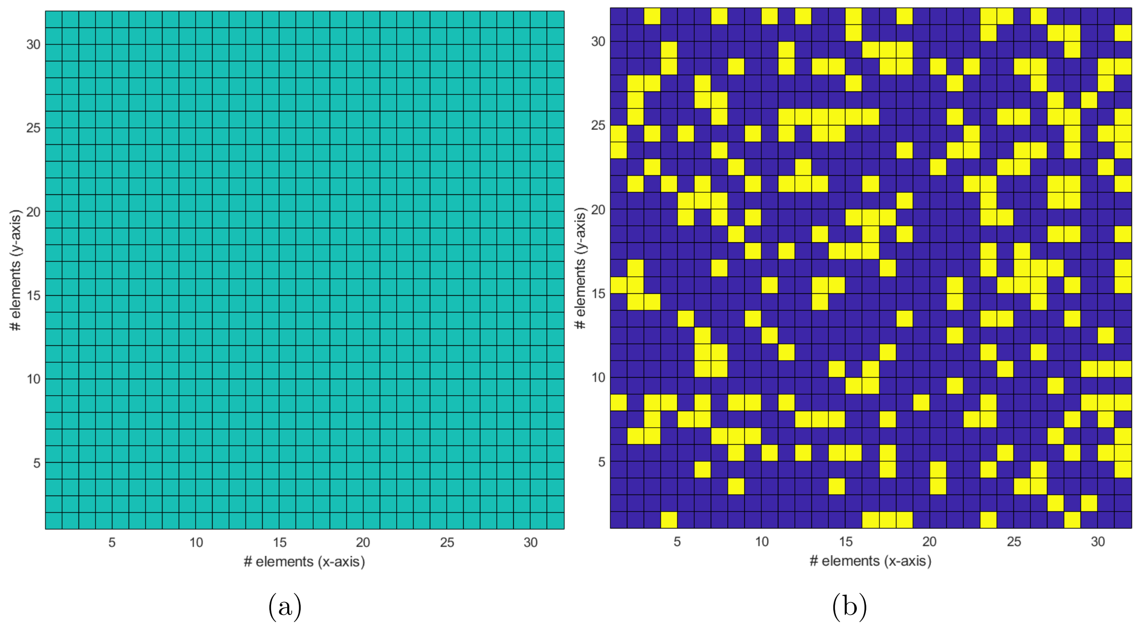

Figure 2.5: Schematic of 32×32 2D arrays in (a) fully-wired fashion with 1024 active elements, and (b) randomly distributed SPARSE fashion with a total of 256 active elements. The yellow elements are the chosen active elements.

2.2.3 Sparse Arrays

Sparse arrays are another form of 2D arrays developed to reduce the channel count and wiring complexity to fabricate bigger aperture sizes. This approach strategically distributes the active ultrasound elements on a 2D axis to reach the maximum possible image quality while minimizing the number of wiring and active transducers needed [15, 16]. This configuration can lead to cost-effective manufacturing and reduced system complexity with different implementation and optimization ways [17–27]. Fig.2.5 (b) demonstrates a sparse array with randomly distributed 256 active elements. In this figure, the elements are chosen randomly only for the purpose of the demonstration. The real sparse arrays distribute the active elements precisely in some patterns, which would result in improved spatial resolution.

Well-designed sparse arrays can achieve image quality comparable to fully connected 2D arrays, especially in applications where high resolution is not the primary concern, such as portable ultrasound probes. A few imaging topologies have been successfully developed and utilized on sparse arrays using focused or diverging beams [28]. The use of Artificial intelligence (AI) also have been reported to improve the image quality of sparse arrays [29]. However, they are limited by imaging artifacts and the limited signal-to-noise ratio (SNR), which may result in shallower penetration and imaging capabilities for some applications.

2.2.4 Microbeamformer-Based Matrix Arrays

Another approach to reducing the wiring complexity while having a bigger aperture with more active elements is the Matrix probes with embedded Application-Specific Integrated Circuits (ASIC), also known as microbeamformers. The state-of-the-art matrix probes have dramatically improved the image quality with the use of microbeamforming, involving pre-amplifiers, analog-to-digital converters, and delay-and-sum circuitry implemented as a custom integrated circuit beneath the shadow of each element with some examples here [30–34]. In microbeamforming, fine delays are introduced to elements before summing in groups, and coarse delays are implemented in the mainframe. Often, micro-beamformers implement tilt-only fine delays as a linear approximation to a quadratic delay profile. These approximations can be a source of image quality degradation, especially when using parallel beamforming to reconstruct a group of adjacent A-scan lines over a wide area, as ideal focal delays are accurate only for one line of sight. As a result, microbeamformer-based matrix probes may not necessarily provide the B-scan image quality. Also, Beyond image quality considerations, such micro beamforming-based matrix probes do not yet provide ultrafast imaging capabilities that are important for some applications such as ultrasensitive blood-flow tracking and super-resolution imaging.

Matrix probes with embedded microbeamformes are also limited by the paraxial approximation, which limits their dynamic focusing. In contrast, our proposed ultrafast imaging scheme implemented on the fabricated TOBE arrays shows some benefits of focusing the beam everywhere in the transmission and reception to obtain better

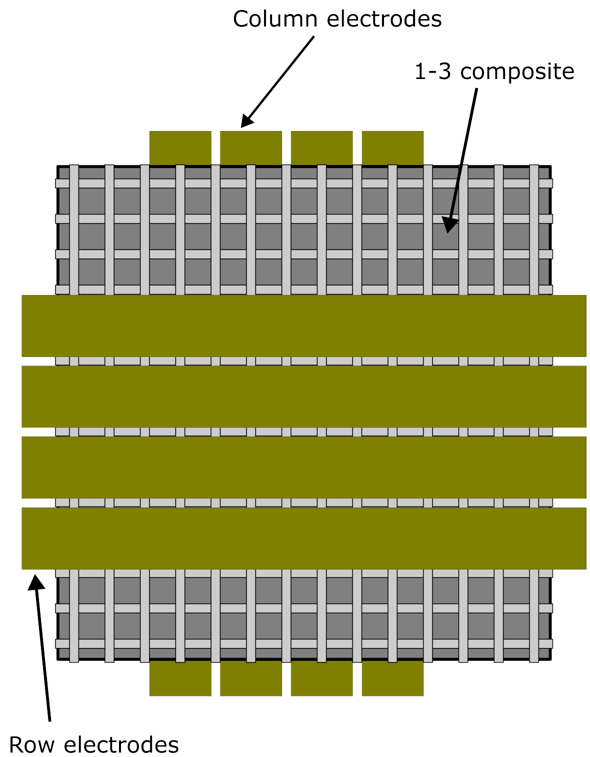

Figure 2.6: Schematic of a 4×4 TOBE array.

image quality.

2.2.5 Row-Column-Arrays (RCAs)

As mentioned before, a fully wired N×N 2D array would become impractical for large arrays. Top-orthogonal-to-bottom electrode (TOBE) arrays, also known as row-column-array (RCA), greatly reduce the number of active channels needed to acquire an image from N×N channels down to 2N. Fig. 2.6 shows a simplified schematic of a 4×4 TOBE array where 1-3 composite active material is sandwiched between rows and columns electrodes. RCAs were first introduced in [35], and have been developed over and utilized in ultrasound imaging in [36]. TOBE arrays were used to create volumetric images in [36–39] and with a solution for reducing the ghost artifacts [40], but still, they suffer from poor image quality owing to unfocused apertures on transmit or receive. In principle, images obtained by a TOBE array are similar to ones obtained by linear arrays in two orthogonal directions.

An approach has been made to improve the image quality by coherently compounding the multiple steered angles in two directions, but it suffered from asymmetric volumetric resolution and sidelobes [41]. However, the non-bias-switchable RCAs are limited to providing an image underneath the shadow of the array because of the way they use aperture on the transmission and reception [42]. The effect of acoustic lenses and transmitting diverging waves on the row-column arrays has been investigated to widen the field of view (FOV) with reported imaging artifacts and still lower SNR [39, 43–46].

The RCAs were first introduced and developed based on piezoelectric materials, then bias-sensitive CMUTs were used in the RCA fashion [47]. Later, a few novel approaches were introduced using bias switchable electrostrictive materials [1, 48]. later on, aperture encoding/decoding on the row and column have been investigated and introduced to improve the image quality and imaging frame rate [1, 2, 49–51]. However, the fabricated N×N arrays require N transmit events to acquire an ultrasound image which may become impractical for real-time applications where the tissue or organs move. This dissertation introduces the fabrication of a large 128×128 TOBE array with a precise fabrication method and a novel sparsely coded imaging scheme to increase the volumetric imaging frame rate and improve spatial resolution compared to the previously investigated 64×64 arrays.

2.3 Photoacoustic Imaging

Although optical imaging provides more contrast, it suffers from high scattering in biological tissues. On the other hand, a dense focused ultrasound probe can provide an excellent spatial resolution on the receiving side. Photoacoustic imaging is an imaging technique that combines the benefits of high optical contrast and high ultrasonic spatial resolution by exciting the tissues with short-pulse lasers and detecting ultrasound signals. Photoacoustic has many applications in the biomedical field, such as blood oxygenation measurement [52], vessel imaging [53], and optical contrast agents [54].

In practice, a transmitted short-pulse laser is absorbed by biological tissues and generates acoustic waves due to thermal expansion [55]. The quick impulse in pressure P_0 induced by optical absorption can be expressed as [56]:

$$P_0 = \left(\frac{\beta c^2}{C_p}\right) \mu_a \Phi \tag{2.1}$$

where β is the isobaric volume expansion coefficient, c is the speed of sound, C_p is the specific heat, μ_a is the absorption coefficient, and Φ is the light fluence.

Photoacoustic Microscopy (PAM) and Photoacoustic Tomography (PAT) are different techniques of photoacoustic imaging, each with unique approaches and applications. PAM, which usually uses a transparent single-element ultrasound transducer, leverages a focused laser beam through the transducer to achieve high spatial resolution imaging at superficial depths. This focused PAM approach allows detailed visualization of fine structures in biological tissues, such as small blood vessels in a mouse ear. The size of the illuminated laser spot primarily defines the resolution of PAM. A fine-focused laser beam is rastered on a biological tissue to form a C-scan image. Usually, the axial resolution of the ultrasound transducer is less important for the PAM as the laser's focal zone defines the depth of the imaging, and any reverberation inside the transducer (lower axial resolution) is less critical.

On the other hand, PAT utilizes broader illumination schemes, such as oblique illumination with fiber bundles to penetrate deeper into tissues, where an array of ultrasound transducers determines the spatial resolution. This technique is particularly useful for imaging deeper structures within biological tissues, such as breast cancer tumors in mice. Rather than focusing the laser beam as in PAM, PAT illuminates over a wider area, allowing for deeper tissue penetration. The spatial resolution in PAT is then defined by the ultrasound transducer or array used in the imaging setup.

In this thesis, we have shown the fabrication of a transparent single-element transducer that can be used for PAM applications where the non-ideal axial resolution wouldn't be a problem for a focused laser beam illuminating a desired depth. Also, we have developed a prototype transparent variant of the TOBE array for PAT applications and have shown some preliminary results with some suggestions to improve the bandwidth and transparency.

2.4 Bias-Sensitive PMN-PT Material

A piezoelectric material is polarized by applying an electric field at a high temperature. The polarization can stay still at an average operating temperature and voltages. The piezoelectric materials generate strains with an applied voltage across the poled domains and vice versa. Unlike the piezoelectric materials, the bias-sensitive ultrasound transducers show no piezoelectricity effect unless a DC bias voltage is applied. The capacitive micromachined ultrasound transducer (CMUT) is one of these bias-sensitive transducers, which uses electrostatic forces between two clamped plates to generate acoustics. However, the fabrication of these transducers is expensive and challenging.

This thesis focuses on the other materials known as electrostrictive materials, where the domains are unpolarized at room temperature. These materials can be temporarily polarized by applying a DC bias voltage. The biased electrostrictive material will then behave as a piezoelectric. In this thesis, we investigate the fabrication of transparent and non-transparent bias-sensitive ultrasound transducers based on PMN-PT, where the concentration of the PT is very low to hold any residual polarization. Also, bias-sensitive TOBE arrays allow for coding the aperture to address each column and row individually for the purpose of beamforming and image reconstruction as well as improving the SNR.

The electrostrictive PMN-PT material used in this thesis is PMN38 (from TRS Technology). The PMN38 poses optimum performance around 38 degrees Celsius, which is close to the body's temperature. Fig. 2.7 shows the parameters of the used PMN38 for different given electric fields. As shown in Fig. 2.7 (a), the material shows no piezoelectric effect without applied DC voltage. Also, from Fig. 2.7 (b) and (c), we can see that the PMN38 reaches the highest performance, around 4-5 kV/cm at room temperature. The density of the material is ~$7900 Kg/m^3$ with an acoustical impedance of ~35 MRayls. The graphs are taken from TRS technology website and the material's datasheet.

2.5 1-3 Composite and KLM Modeling

Unlike Finite Element Modeling (FEM), which computationally is extensive to investigate the behavior and design factors of an ultrasound probe, KLM modeling is a quick approach to speed up the design process by some approximations [57]. The KLM method numerically models the ultrasound transducers and mediums as electrical transmission lines, as a simple MATLAB script is provided in the Appendix based on [58–60]. The KLM model only considers the thickness mode resonance by assuming the active element area is much greater than the thickness. So, the acoustic waves only retain in one direction (thickness mode). The KLM model is useful for predicting the input impedance of a transducer and consequently estimating the resonance and anti-resonance frequencies, electromechanical coefficient (k_t), and electrical impedances for designing matching networks. It is also useful for predicting the transfer function of the transducer in pulse-echo mode with different mediums.

In this thesis, the fabrication of the TOBE arrays was started by modeling the behavior of the material in a 1-3 composite fashion using KLM modeling. A bulk PMN38 material has an acoustic impedance of up to 40 MRayl, which is very far from biological mediums' impedances (~1.5 MRayl). These huge acoustical mismatches cause multiple acoustic reflections inside the active material and limit the fractional bandwidth and then the axial resolution. Also, using a bulk material for making an array is inefficient as the electromechanical coefficient for PMN38 resonating in the thickness mode is around 55% in the best case, constrained by other resonance modes interfering with the desired resonating mode, as shown in Fig. 2.7(a).

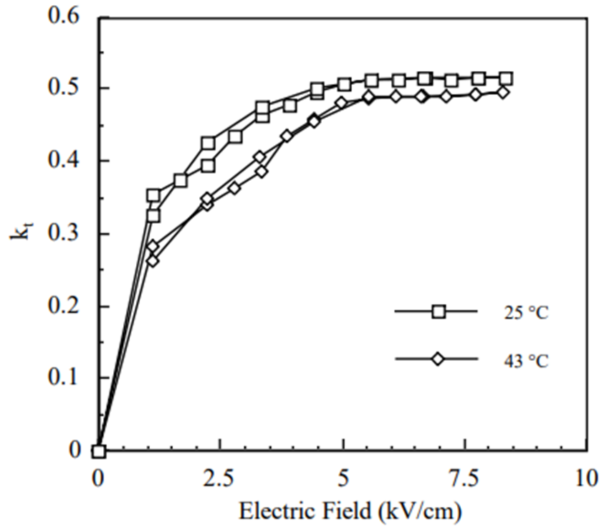

(a)

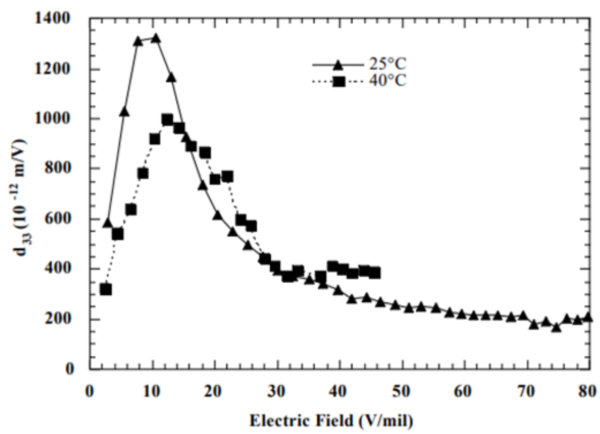

(b)

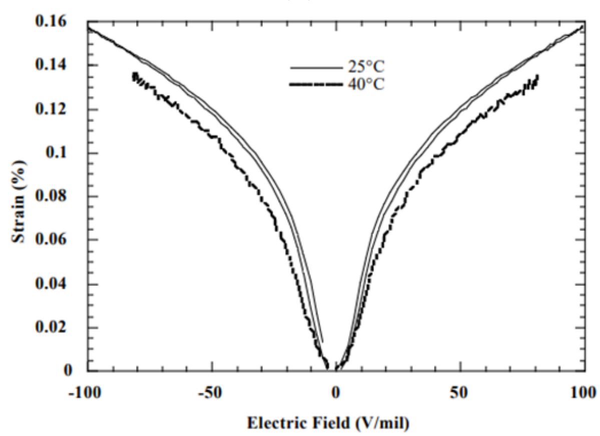

(c)

Figure 2.7: Properties of the electrostrictive PMN38 ; (a) electromechanical coefficient (k_t), (b) piezoelectric coefficient, and (c) strain versus applied electric field. Graphs are taken from the TRS technology website and PMN38 datasheet.

A solution for this problem is to make a 1-3 composite material with the bulk PMN38 and epoxy. As a result, the average acoustic impedance will be reasonably low to be matched with water (∼1.5 MRayl) by adding a matching layer. Also, the used epoxy will absorb the lateral mode resonances to improve the electromechanical coefficient of the array in thickness mode. Designing a 1-3 composite array requires many parameters of each component, such as stiffness matrix, dielectric constant, density, etc. Unfortunately, there are limited investigations done on the PMN38. Hence, the data provided by the companies is limited. So, a KLM model was first developed to predict the initial parameters of the bulk PMN38 material. This was done by measuring the input impedance of a thin bulk PMN38 material with metal pads on both sides. Then, the input impedance curve obtained from the KLM model was fitted on it to predict the parameters for the bulk PMN38. Two fabricated 1-3 composites are shown in Fig. 2.8 (a) and (b) with laser micromachining and dicing the bulk PMN38, respectively. After this step, materials are cleaned and filled with the epoxy301, followed by lapping and polishing.

The estimated parameters of the bulk PMN38, along with the parameters of Epoxy301 (Epotek) were used to extract the 1-3 composite parameters as described in [61, 62]. The estimated electromechanical coefficient (k_t), speed of sound, and the acoustic impedance of the 1-3 composite material based on the PMN38 fraction volume ratio are shown in Fig. 2.9. We have developed the fabrication process for the TOBE arrays by aiming to have a volume fraction of 50 to 70 percent. Another consideration in the transducer design is to ensure the lateral resonances formed in the width of the Epoxy and the active material's pillars are not interfering with the main frequency of the transducer. So, as per the rules of thumb, we have aimed to fabricate the transducer with a pillar size that has a ratio of thickness to width that is greater than at least 1.5 times. Also, the width of the cut is small enough, so the lateral resonance formed in the filled Epoxy has a frequency at least 2 times greater than the transducer's center frequency. By considering all of these design rules, we

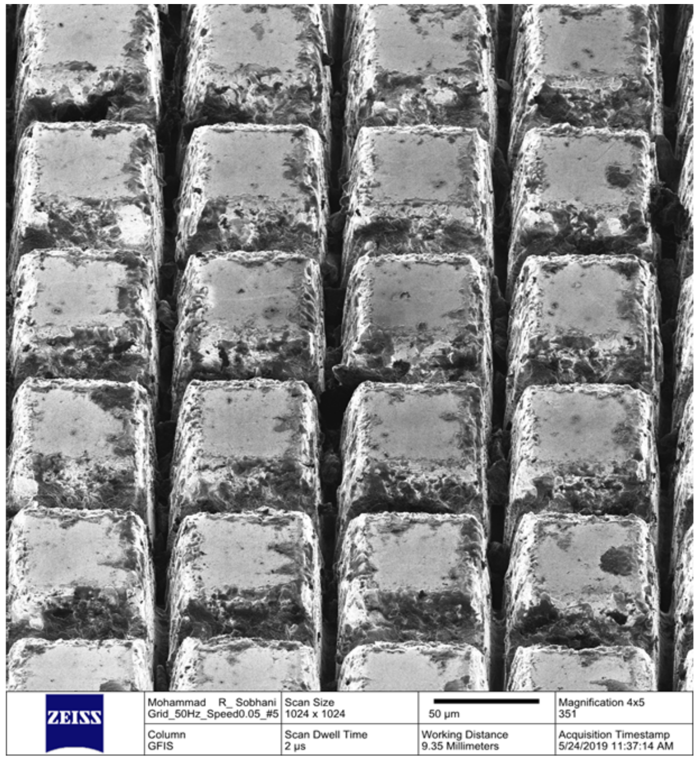

(a)

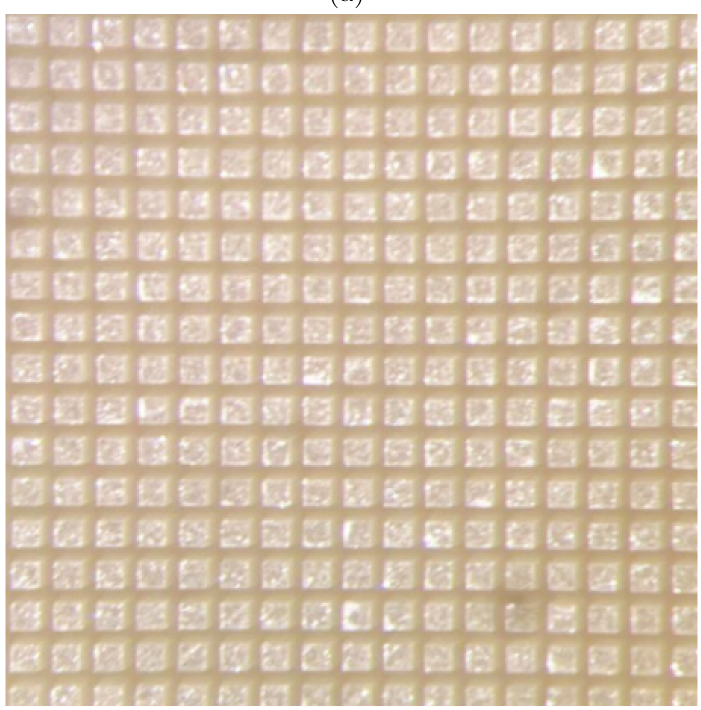

(b)

Figure 2.8: Fabrication of 1-3 composite by using: (a) laser micromachining for fine cuts and (b) dicing method.

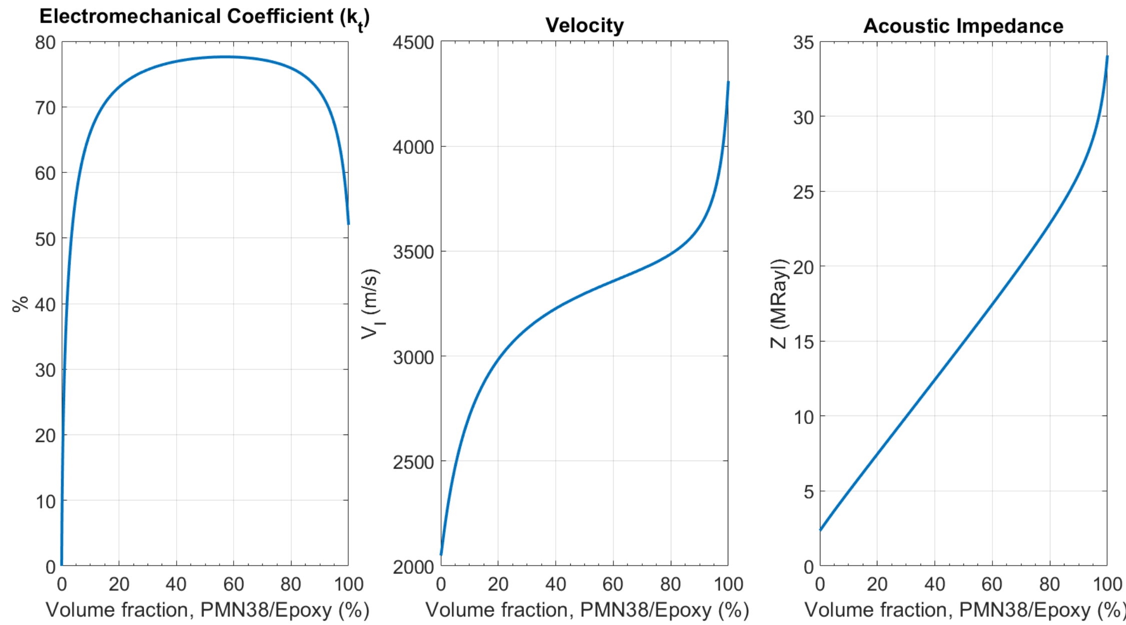

Figure 2.9: Simulated properties of a 1-3 composite material (PMN38/Epoxy301).

choose the suitable blade with the desired cut kerf. The fabrication of the transducer starts with making a 1-3 composite material by dicing the bulk PMN38 in the rows and columns to have small pillars. So, for a 10 MHz 128×128 TOBE array with a pitch size of lambda (∼150μm), we chose a pillar size of ∼60μm in each direction. This would result in a ∼65% active element fractional volume ratio where we get the maximum kt value as well as a reasonable acoustic impedance.

2.6 Bias-Sensitive TOBE vs Conventional Piezo RCA

As a summary for this chapter, TOBE arrays made of electrostrictive material offer bias sensitivity and switchability compared to conventional linear and piezoelectric-based row-column arrays (RCAs). As mentioned previously, the elements on the piezoelectric-based arrays are active all the time during the transmit and receive events. In contrast, this thesis reports the fabrication and development of bias-switchable TOBE arrays made of PMN38, whereby any individual elements on the

TOBE grid can activated by row and column addressing. Fig. 2.10 illustrates the schematic of a piezo-based RCA and PMN38 TOBE array with a focused beam transmitted along the rows.

In practice, bias-switchable TOBE arrays can do anything conventional piezo-based RCA and linear arrays can and offer more, such as aperture encoding/decoding and actively applying apodization to each row and column. Also, the developed bias-sensitive TOBE arrays offer adjustable elevational focusing/steering, which is impossible in linear arrays. Moreover, the conventional non-bias-sensitive RCAs provide images underneath the shadow of the array, while our proposed bias-sensitive TOBE arrays with implemented novel imaging schemes can provide sector imaging. This is an important feature for some of the applications, such as cardiac imaging, where the physical size of the array is limited to the spaces between the ribs.

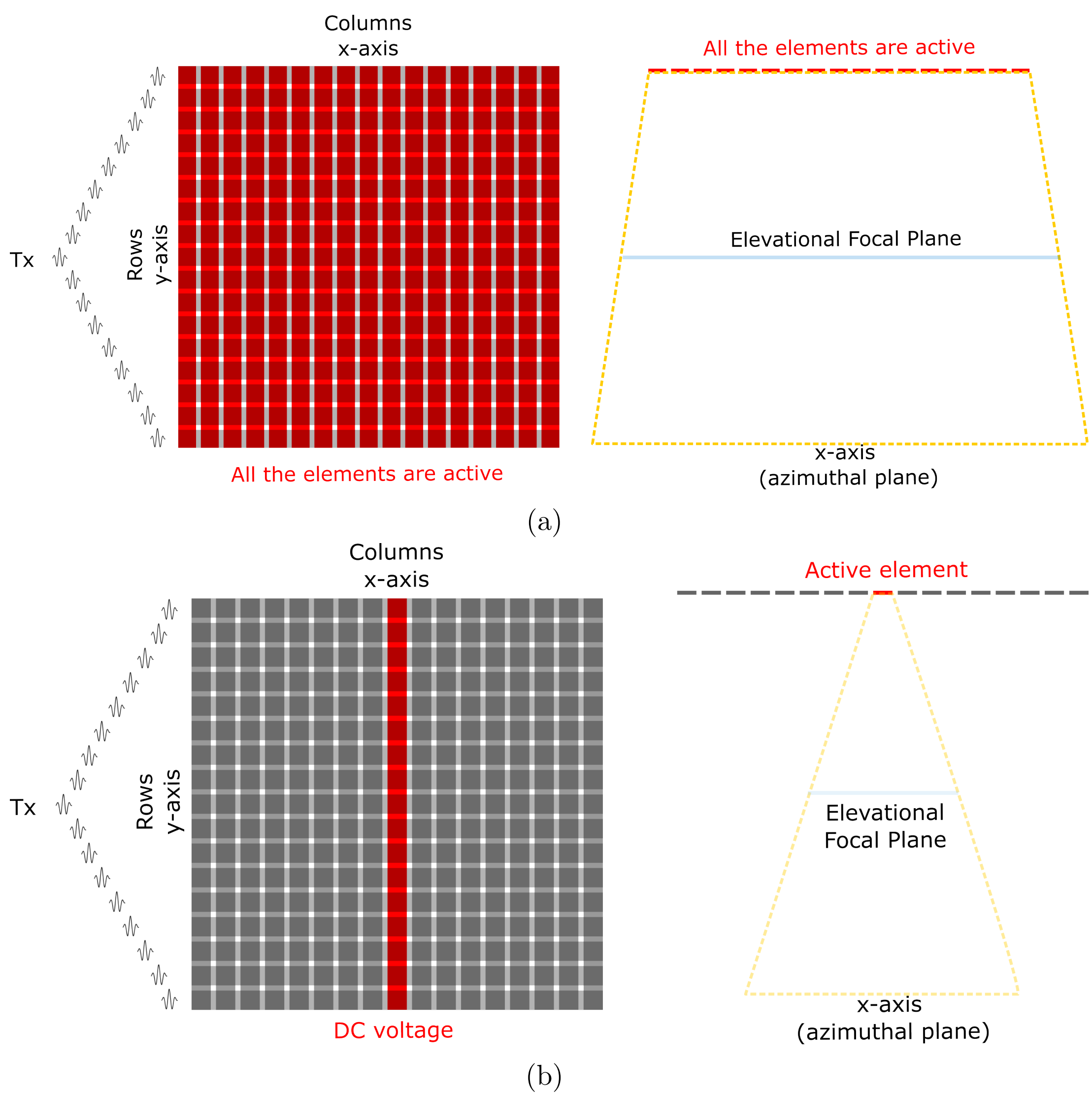

Figure 2.10: The comparison of RCA and TOBE arrays; (a) a conventional piezo-based RCA in which all the elements are active all the time, (b) a bias-switchable TOBE array made of PMN38 in which only the biased elements are active.

Chapter 3

Bias-Sensitive Transparent Single-Element Ultrasound Transducer

In this chapter, we introduce electrostrictive hot-pressed Lead Magnesium Niobate (PMN) with low Lead Titanate (PT) doping as a candidate transparent transducer material. We fabricate transparent high-frequency single-element transducers and characterize their optical, electrical, and acoustic properties. PMN-PT may offer sensitivity advantages over other transducer materials, such as Lithium Niobate, owing to its high electromechanical efficiency and bias-voltage sensitivity. The transparency of the fabricated transducer was measured 67% at 532 nm wavelength with a maximum electromechanical coefficient of ∼0.68 with a DC bias level of 100 V. The photoacoustic impulse response showed a center frequency of ∼27.6 MHz with a -6 dB bandwidth of ∼61% at a DC bias level of 40 V. Results demonstrate that the new transparent transducers hold promise for future optical-ultrasonic and photoacoustic imaging applications. Also, obtained results showed that this material can be used for bias-switchable applications where we aim to make unprecedented large ultrasound arrays for ultrasound/photoacoustic applications in the next chapters.

3.1 Introduction

Emerging combined optical and ultrasonic imaging and sensing technologies have been limited by opaque ultrasound transducers. Transparent transducers would enable optical imaging and light delivery through the transducer, rather than around it. Photoacoustic imaging (PAI) is one such technology that offers rich optical contrast with ultrasonic - or even optical spatial resolution [63]. Most photoacoustic imaging methods require non-optimal light delivery methods where optical and acoustic paths are separated [64].

Transparent ultrasound transducers could enable improved light delivery and shorter acoustic path lengths, leading to high signal-to-noise ratios. Transparent ultrasound transducers have recently been considered as an alternative to more conventional opaque transducers. Transparent Lithium niobate transducers were introduced some years ago using indium tin oxide electrodes, but initial work did not explore photoacoustic or imaging applications [65]. In 2019, Z. Li et al. demonstrated transparent single-element capacitive micromachined ultrasound transducers with accompanying through-illumination photoacoustic data [66]. Later the same year, Dangi et al. demonstrated a transparent single-element Lithium Niobate transducer for photoacoustic imaging [67]. The same group later demonstrated optical-resolution photoacoustic microscopy with similar devices [68]. R. Chen et al. successfully demonstrated PAI of mouse-ear vasculatures in vivo using a high-frequency transparent lithium niobate transducer [69]. The C. Kim group recently demonstrated multi-modality imaging with transparent ultrasound transducers, showing impressive imaging results in [70]. However, all these methods required mechanical scanning of the light source and/or the transducer to form images. Kashani et al. recently demonstrated transparent linear arrays for combined optical, ultrasonic, and photoacoustic imaging [71, 72]. Transparent ultrasound arrays have also been implemented using optical detection methods, and include Fabry-Perot etalon sensors, micro-ring resonators, etc. Fabry-Perot etalons have demonstrated high sensitivity 3D photoacoustic imaging but require scanning of an interrogation beam over the etalon, and sometimes optical tuning to account for etalon non-uniformities.

Our long-term objective is to develop transparent ultrasound array transducers enabling 3D ultrasonic and photoacoustic imaging with fast electronic readout. Recently, Ceroici et al. demonstrated electrostrictive bias-sensitive row-column arrays with a novel Hadamard-biasing and readout scheme for fast 3D imaging [50, 73]. This approach, however, used opaque row-column arrays. However, there may be an opportunity to achieve such arrays with transparent electrostrictive materials. Such materials would ideally be non-piezoelectric in the absence of a DC bias voltage, but become piezoelectric with an application of such voltage. Moreover, the phase of transmitted or received signals would ideally be shifted by 180 degrees with a bias polarity change to enable the required Hadamard bias readout schemes. As a step towards this goal, we here introduce a high-frequency transparent electrostrictive PMN-PT single-element transducer and demonstrate the feasibility of bias sensitivity.

3.2 Methods and Procedure

Here, we present the fabrication and the first usage of hot-pressed lead magnesium niobate (PMN) with low PT doping ($<0.1\%$ PT [74]) as a bias-sensitive transparent ultrasound transducer with a higher electromechanical coefficient. The low PT doping leads to electrostrictive rather than piezoelectric behavior, such that at room temperature, there is no hysteresis (i.e., no residual polarization) when cycling the electric field and measuring material polarization. This behavior is important for envisioned TOBE array bias-encoding operations as detailed in [75], with a fabricated high-frequency transducer in [76]. This relaxor material has an extremely large dielectric and electrostrictive constant. Hot-pressed PMN-PT has been used for electro-optic devices, but to our knowledge, this is the first time this material has been investigated as a transparent ultrasound transducer. The transducer is fabricated by cutting down the bulk hot-pressed PMN-PT (Boston Applied Technologies, Inc., U.S.) into ∼1 mm thick samples using a diamond-wire saw (STX201, MTI Corporation, CA, U.S.) and then lapping to ∼80 μm thickness (Unipol 1202, Laizhou Weiyi experimental machine manufacturing Co., Ltd., China), followed by fine polishing on both sides (Fig. 3.1 (b)). The PMN-PT half-lambda thickness is the primary determinant of the resonance frequency, predicted to be ∼30MHz. A layer of ∼250 nm indium tin oxide (ITO) is deposited as a transparent electrode on both sides of the transducer with a measured sheet resistivity as low as 37.2 Ω/sq. To measure ITO resistivity, we used a four-point probe (Lucus Pro4 4000, CA, USA). The fabricated transducer showed a transparency of 67% at 532 nm (Fig. 3.1 (c)). The transducer is diced into 4 x 4 mm squares and then mounted on a PCB with an open aperture to let the laser beam pass through. The bottom and top electrodes are connected to the PCB by a thin layer of gold masked during deposition with a photoresist patterned to create non-transparent metal bond-pads at the edge of the transducer. The transparent aperture measures ∼ 3.5 mm × 3.5 mm. Next, an SMA connector is connected to the PCB. A thick layer of transparent Epotek-301 with an acoustic impedance of ∼3 MRayls was used as a backing material. Fig. 3.1 (d),(e) illustrate the side view and the fabricated transducer, respectively.

As part of the characterization, the laser damage threshold was measured for separate material samples, including a 3mm block of polished Epoxy-301, a ∼200 μm thick layer of transparent PMN, and a ∼250 nm layer of ITO sputtered on a glass wafer. A Nd:YAG pulsed 532 nm laser with a repetition rate of 10 Hz was guided to the samples. For the damage test, each sample was hit by 2000 laser shots for a few different energy levels. However, all the tested materials could withstand up to ∼60 mJ/cm2, without any apparent damage, which is three times the ANSI maximum permissible exposure used for biomedical applications. The laser damage threshold for Parylene C, however, was 23 mJ/cm2 for a ∼50 μm layer of Parylene C.

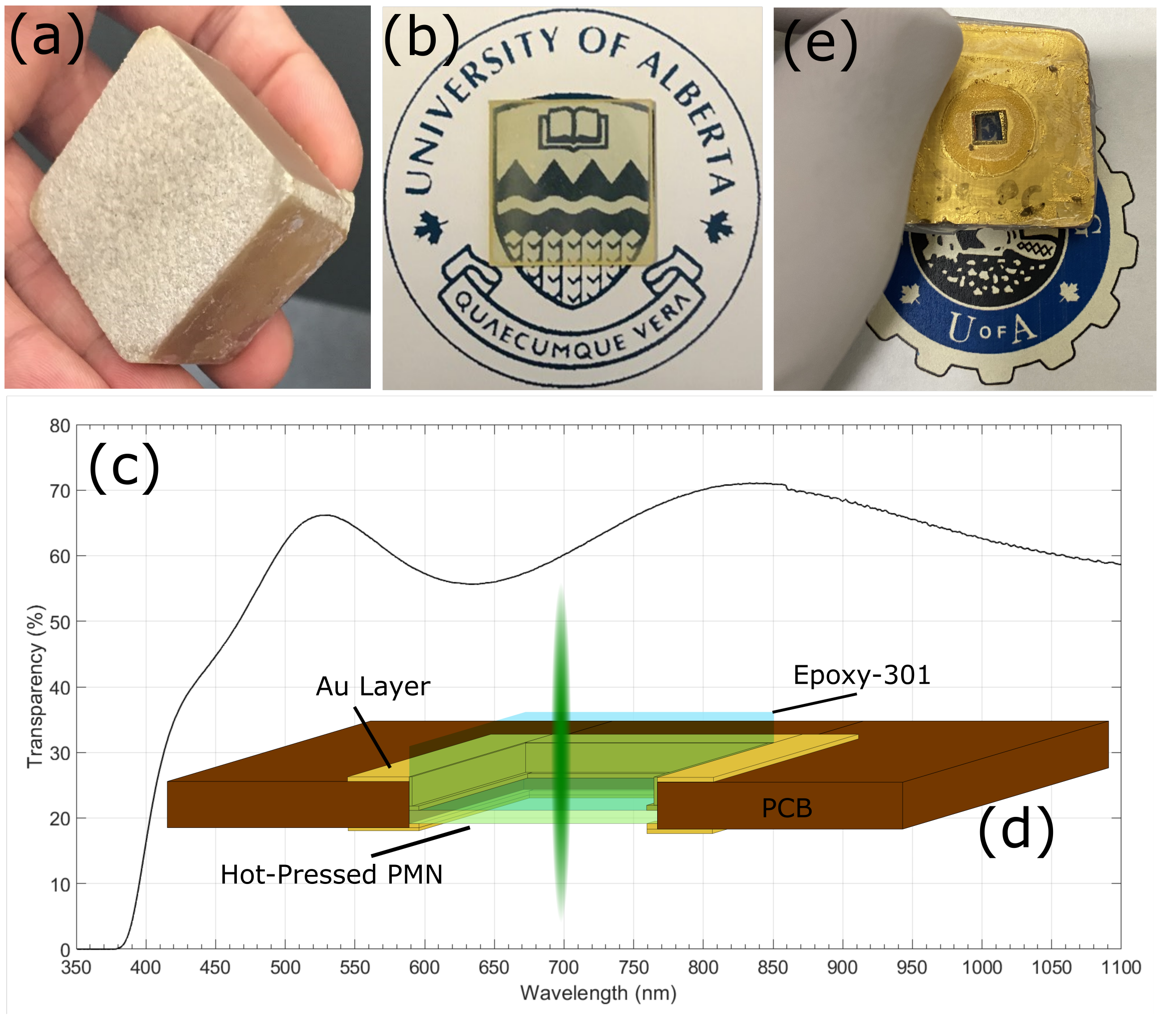

Figure 3.1: The fabricated transparent ultrasound transducer based on electrostrictive PMN-PT and transparency measurement. (a) The raw bulk hot-pressed PMN-PT measuring roughly 40 mm × 40 mm x 25 mm. (b) Precisely polished, and ITO coated ∼80 µm thick PMN-PT. (c) Transparency measurement of the fabricated transducer with maximum transparency of 67% at 532 nm. (d) diagram of the transducer cross section. (e) The fabricated transparent transducer mounted on a PCB with a transparent aperture of roughly 3.5 mm × 3.5 mm.

3.3 Results

The bias sensitivity and the electromechanical efficiency of the transducer were characterized by measuring the resonance and anti-resonance frequencies with an impedance analyzer for different DC bias voltages. Two different fabricated transducers were used for these measurements, the first one without a matching layer and another one with a layer of ~20 μm (quarter-wavelength) Parylene C as a front matching layer. The deposition of the matching layer was obtained by evaporating ~39 grams of Parylene C inside a vacuum chamber. Although the matching layer adds some damping to the transducer and decreases the operational center frequency, it showed an improvement in the transducer sensitivity and with non-noticeable electromechanical coefficient changes. Fig. 3.2 (a) and (c) illustrate the magnitude of the unloaded input impedance for both transducers, with and without matching layer, respectively. The electromechanical coefficient (k_t) value was calculated using measured resonance and anti-resonance frequencies, as detailed in [57] and expressed in Eq. 3.1, where ω_S and ω_P are the resonance and anti-resonance frequencies, respectively.

$$k_t = \sqrt{(\frac{\pi\omega_s}{2\omega_p})tan[\pi\frac{(\omega_p - \omega_s)}{2\omega_p}]} \tag{3.1}$$

As expected, the hot-pressed PMN-PT material shows no piezoelectric effect for a 0 Volt bias voltage while an increment on the kt was seen while the biasing voltage increases. Both the transducers showed almost the same kt for the same level of biasing with a maximum value of ~0.68 for a voltage of 100V, which is higher than Lithium Niobate (with k_t of ~0.49). Single-crystal PMN-PT may provide even higher kt values; however, most PMN-PT materials have higher PT doping and thus are not purely electrostrictive as required in our envisioned applications.

The lower electrical impedance of the transducers is due to the high dielectric constant of the Hot-Pressed PMN-PT material and the large area of the transducers. Such a small input impedance causes a large electrical mismatch when transmitting on

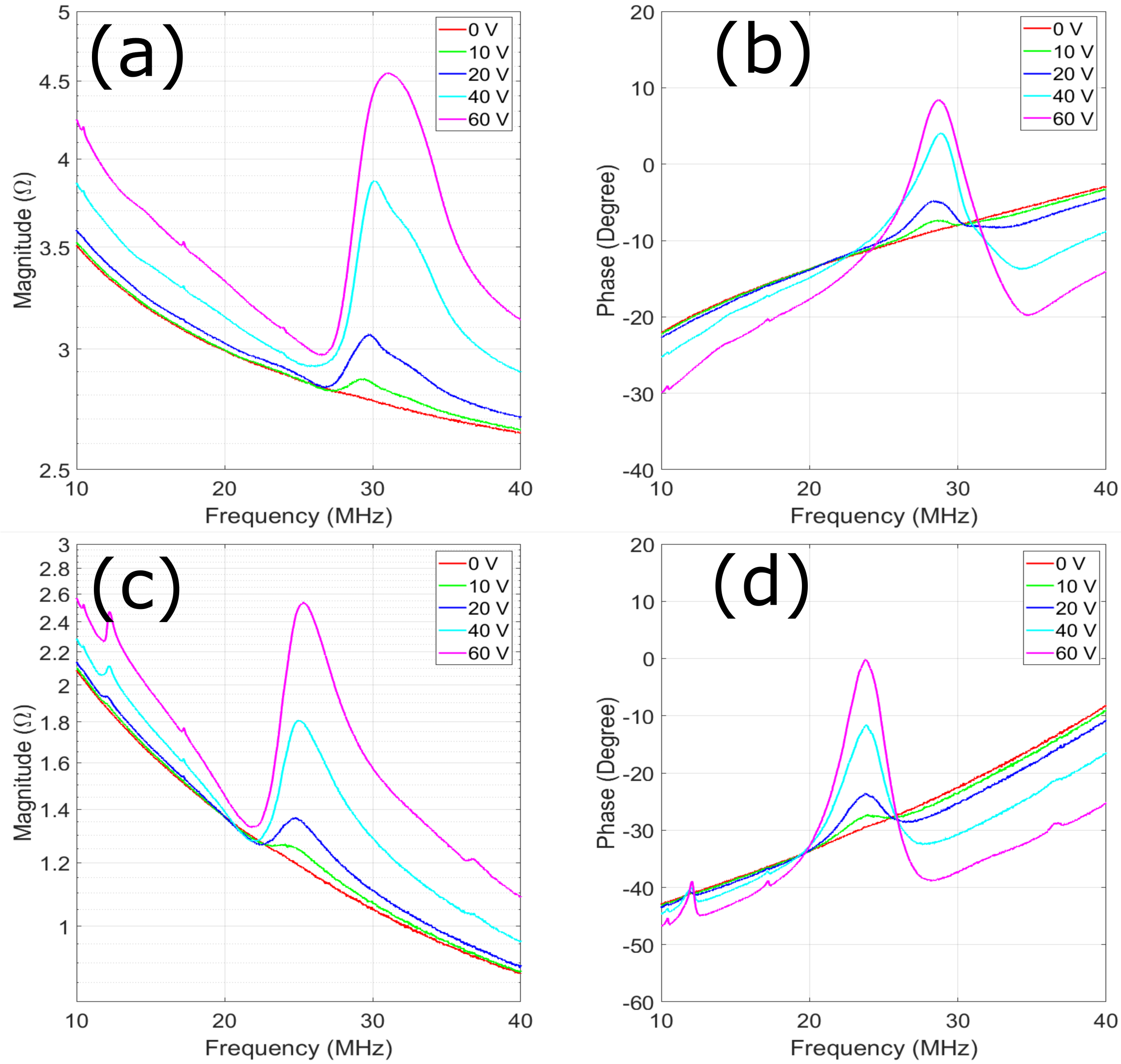

Figure 3.2: The measured input impedance of the transducers without loading on the front surface. (a),(b) The magnitude and phase of the input impedance for the fabricated transducer without a matching layer. (c),(d) The magnitude and phase of the input impedance for the fabricated transducer with a matching layer.

the transducer. For measuring the receive response of the transducer, a commercial broad-band 25 MHz transducer (V324-SM, Olympus Scientific Solutions Americas Inc. U.S.) with a focus point of half an inch was used as a transmitter while receiving on the fabricated transducers. A tank filled with deionized water was used for immersion testing. The 25 MHz transducer was placed 0.5 inches away from the fabricated transducer while transmitting the focused beam to the center of the transducer. The measurements are done for different values of DC bias voltages. The received signals were recorded after amplifying with a +28 dB, 5 to 75 MHz amplifier (PANAMETICS-NDT 5073PR). As shown in Fig. 3.3 (a) for the measured impulse responses, the fabricated transparent transducer without a front matching layer has a center frequency of 27.5 MHz with a -6 dB bandwidth of 36% at a DC bias voltage of 60 V. The transducer with a front matching layer showed a center frequency of 23.4 MHz with a bandwidth of 38% at the same DC biasing level. The matching layer slightly decreased the center frequency but increased the amplitude of the received signal from a peak-to-peak voltage (Vpp) of 780 mVpp to 1312 mVpp. The receive sensitivity of the transducers was measured by a Hydrophone at a 10 mm axial distance with a maximum sensitivity of $\sim$4.2 μV/kPa and $\sim$7.1 μV/kPa for the fabricated transducers with and without the matching layer, respectively. The hydrophone was first used to measure the acoustic pressure at a 10 mm axial distance when transmitting on the 25 MHz commercial transducer. The transmitter sends a negative short pulse to excite the transducer. Then the same 25 MHz transducer was used at the same axial distance (10mm) to transmit the same acoustic wave and the signals were received on the fabricated transducers. For the given pressure and measured signal amplitude from each transducer, we have calculated the receive sensitivity for each fabricated transducer.

The photoacoustic (PA) response of the transducer was obtained only on the transparent transducer without a matching layer to avoid damage to the Parylene C layer. The characterization is done by guiding a pulsed 532 nm laser beam through the transducer and hitting a thin carbon fiber bundle inside a water tank filled with DI-Water. The diameter of the beam was ∼1mm when hitting the target with a measured power of ∼10 mW at a repetition rate of 10 Hz. Fig. 3.3(b) illustrates the PA impulse response of the transducer with a center frequency of ∼27.6 MHz and a -6 dB bandwidth of ∼61% at a DC bias level of 40 V. Changing the polarity of the bias voltage keeps the sensitivity level the same but shifts the received signal's phase by 180 degrees. This makes our bias-sensitive fabricated transducer a good candidate for aperture coding/decoding applications with adjustable sensitivity. The axial resolution of the single-element transparent transducer was estimated by taking the full-width at half-maximum (FWHM) of an envelope applied to the photoacoustic signal from the thin carbon fiber bundle shown in Fig. 3.3(b). The FWHM was found to be ∼60 ns, resulting in ∼90 μm in water. The obtained resolution is in a good agreement with ∼78.6 μm calculated by 0.88*c/BW as described in [77]. The resolution can be significantly improved by adding a high-impedance backing layer, adding a matching layer, and designing an electrical matching network in future work.

We performed a simple photoacoustic imaging experiment, scanning a focused laser spot re-focused from a multi-mode fiber through the transducer. The lateral resolution in this experiment was determined by the laser spot size and was estimated from an edge-spread function by scanning a USAF 1951 resolution target and plotting the peak amplitude of the envelope detected photoacoustic responses, as illustrated in Fig. 3.4(b) and (c). The spatial resolution was estimated from the edge-spread function as ∼285 μm, as measured for a rise from 10% to 90% of the peak amplitude across the edge. The imaging resolution can be improved by tighter optical focusing in future work.

To demonstrate the potential advantages of our transparent transducers, we performed photoacoustic imaging experiments in a scattering phantom with an embedded blood tube. The phantom was a cornstarch-gelatin phantom (10% cornstarch, 10% gelatin powder, and 80% water, by weight), which previously was shown to exhibit ul-

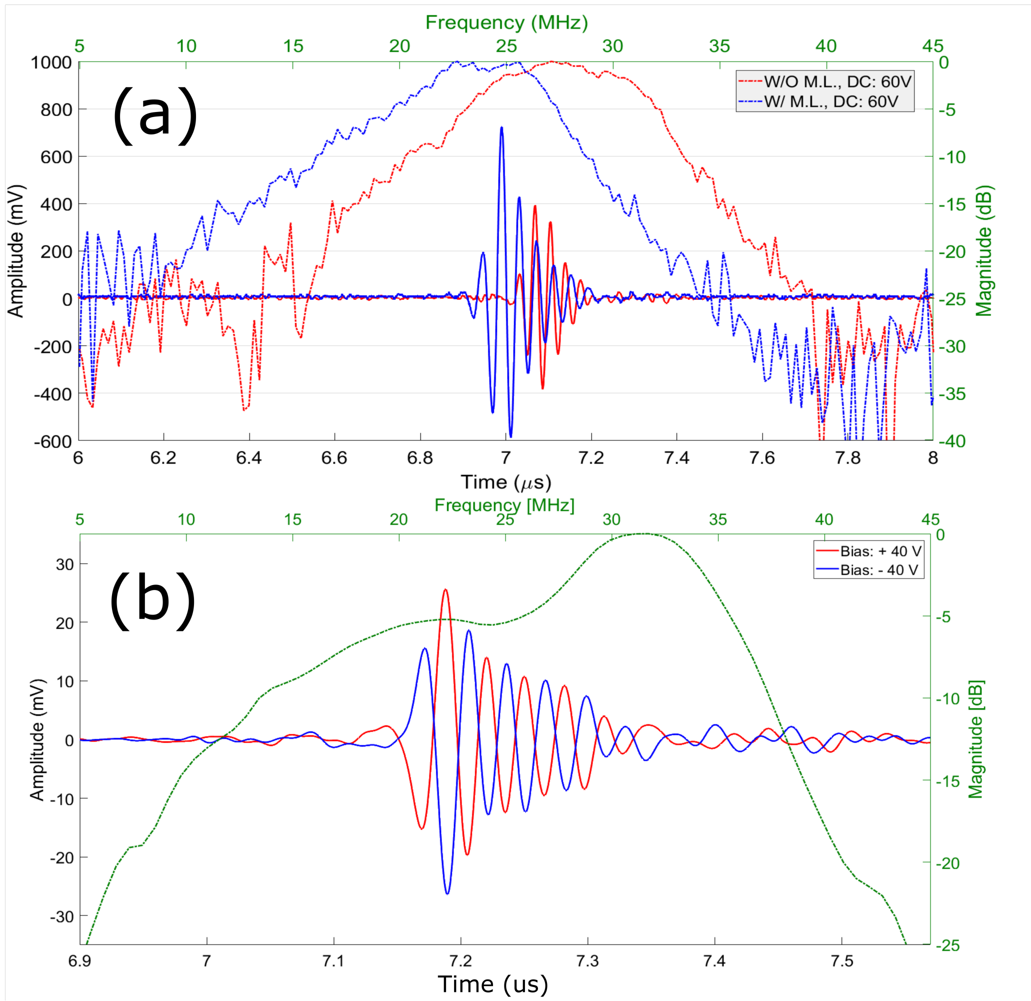

Figure 3.3: The measured acoustic receive response and photoacoustic responses of the transducers. (a) The amplitude and phase of the impulse response for the fabricated transparent transducers, with and without matching layer at +60 V bias. (b) The PA response of the transducer without matching layer at +40 and -40 Volts bias.

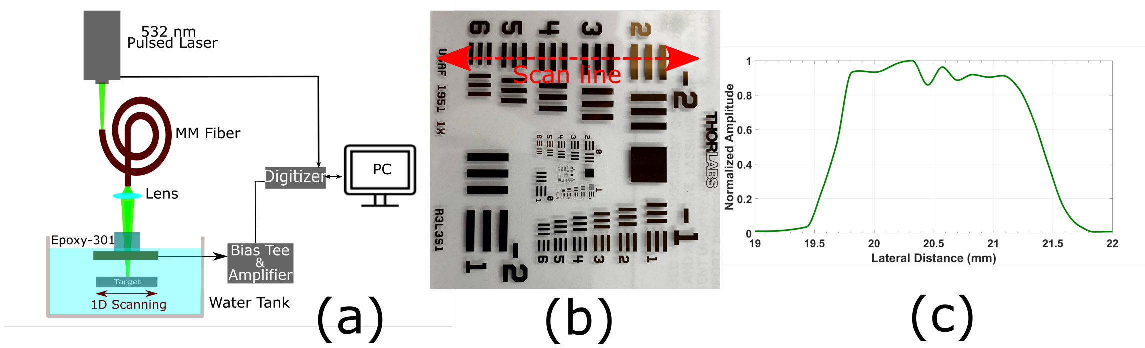

Figure 3.4: PAI using the fabricated transparent PMN-PT transducer without a matching layer. (a) The laser setup for 1D scanning. (b) The linear PA scan was performed along a 3 mm line covering a line pair of element 3 in group -2. (c) The normalized PA amplitude of the scanned line for measuring the lateral resolution of the system.

trasonic and optical properties similar to tissues [78]. We investigated three different configurations: (a) trans-illumination through the fabricated unfocused transparent ultrasound transducer in direct contact with the scattering phantom (b) oblique illumination around the transducer (also in contact with the phantom) and (c) oblique illumination around a focused transducer (V324-SM, Olympus Scientific Solutions Americas Inc. U.S.) positioned with an ~11mm standoff distance in water, as shown in Fig. 3.5. The oblique illumination scenario (b) suffered from a long optical propagation length through the scattering medium and thus produced a very weak photoacoustic signal compared to the trans-illumination scenario (a). Even when using a focused transducer with a water standoff to allow for oblique illumination to hit closer to the blood tube, signal-to-noise was still ~4dB lower than the transparent transducer through illumination scenario. The through-illumination measurement was ~25dB larger than the oblique illumination experiment b). This is primarily attributed to the long optical propagation distance through the scattering medium, greatly reducing the fluence at the blood tube. In all experiments, we used a 532-nm 8-ns pulsed laser with identical surface spot size and a laser surface fluence of ~12mJ/cm2. The received photoacoustic signals were recorded after amplifying with a +28 dB, 5 to 75 MHz amplifier (PANAMETICS-NDT 5073PR).

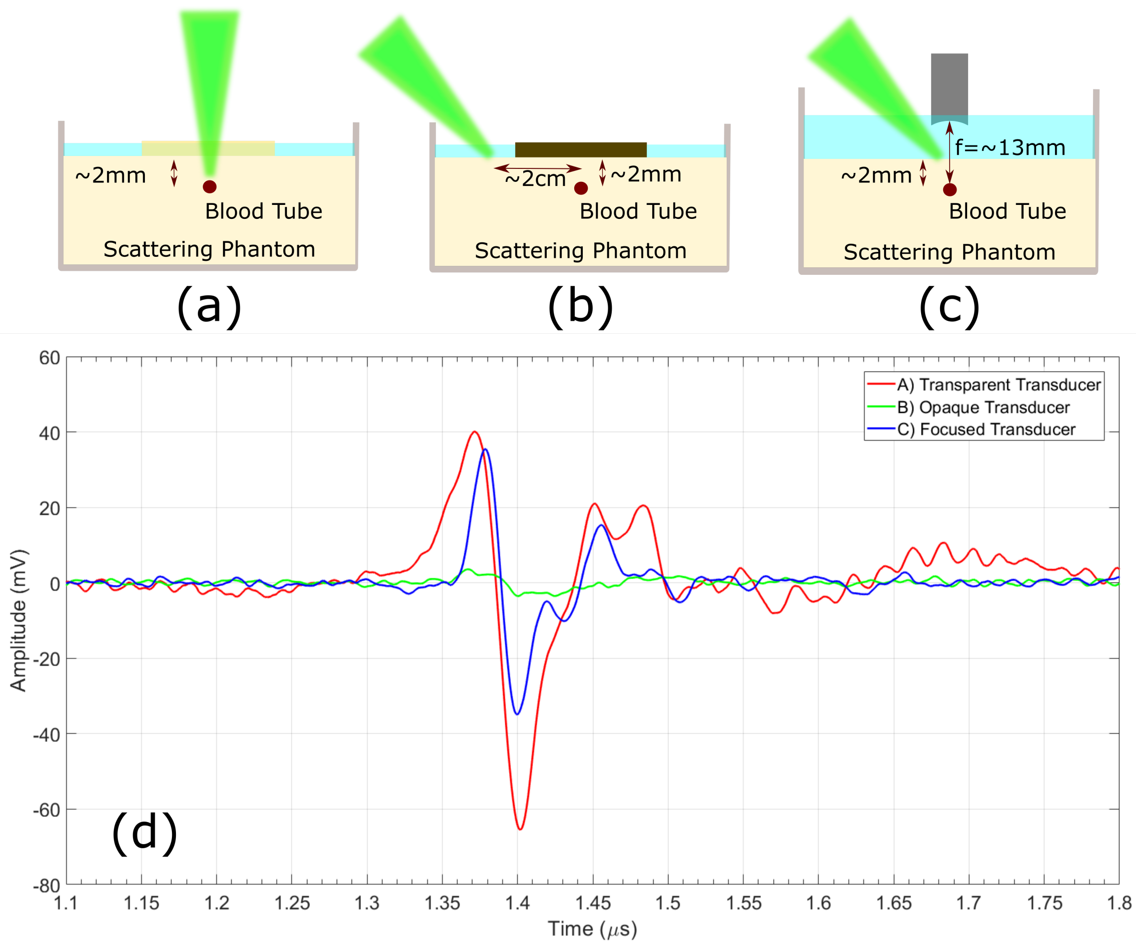

Figure 3.5: Comparison of PA signals obtained from a scattering phantom with an embedded blood tube. (a) illumination through the fabricated unfocused transparent transducer (b) oblique illumination around the opaque transducer (c) oblique illumination around the focused transducer positioned ~11mm above the phantom (d) their photoacoustic received signals.

3.4 Discussion and Conclusions

Current work is limited to single-element transparent transducers to establish the feasibility of hot-pressed PMN-PT as a novel electrostrictive transducer material. The single element transducer was lapped thin enough to provide higher frequency. It is obvious that for a lower-frequency transducer, which requires thicker material, the transparency would be smaller than what is reported here. One solution to further improve the transparency and overall performance of the investigated transparent single-element transducer is the development of the quarter-wavelength transducer with clamped backing. This would result in a thinner transducer maintaining good transparency for lower frequencies as well as half of the biasing voltage required compared to the conventional half-lambda thick transducers. Also, the transparency depends on the PT dopant of the PMN-PT electrostrictive material, where transparency improves with lower PT dopants. Future work could involve the development of linear or even 2D arrays, including top-orthogonal-to-bottom electrode arrays, which could enable bias-switchable readout of every element using only rows and columns.

An additional limitation of current work is the lack of a suitable backing material. Epoxy was tested as a backing material, but its impedance was not adequately matched to the PMN-PT, and thus, ringing was observed in the transducer response, limiting the fractional bandwidth of the transducer. Future work could consider glass delay lines or fiber bundles as a backing material, which should be better impedance-matched and thus provide a means of reducing ringing. Additional work is also needed to develop improved transparent matching layers that have a high optical damage threshold.

Transparent transducers could find important uses for wearable fiber-tethered photoacoustic devices to measure venous oxygen saturation, which cannot be measured with pulse oximetry. They could also be developed into arrays for improved deep-tissue photoacoustic imaging. They may further have applications to endoscopic or laparoscopic, trans-rectal or trans-vaginal form factors, where it is difficult to share optical and ultrasonic real-estate.

In conclusion, the fabrication steps and the preliminary results of a novel bias-sensitive transparent high-frequency ultrasound transducer made of hot-pressed PMN-PT are presented. The transparency of the transducers was measured ∼67% at 532 nm wavelength with a maximum electromechanical coefficient of ∼0.68 with a DC bias level of 100 V. The high bias voltages used here could be an electrical safety concern for human subject imaging without proper isolation. However, dielectric matching layers and/or additional grounding layers could provide suitable isolation for safe use. The effect of the matching layer on the transducer was investigated, which resulted in increasing the bandwidth from 36% to 38% and with a ∼168% improvement in the received signal peak-to-peak value. The center frequency of the transducer was slightly shifted from 27.5 MHz to 23.5 MHz due to the Parylene C matching layer. Our measured kt value of 0.68 is significantly improved compared to other transparent transducers such as lithium niobate with a reported kt of 0.49. However, our measured kt is less than that reported for single-crystal PMN-PT (>0.8), which could be a promising transparent technology in future work. However, electrostrictive PMN-PT with low-PT doping is not yet commercially available. In future work, we aim to fabricate top-orthogonal-to-bottom-electrode (TOBE) ultrasound arrays using these materials that should be capable of aperture coding/decoding, as well as sensitivity adjustment by changing the applied biasing polarity and voltages, respectively. Future work should investigate improved backing and the front matching layers that will be both transparent and be more immune to laser damage.

Chapter 4

Ultrafast Imaging with Bias-Sensitive TOBE Arrays

Top-orthogonal-to-bottom electrode (TOBE) arrays, also known as row-column arrays, have shown great promise as an alternative to fully-wired 2D arrays, owing to a considerable reduction in channels. Novel imaging schemes with bias-switchable TOBE arrays were previously shown to offer promise compared to previous non-bias-switchable row-column imaging schemes and compared to previously-developed Explososcan methods, however, they required significant coherent compounding. This chapter, which is an original work published in [79], introduces Ultra-Fast Orthogonal Row-Column Electronic Scanning (uFORCES), an ultrafast coded synthetic aperture imaging method. Unlike its FORCES predecessor [73], uFORCES can achieve coherent compounding with only a few transmit events and may thus be more robust to tissue motion. Simulations demonstrated that uFORCES can potentially offer improved resolution compared to the matrix probes having beamformers constrained by the paraxial approximation. Also, unlike current matrix probe technology incorporating microbeamforming, uFORCES with bias-switchable TOBE arrays can achieve ultrafast imaging at thousands of frames per second using only row- and column addressing.

This chapter also demonstrates the experimental implementation of uFORCES using a fabricated 128×128 electrostrictive TOBE array on a crossed 25 μm gold wire phantom and a tissue-mimicking phantom. The potential for improved resolution and ultrafast imaging with uFORCES could enable new essential imaging capabilities for clinical and pre-clinical ultrasound.

4.1 Introduction

Two-dimensional array transducers have enabled 3D ultrasound imaging but with clinical impact currently limited in part by the image quality. With such 2D arrays, there exist difficult engineering trade-offs between system complexity and achievable image quality. Large probes with high-element density would produce high-quality images but with a resulting large number of channels leading to significant interconnect and channel count difficulties. Implementation of fully-wired arrays is currently prohibitive, with commercial (non-microbeamformer) arrays available with only 32×32 elements, leading to small aperture sizes and poor image quality. Various previous 3D imaging techniques have been implemented by mechanical sweeping of a linear or annular transducer but these were not capable of fast volumetric imaging [9, 12, 80]. A few approaches have been made to reduce the channel count while having a larger aperture size, such as multiplexing and sparsely distributing the active elements with limited channels but these methods have thus far demonstrated sidelobe artifacts that degrade image quality [4, 13, 15]. Image quality from 2D arrays has been dramatically improved with the use of micro-beamforming, involving pre-amplifiers, analog-to-digital converters, and delay-and-sum circuitry implemented as a custom integrated circuit beneath the shadow of each element.

In microbeamforming, fine-delays are introduced to elements before summing in groups, and coarse delays are implemented in the mainframe. Often, micro-beamformers implement tilt-only fine-delays as a linear approximation to a quadratic delay profile. These approximations can be a source of image quality degradation, especially when using parallel beamforming to reconstruct a group of adjacent A-scan lines over a wide area, as ideal focal delays are accurate only for one line-of-sight. As a result, microbeamformer-based matrix probes may not necessarily provide the B-scan image quality otherwise found with simpler linear or phased array probes.

Beyond image quality considerations, such microbeamforming-based matrix probes do not yet provide ultrafast imaging capabilities. Such ultrafast ultrasound methods offer imaging at thousands of frames per second and have enabled ultrasensitive blood-flow tracking, shear-wave imaging, super-resolution imaging, and other emerging applications, but such work has primarily been done in 2D with linear array transducers. Some groups have started to explore ultrafast imaging using 2D fully-wired or sparse arrays, but such fully-wired 2D arrays have been limited to 32×32 elements, and both fully-wired and sparse array methods have thus far provided limited image quality [13, 81].

Row-column arrays have been investigated as a means of reducing interconnect complexity as they can be addressed using only row and column electrodes [36–38, 41, 47, 82–86]. Also known as top orthogonal to bottom electrode (TOBE) arrays, they offer significant promise for next-generation 3D imaging. They have been implemented with piezoelectrics, capacitive micromachined ultrasound transducers (CMUTs), and more recently electrostrictive realizations. Unlike the piezoelectric materials, electrostrictive materials show no piezoelectricity effect unless a DC bias voltage is applied, making them bias-sensitive. Additionally, the polarity of the applied bias voltage determines the polarity of dipoles inside the materials, making them a good candidate for bias coding applications. Thus, unlike piezoelectric implementations, CMUT- and electrostrictive implementations of TOBE arrays offer bias-sensitivity, which can be used advantageously for novel imaging schemes. These have included Simultaneous Azimuthal and Fresnel Elevational (SAFE) compounding, which exploits Fresnel-lens-based elevational focusing, introduced by K. Latham et al. in [48, 87]. Importantly, each element of such a bias-sensitive TOBE array can be addressed by biasing a row and transmitting or receiving from a column. Hadamard or S-Matrix-encoded biasing schemes have furthermore been proposed to improve signal-to-noise ratio with good success, including in our recent demonstrations of 3D imaging techniques [1, 2, 49, 84, 88].

Such Hadamard-encoding schemes have also been put to use for aperture-encoded synthetic aperture imaging using our recently-developed imaging scheme called Fast Orthogonal Row-Column Electronic Scanning (FORCES). FORCES involves biasing columns with a sequence of Hadamard biasing patterns while transmitting pulses along rows with focal delays to create a cylindrical elevational transmit focus. By using a new Hadamard pattern for each of N transmit events, while receiving echoes from columns, an encoded synthetic transmit aperture dataset is collected. After decoding by multiplying by an inverse Hadamard matrix, the decoded channel dataset represents a synthetic transmit aperture dataset, consisting of a received signal from each element for each respective (elevationally-focused) transmitting column. FORCES was demonstrated to produce elevationally-steerable B-scans with image quality superior to previous non-encoded row-column imaging schemes and significantly superior to Explososcan schemes constrained by a similar total channel count. These contributions were significant because it demonstrated the potential advantages of using a bias-switchable row-column array compared to previous non-bias-sensitive array schemes and compared to linear array transducers. Moreover, unlike a linear array, our methods provided electronic elevational focusing control, electronic scan-plane steering, and 3D imaging.

A significant limitation of previous FORCES and SAFE compounding schemes, however, was the necessity for coherent compounding over a large number of transmits, which is troublesome in the presence of tissue motion. For a 128×128 array, FORCES would require motion-free coherent compounding over 128 transmit events, which may not be realistic in many clinical scenarios. Some recent work sought to minimize the number of transmit events for 3D imaging using orthogonal plane-wave compounding and non-bias-sensitive row-column arrays. However, while enabling fast 3D imaging, significant reconstruction artifacts were present, limiting image quality.

Previous work in linear array-based synthetic aperture imaging has demonstrated high image quality using sparse transmission schemes, where the number of transmit events for coherent compounding was limited.

In this work, we seek to achieve sparse synthetic aperture imaging schemes similar to FORCES, but which require coherent compounding over only a few transmit events. We call our approach Ultra-Fast Orthogonal Row-Column Electronic Scanning (uFORCES). We demonstrate through simulations that uFORCES can potentially offer improved resolution compared to microbeamformer-based and even fully-wired matrix probes constrained by the paraxial approximation in dynamic focusing. Also, unlike current matrix probe technology incorporating microbeamforming, uFORCES with bias-switchable TOBE arrays can achieve ultrafast imaging at thousands of frames per second using only row- and column addressing. Using a fabricated 128×128 electrostrictive TOBE array, we also experimentally show the implementation of uFORCES on a crossed 25 μm gold wire phantom. Our work could provide an alternative, and in some cases, improved 3D imaging technology to matrix probe technology, ushering in new opportunities for improved image quality in clinical imaging and enabling ultrafast imaging modes for next-generation imaging.

4.2 Methods and Procedure

This paper hypothesizes that the sparsely coded synthetic aperture imaging scheme implemented on a bias-sensitive TOBE array (called uFORCES) will exhibit comparable or improved resolution to a state-of-the-art fully-wired matrix probe. Thus, three different imaging schemes were investigated: (1) FORCES and (2) uFORCES were implemented with a TOBE array. (3) A walking aperture scheme on a fully wired 2D array (simulating a matrix probe) was implemented for comparison. These imaging schemes are briefly illustrated in Fig. 4.1. The active aperture is kept the same in all simulations. A walking aperture scheme is selected for the matrix probe as it represents the best possible image quality that could be achieved (in con-

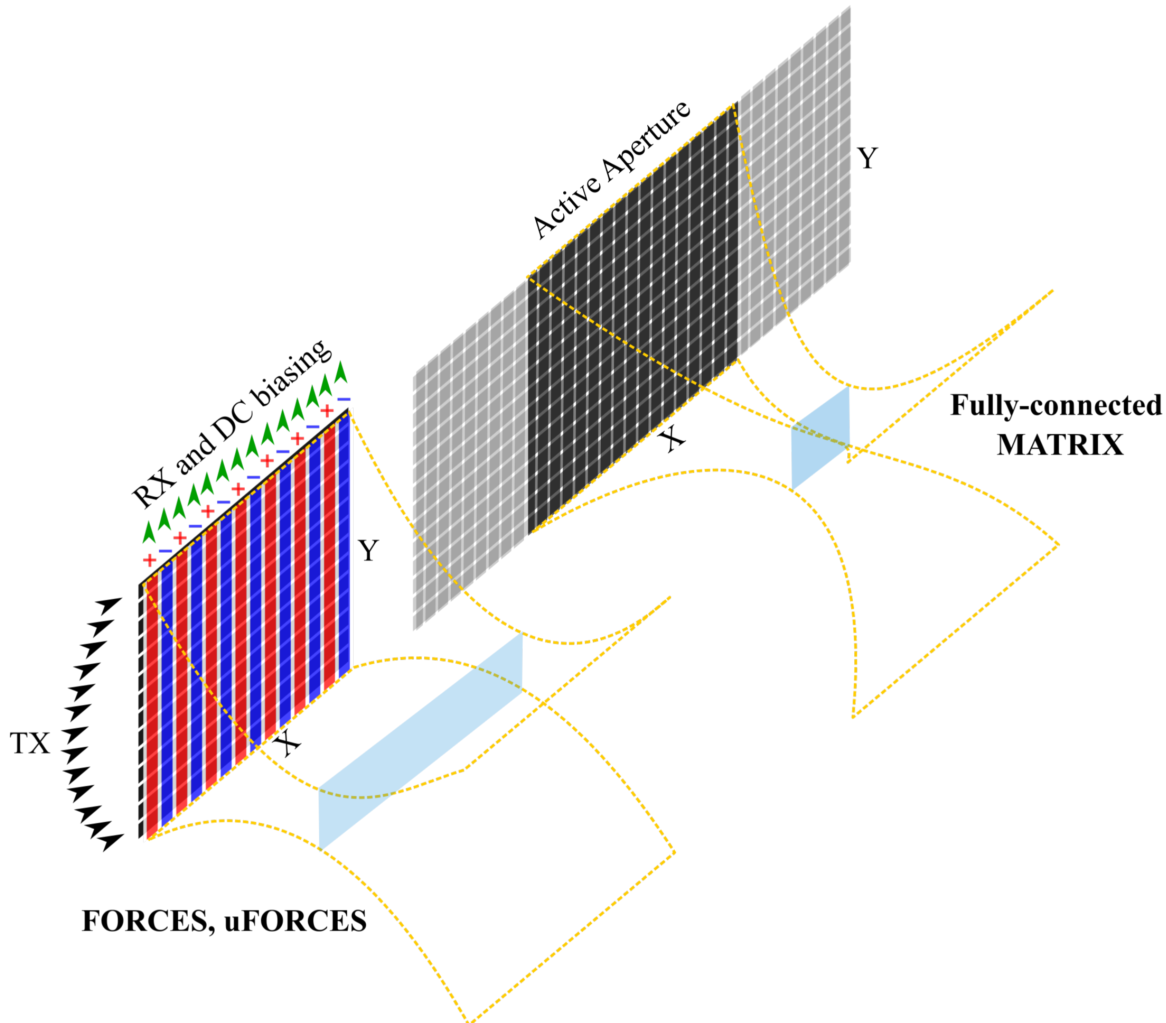

Figure 4.1: Illustration of different imaging schemes investigated in this paper. The size of the active aperture for fully-connected matrix probe is the same as the aperture size for TOBE arrays.

trast to sector scanning). Additionally, unlike a true matrix probe which implements micro-beamformer approximations, we simulate a fully-wired array and beamforming constrained to a quadratic delay profile associated with the paraxial approximation.

4.2.1 FORCES and uFORCES

FORCES has successfully been introduced and implemented in [1, 2]. In summary, as shown in Fig. 4.1, FORCES transmits delayed pulses on rows to achieve elevational focusing and receives along columns. The columns are bias coded with Hadamard

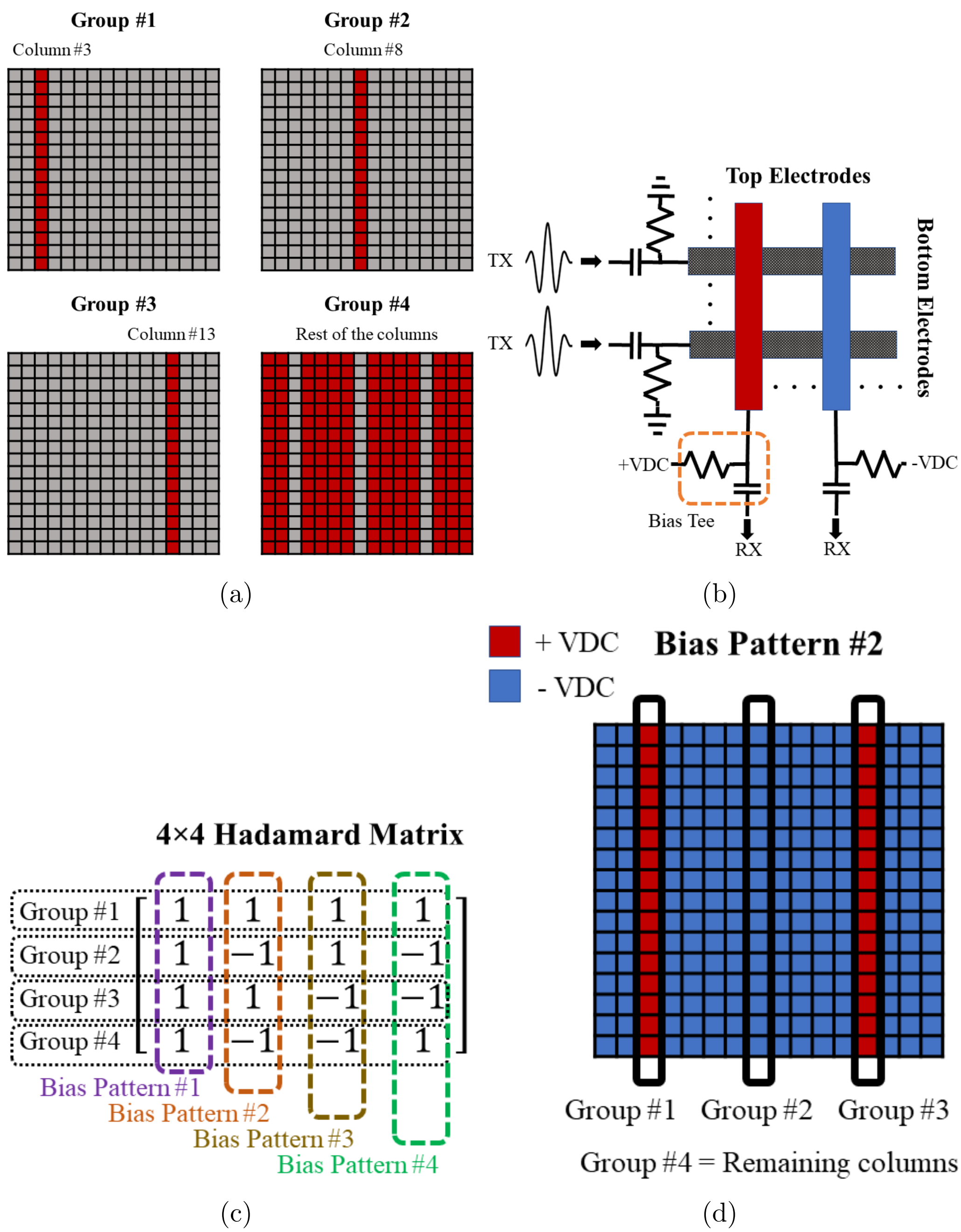

Group #1
Column #3
Group #2
Column #8
Group #3
Column #13
Group #4
Rest of the columns
(a)
Top Electrodes
Bottom Electrodes
TX
TX
+VDC
-VDC
Bias Tee
RX
RX
(b)
4×4 Hadamard Matrix
Group #1
Group #2
Group #3
Group #4
1 1 1 1
1 −1 1 −1
1 1 −1 −1
1 −1 −1 1
Bias Pattern #1
Bias Pattern #2
Bias Pattern #3
Bias Pattern #4
(c)
+ VDC
- VDC
Bias Pattern #2
Group #1
Group #2
Group #3
Group #4 = Remaining columns
(d)

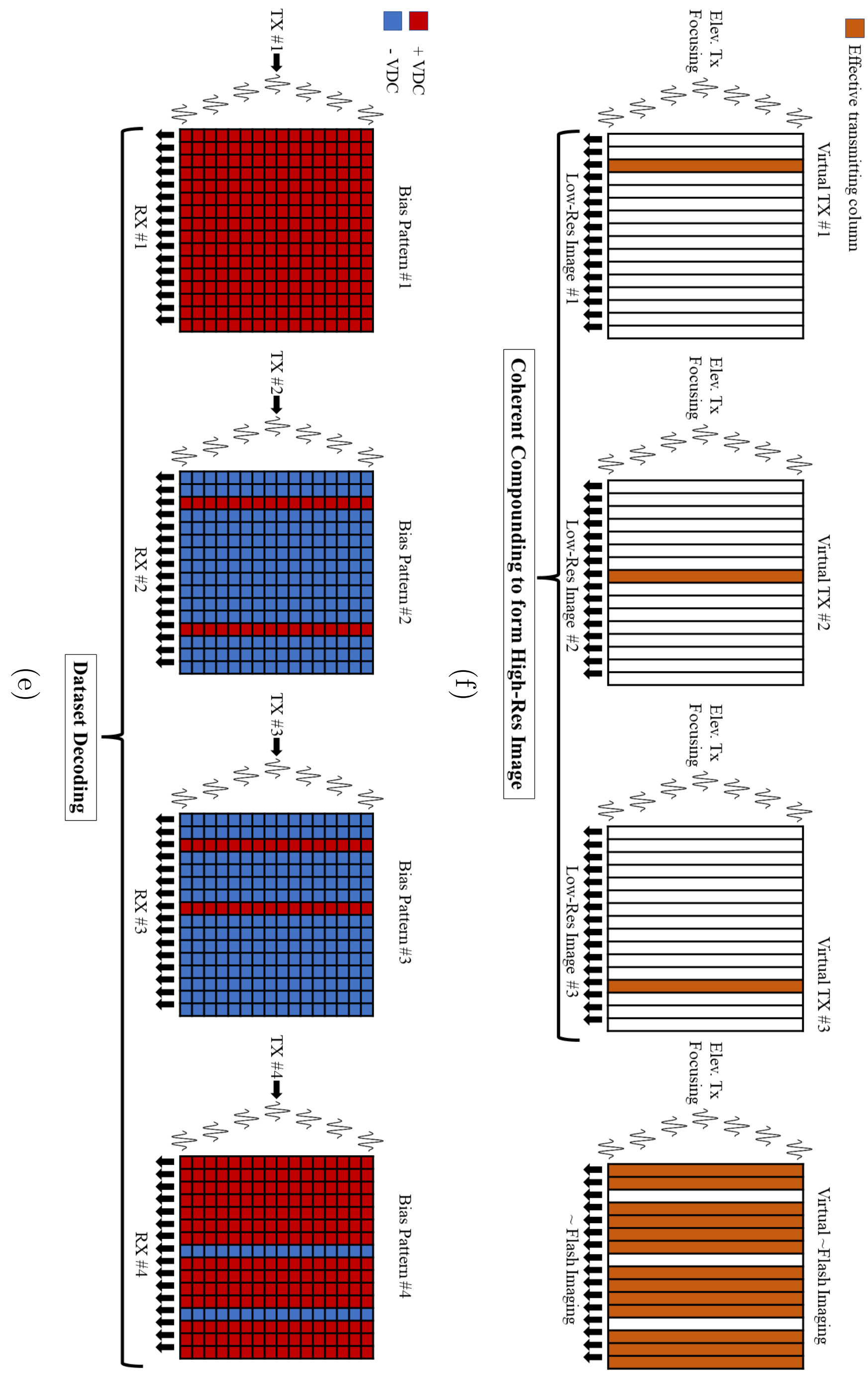

Figure 4.2: uFORCES imaging scheme illustrated with a 16×16 TOBE array using 4 transmits (4 bias patterns). (a) Column groupings for arbitrarily selected sparse transmitters, (b) Schematic of the top and bottom electrodes and their bias tees, (c) 4×4 Hadamard matrix for this example. One column of the Hadamard matrix is used as a biasing pattern for each transmit event. (d) Applied coded bias voltage pattern associated with bias pattern 2, (e) Illustration of the uFORCES imaging scheme for all the bias pattern sequences with transmitting on the rows and receiving on the columns, (f) sparse synthetic aperture effective dataset and reconstruction scheme after aperture decoding with an inverse Hadamard matrix.

Table 4.1: Parameter Used in Field II Simulations

Parameter	Value
Speed of sound	1540 m/s
Center frequency	10 MHz
Sampling frequency	100 MHz
Kerf	15 μm
Pitch	150 μm
Number of excitation cycles	1
2D array size	128×128

patterns for each transmit/receive event. For a 128×128 TOBE array, FORCES uses 128 transmit/receive events. Decoding the data (using an inverse Hadamard matrix) recovers a full transmit-receive synthetic aperture imaging (SAI) dataset for the columns of the TOBE array. The role of the rows and columns can be interchanged to create cross-plane imaging. Electronic steering enables acquisition of a 3D image.

uFORCES is introduced here as an ultrafast variant of FORCES using TOBE arrays. uFORCES will enable steerable B-scan acquisition with only a few transmit events while achieving near-ideal synthetic aperture transmit and receive focusing everywhere in the image. Here, we describe the uFORCES approach and demonstrate using simulations that uFORCES with TOBE arrays has the potential to achieve improved in-plane resolution and comparable out-of-plane resolution as state-of-the-art matrix probes relying on micro beamforming.

Fig. 4.2 illustrates the uFORCES scheme for a 16×16 TOBE array. FORCES would require as many transmit/receive events as columns in the array. However, our proposed uFORCES approach can achieve imaging with fewer transmit events. In this method, we select sparsely-spaced columns as the desired transmitters. One might wonder if we could transmit on a single column at time. However, the problem is that if we only biased one column and transmitted along rows for elevational focusing, the unbiased columns would be insensitive to receiving signals. Instead, we bias all the columns, but with a set of bias patterns. In this way, we can receive signals from every column after each transmit event. Previously we did this with bias patterns selected from rows or columns of a Hadamard matrix [1]. In uFORCES, however, we first group elements into grouping including sparse transmitters and remaining element groupings. In Fig. 4.2 (a) we choose columns 3, 8, and 13 as sparse transmitters and all the remaining elements as a fourth grouping. Here we arbitrarily use columns 3, 8, and 13 as sparse transmitters for illustrative purposes (as they are separated by a regular interval, in this case 5 columns) but other choices are possible. As before, delayed pulses are sent on the rows to focus the beam in elevation. However, instead of selecting bias patterns from an $N \times N$ Hadamard matrix for an $N \times N$ TOBE array, (in this case $N=16$), we now select bias patterns from a smaller (e.g. $M \times M$, where $M<N$) Hadamard matrix. In this example, we do this with a 4×4 Hadamard matrix. For example, the second column of a 4×4 Hadamard matrix is [1 -1 1 -1]. Thus we apply positive, negative and positive bias voltages to sparse transmitting columns on columns 3, 8, and 13. Then, we apply a negative bias voltage to all remaining elements as illustrated in DC Pattern #2 in Fig. 4.2 (d). We apply a biasing pattern in this manner for each of 4 transmit events. After the complete set of transmit events has been sent, recovered column channel data (inverted when acquired from a negatively biased column) is aperture-decoded using the inverse of the 4×4 Hadamard matrix. This then recovers a column data synthetic aperture dataset. As shown in Fig. 4.2 (f), for this example, it recovers channel data as if column 3 first transmitted (with an elevational focus) then data was received on all columns, then column 8 then column 13. A final dataset is recovered which is similar to a plane wave excitation with some of the sparse columns missing (however it is not used in the beamforming). The synthetic aperture datasets are then reconstructed to form a synthetic aperture image which is focused in transmit and receive everywhere in the scan-plane. This is accomplished by beamforming a low-resolution image from each sparse-transmitting element then coherently compounding the low-resolution images to form a high-resolution image.

Steering the scan-plane in elevation is also possible when acquiring a volumetric image. In previous sparse synthetic aperture imaging work using linear arrays, as few as 5 sparse transmitting elements had been shown to produce image quality comparable to full synthetic aperture imaging[80]. Thus in what follows we will use uFORCES with 8, 16 or 32 groupings. An 8-transmit uFORCES scheme would recover a synthetic aperture dataset with 7 sparse transmitting columns.

While our approach requires far fewer transmit events than FORCES, there will be a trade-off between imaging speed and SNR. The higher the imaging speed, the lower the SNR would be since the effective active aperture with only a few sparse transmitting elements is small. The image quality can be dynamically changed during the imaging by adjusting the number of transmit events where needed.

The comparison is conducted in Field II [89] with 128×128 arrays with parameters summarized in Table 4.1. To form a top-orthogonal-to-bottom-electrode (TOBE) array, the RF signals of each element on the columns and rows are added up. The effect of the DC bias switching for each pattern was applied to each individual element in Field II by alternating the index of the apodization between 1 and -1 denoting positive and negative bias voltages, respectively. Additionally, this apodization is modified with a hamming-weighted shape, which is shown to reduce the artifacts caused by side lobes compared to the unity-weighted apodization. The hamming-shaped apodization can potentially be implemented by tapering the electrodes during the fabrication of the TOBE arrays.

4.2.2 Matrix Probe

In this paper, the matrix probes are considered as a 2D fully connected array which performs a walking aperture imaging scheme with either wide or narrow focused transmit beams and with narrow dynamic-receive beamforming used in reception. In practice, the considered walking aperture implemented on a fully-connected 2D array will perform better than an actual matrix probe as no microbeamformer approximation is used. This was done to demonstrate the best-possible performance of a matrix probe for comparison against our uFORCES simulations with TOBE arrays. As mentioned, the matrix probes used receive focusing with a dynamic quadratic delay profile as constrained by the paraxial approximation. This approximation limits reconstructions to f-numbers greater than unity without reconstruction artifacts. In contrast, our uFORCES synthetic aperture approach required no such restrictions.

4.2.3 Imaging Targets

The imaging simulations are conducted on two different phantoms. The first phantom, which is composed of 15-point scatterers located at depths of 15, 20, 25, 30, and 35 mm (on- and off-axis by 3 mm), was used for the simulation. However, the on-axis scatterers were only used for calculating the point spread functions (PSFs) and associated spatial resolution for each imaging scheme. Another phantom with 100,000 scatterers and different cyst sizes was used for comparing the contrast and contrast-to-speckle ratio (CSR). The simulations were performed on a computer with a 6-core processor and a 32 GB of memory. However, due to the slow simulation, only walking aperture and uFORCES imaging were performed on the cyst phantom by knowing that FORCES would give almost the same resolution as uFORCES with some improved SNR due to the more signal averaging in the coherent compounding.

The contrast-detail phantom images of different imaging schemes are compared with each other in terms of contrast and contrast-to-speckle ratio (CSR), which are calculated using the following expressions [90]:

$$\mathrm{CSR} = \frac{\mu_{\mathrm{in}} - \mu_{\mathrm{out}}}{\sqrt{\sigma_{\mathrm{in}}^2 + \sigma_{\mathrm{out}}^2}} \tag{4.1}$$

$$\mathrm{Contrast} = \frac{\mu_{\mathrm{in}} - \mu_{\mathrm{out}}}{\mu_{\mathrm{out}}} \tag{4.2}$$

in which μ_{in} and μ_{out} are the average signals inside and outside of the area of interest, respectively, and σ denotes the standard deviation.

4.3 Experimental Methods

4.3.1 Bias-Sensitive Ultrasound Transducer Based on PMN-PT

Bias-sensitive TOBE arrays allow for coding/decoding the aperture to be able to address each column and row individually by using i.e. Hadamard matrix biasing. Unlike the piezoelectric materials, the bias-sensitive ultrasound transducers made of electrostrictive materials show no piezoelectricity effect unless a DC bias voltage is applied [1, 2]. Lead magnesium niobate (PMN) with low lead titanate (PT) doping is a electrostrictive material that is naturally unpolarized at around room temperature and becomes polarized by applying a DC bias voltage (PMN38, TRS Technology). These materials can also be made transparent/translucent when polished on both sides that potentially can be used in through-illumination photoacoustic applications [51, 91, 92]. Capacitive micromachined ultrasound transducer (CMUT) is another bias-sensitive transducer that uses electrostatic forces between two clamped plates to generate acoustics which some of their applications in TOBE configurations have been demonstrated recently [47].

In this work, a 128×128 electrostrictive TOBE array was fabricated to perform uFORCES imaging. This is the largest such TOBE array fabricated to date. The fabrication was conducted with steps similar to those previously described [48] for 64×64 arrays. As shown in Fig. 4.3, the transducer is composed of a PMN-PT/epoxy composite material sandwiched in between top and bottom electrodes which are orthogonal to each other. A quarter-wavelength parylene-C layer was deposited on top as the matching layer and a thick alumina-loaded epoxy on the back serves as backing layer. Transducer fabrication was performed in the University of Alberta nanoFAB facility. The fabricated array was wire-bonded to a printed circuit board on both the front- and back-sides, which was then connected to an interfacing board connected to our Verasonics Vantage ultrasound platform for testing and imaging. Custom high-voltage biasing electronics were used to apply bias patterns as controlled by the Verasonics system.

4.3.2 Array Characterization and Testing

Prior to Parylene-C deposition, the bias-sensitivity of the fabricated transducer was tested by measuring the input impedance for a few different DC biases. The bias-sensitivity for a smaller array was demonstrated previously in [2].

To measure the impedance of the array, we used a Keysight E4990A impedance analyzer and recorded both the magnitude and phase as a function of frequency in an air environment. A bias tee (Minicircuits ZFBT-4R2GW-FT+) was used to apply varying bias voltages for experiments. In performing these experiments we grounded all connections on one side of the array while testing one channel on the other side. These data were used to calculate the resonance (ω_s) and anti-resonance (ω_p) frequencies and the associated electromechanical coefficient, k_t, as follows [93]:

$$k_t = \sqrt{\frac{\pi\omega_s}{2\omega_p}\tan\left(\frac{\pi(\omega_p - \omega_s)}{2\omega_p}\right)} \tag{4.3}$$

4.3.3 Bias Switching Electronics

A custom-made bias-switching electronics board was used for biasing the fabricated array. Each channel on the rows and columns is connected to a set of high-voltage MOSFET-based switches controlled by a 2 to 4 decoder. So each channel can be individually programmed to get four stages: positive high voltage, negative high voltage, ground, and high impedance (open circuit). A bias tee made of a capacitor and a resistor is used for each channel. The DC bias voltages from the dedicated electronics switches get to the channels through the resistors of the bias tees. The capacitor on the bias tee blocks the DC voltages from reaching the Verasonics platform while letting the Tx and Rx signals pass through it. The bias-switching electronics can switch from -175 V to +175 V in 648 ns without load[94]. However, this switching speed

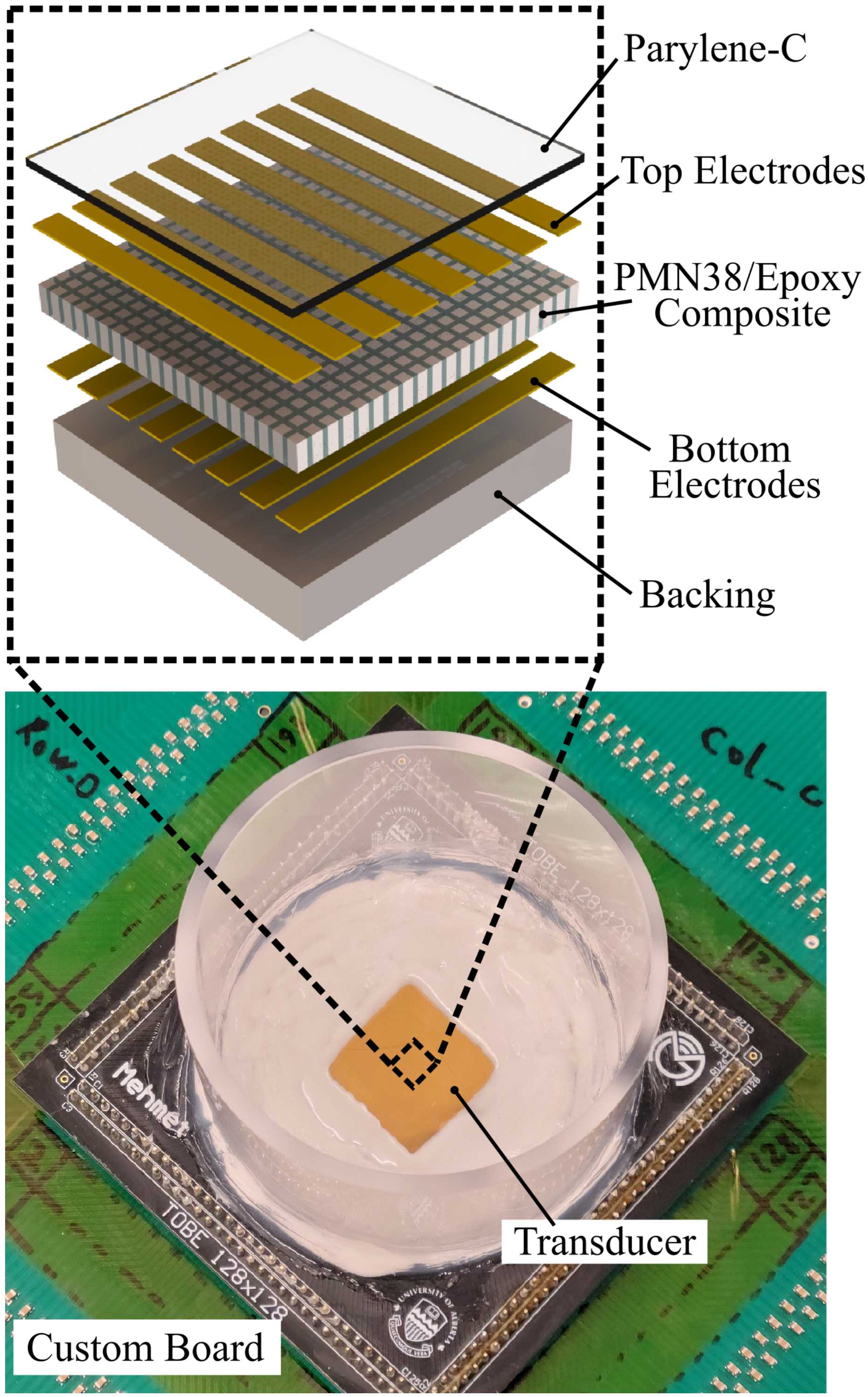

Figure 4.3: The Photograph of the fabricated 128×128 TOBE array with the schematic exploded view showing its cross section.

drops to 300-400 μs when the array is connected to the biasing board, constrained by the high-value resistors used in the bias tees.

4.3.4 Channel Mapping

A script was written to find shorted elements in fabricated TOBE arrays. It applies a bias voltage to one channel at a time and grounds all other rows/columns. The high-voltage power supply has a current limit set to about 5 mA.

The script loops through all channels defined for the transducer and the user is asked to make a decision for each channel whether the channel is shorted or not. Usually, a channel is considered to have no shorts if current drawn is less than 1 mA. Once the mapping procedure is finished, any shorted channel are set to a high impedance state to prevent damage to the electronics or array during imaging.

4.3.5 Immersion Testing and Imaging Experiments

To test the arrays for uFORCES imaging, we glued a water-tank to the PCB with transducer, and conducted immersion experiments using a Verasonics Vantage 256 system.

We first characterized the transducer by performing a pitch-catch experiment using single-channels. This experiment was used to characterize the center frequency and the bandwidth of the array.

Next, We imaged cross-wire targets consisting of three 25 μm wire-bonding wires with approximately 5 mm spacing, and the middle wire being 90-degrees rotated from the others. The purpose of these experiments was to demonstrate preliminary evidence that the uFORCES methods with TOBE arrays could achieve high-resolution images experimentally. We also imaged a tissue-mimicking phantom made of 85% water, 10% gelatin, and 5% cornstarch with a 6 mm-diameter hole in the center.

4.4 Results and Discussion

4.4.1 Simulated Point Spread Functions

Fig. 4.4 illustrates the PSFs of different imaging schemes simulated in Field II with a 128×128 array. All the images are plotted in 50dB dynamic range. The matrix probe walking aperture schemes use narrow dynamically-focused reception with an applied 2D Hanning apodization. We used both narrow and wide transmit beams without any apodizations. The narrow beam was created by using the entire active 128×128 elements, while for the wide beam, only 32 elements in the center were used. Both wide and narrow transmit/receive beams focused at 25 mm depth. We reconstructed images with 501 A-scan lines. However, to compare with sparse-transmitting uFORCES schemes, we considered reducing the number of transmit events. We tested 501, 24, and 8 transmit event imaging using these matrix simulations.

The images obtained by FORCES and uFORCES methods used three elevation (and azimuthal) focusing depths at 15, 25, and 35 mm. Images acquired using these different transmit focal depths were then stitched together using a Gaussian-weighted blending algorithm.

The FORCES scheme requires 128 biasing patterns multiplied by 3 focal zones for an overall 384 transmit/receive events. In contrast the 8-transmit uFORCES scheme only requires $8\times3 = 24$ transmit/receive events making it 16 times faster.

The calculated lateral and axial resolutions for the PSFs are summarized in Table 4.2. The axial and lateral resolutions are estimated with an error of ±2 μm and ±5 μm, respectively. As can be seen, uFORCES PSFs in Fig. 4.4(g) and (h) are similar to FORCES PSFs in (e) and (f). Apodization helped reduce some edge-wave reconstruction artifacts. Lateral Spatial resolution of FORCES and uFORCES reconstructions was improved compared to matrix probe simulations using wide or even narrow transmit beams.

To assess the elevational scanning performance of the uFORCES scheme, we per-

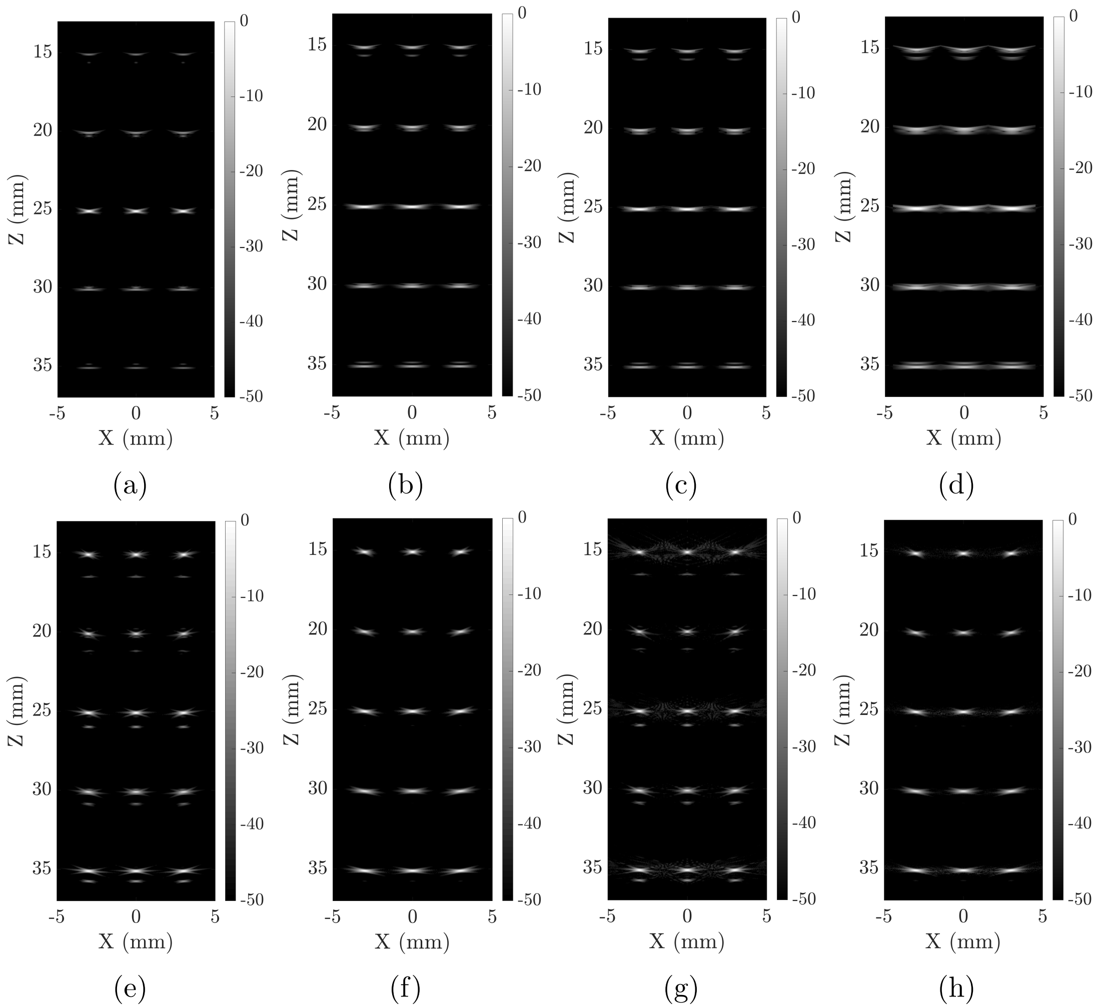

Figure 4.4: In-plane PSFs of different imaging schemes; (a) matrix probe with narrow transmit beam of 501 transmit events, (b) matrix probe wide with wide beam of 501 transmit events, (c) matrix probe with wide beam of 24 transmit events, (d) matrix probe with wide beam of 8 transmit events, (e) FORCES without apodization with 384 transmit event, (f) FORCES with apodization with 384 transmit events, (g) uFORCES without apodization with 24 transmit events, (h) uFORCES with apodization with 24 transmit events

formed simulations to render the YZ-scan plane of a TOBE array in comparison to a matrix probe. The results are shown in Fig. 4.5. In the uFORCES simulation in Fig. 4.5(a), we used three elevational transmit focal zones as discussed above and used 8 transmit events per focal zone. As can be seen, elevational spatial resolution was comparable to the matrix probe but the uFORCES scenario exhibited more reconstruction artifacts since unfocused receive elements were used in elevation. Nevertheless, transmit elevational focusing, including using three elevation focal zones, produce reasonable elevation point-spread functions given limitations of row-column only addressing.

4.4.2 Contrast-Detail Phantom Simulations

The walking aperture simulation was first done on the phantom with a narrow beam and single focus point at 20 mm depth. 601 lines were scanned between -6 to 6 mm lateral distance (x-axis) to form a 2D image of the phantom. We also simulated a wide transmit beam using the same number of transmit events, and wide-beam excitation using 24 and 8 transmit events along with parallel beamforming (Fig. 4.6). These fewer number of transmit events was simulated to compare against uFORCES schemes having 8 and 24 transmit events. Time-gain compensation was applied to achieve roughly uniform brightness with depth. Vertical stripes are seen in some of the wide-transmit-images owing to multiple receive lines reconstructed for each wide transmit event. Commercial systems will undoubtedly use improved blending in post-processing to ensure a more uniform image quality but this was not pursued in this paper for simplicity.

Since the simulations of such a large phantom was quite slow, only uFORCES imaging (which required fewer transmit-receive events than FORCES) were performed on the cyst phantom with 3 focal zones (and 8 transmits per zone) for a total of 24 transmit/receive events as shown in Fig.4.7.

The contrast and contrast-to-speckle ratio for both uFORCES and matrix probe simulations are presented in Table 4.3. Visually, uFORCES simulations look crisper owing to improved spatial resolution. Note that the measured contrast and contrast-to-speckle ratios are not better for uFORCES compared to the matrix probe for the middle lesions since this is where the matrix probe is focused on both transmit and receive. However, for the top and bottom lesions, contrast is improved or similar for uFORCES compared to the matrix simulations, and CSRs are similar.

4.4.3 Impedance Testing

The unloaded input impedance of the fabricated transducer with an applied DC bias of 120 V is demonstrated in Fig. 4.8. The fabricated transducer showed a maximum k_t value of $\sim$0.67 for a voltage of 120 V. As expected, the fabricated bias-sensitive TOBE array shows no piezoelectric effect for a 0 V bias voltage while the sensitivity and polarity scale with the bias voltage amplitude and polarity as reported in Fig. 4 in[2].

4.4.4 Pulse-Echo Testing

Fig. 4.9 shows results from an immersion transmit test, where a single channel of the array was used to transmit ultrasound, which was reflected from an aluminum plate to be received by the same channel. To this end, a pulser/receiver with an excitation spike voltage of -180 V and a receive gain of 10 dB at a frequency range of 5 to 20 MHz was used (PANAMETRICS-NDT, 5073PR). The center frequency of the array was measured to be 13.6 MHz with -6 dB bandwidth of 51%.

4.4.5 Experimental Crossed-Wire and Phantom Imaging

Experimental imaging of wire targets was done with a fabricated 128×128 TOBE array using bias voltages of $\pm 100V$. uFORCES was implemented using a custom imaging script which sent bias-voltage patterns to custom 256-channel high-voltage biasing electronics. The image shown in Fig. 4.10 was obtained by stitching images

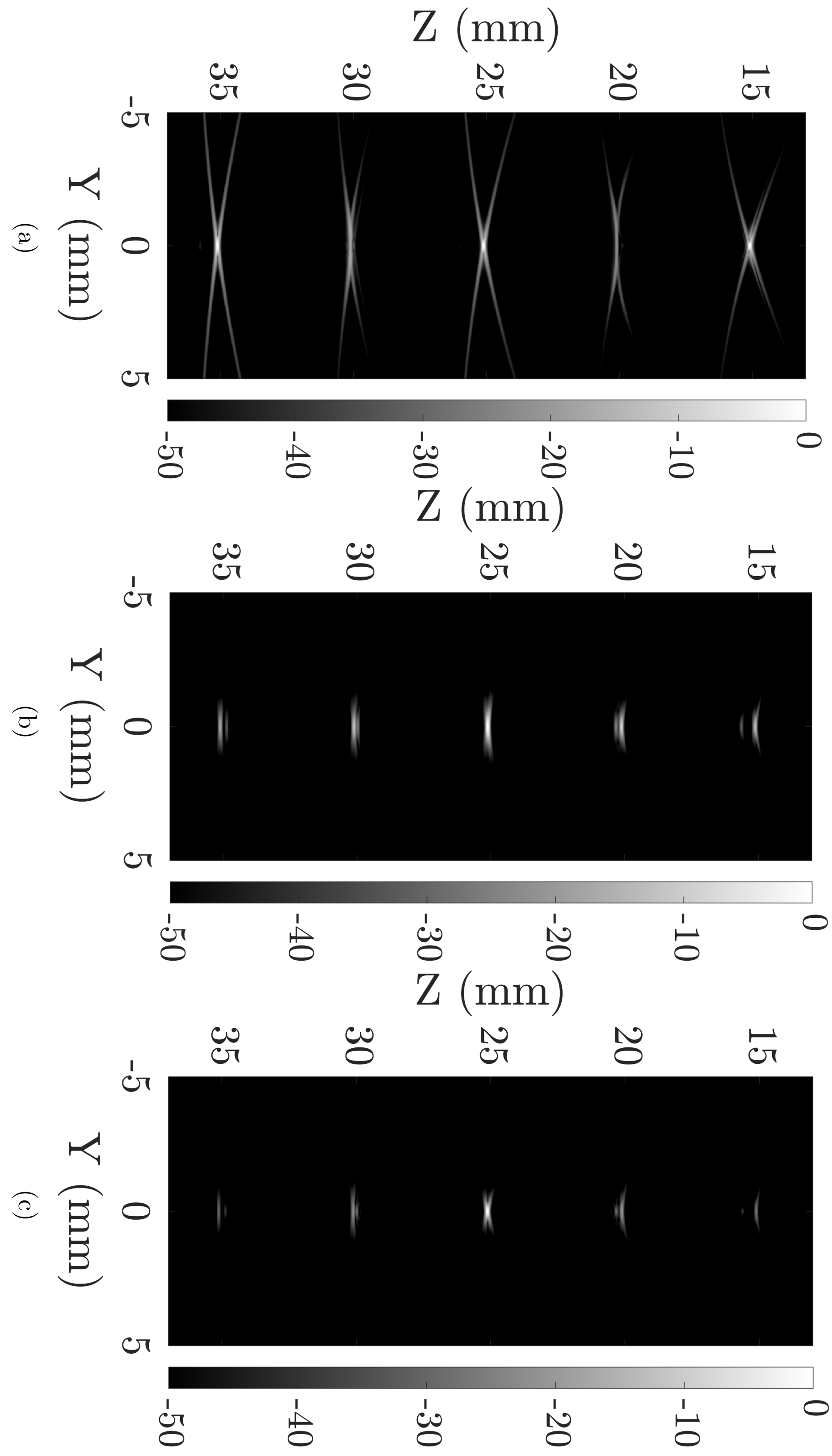

Figure 4.5: Elevationally scanned (YZ) plane imaging comparisons using (a) a 128×128 λ-pitch TOBE array and uFORCES, (b) 128×128 matrix probe using a wide beam excitation in azimuth, (c) 128×128 matrix probe with narrow beam excitation in azimuth.

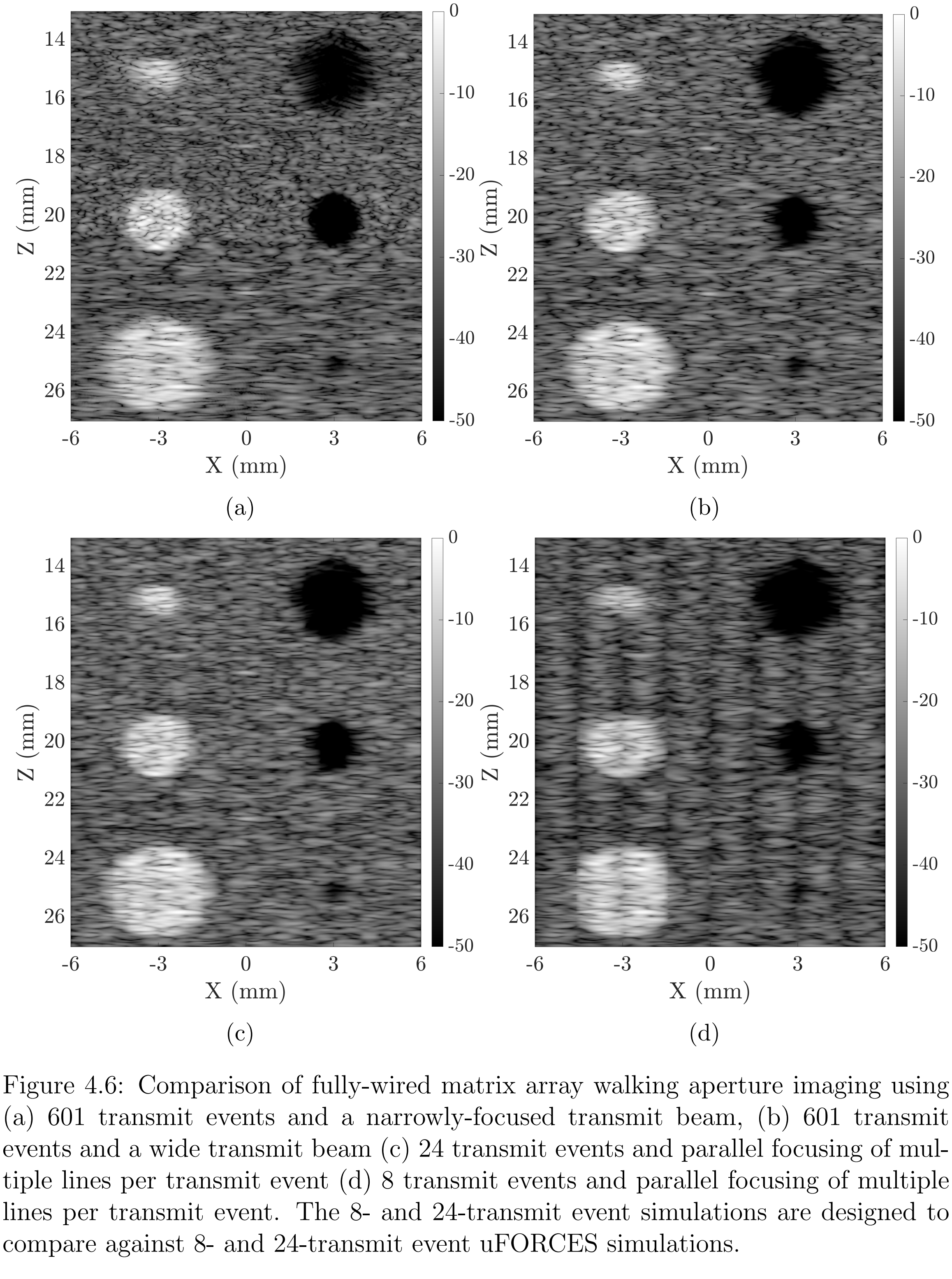

Figure 4.6: Comparison of fully-wired matrix array walking aperture imaging using (a) 601 transmit events and a narrowly-focused transmit beam, (b) 601 transmit events and a wide transmit beam (c) 24 transmit events and parallel focusing of multiple lines per transmit event (d) 8 transmit events and parallel focusing of multiple lines per transmit event. The 8- and 24-transmit event simulations are designed to compare against 8- and 24-transmit event uFORCES simulations.

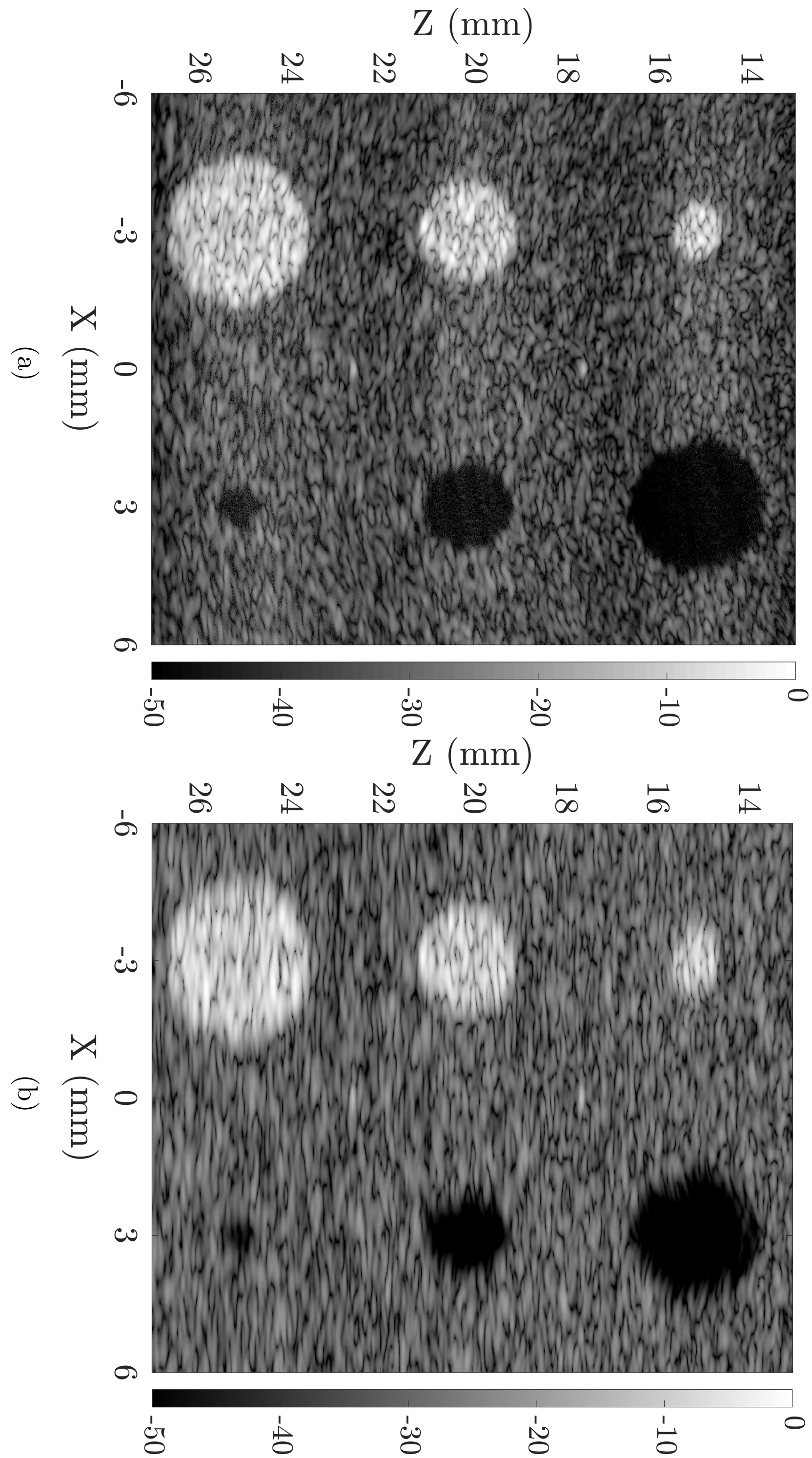

Figure 4.7: Simulated comparisons of a contrast detail phantom imaged using (a) TOBE uFORCES and (b) matrix probe wide-beam walking aperture. In both cases a 10 MHz 128×128 lambda pitch array was used but the TOBE array used only row- and column addressing. Here the uFORCES simulation used 8 transmit events per focal zone, and stitched results from 3 elevational focal zones. This required a total of 24 transmit events, with coherent compounding needed over only 8 transmit events.

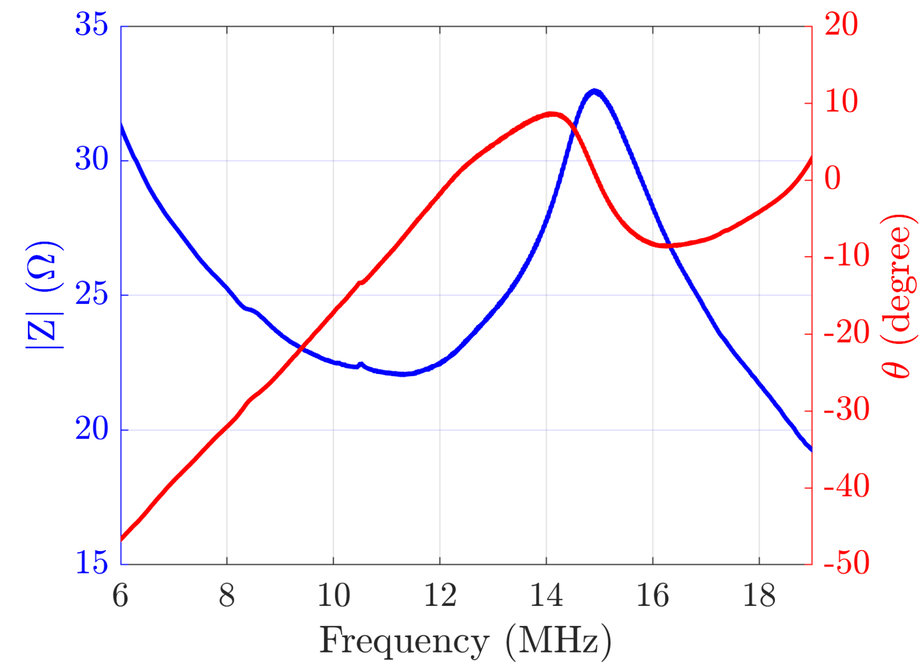

Figure 4.8: Impedance measurement of a single channel of the fabricated arrays done in air.

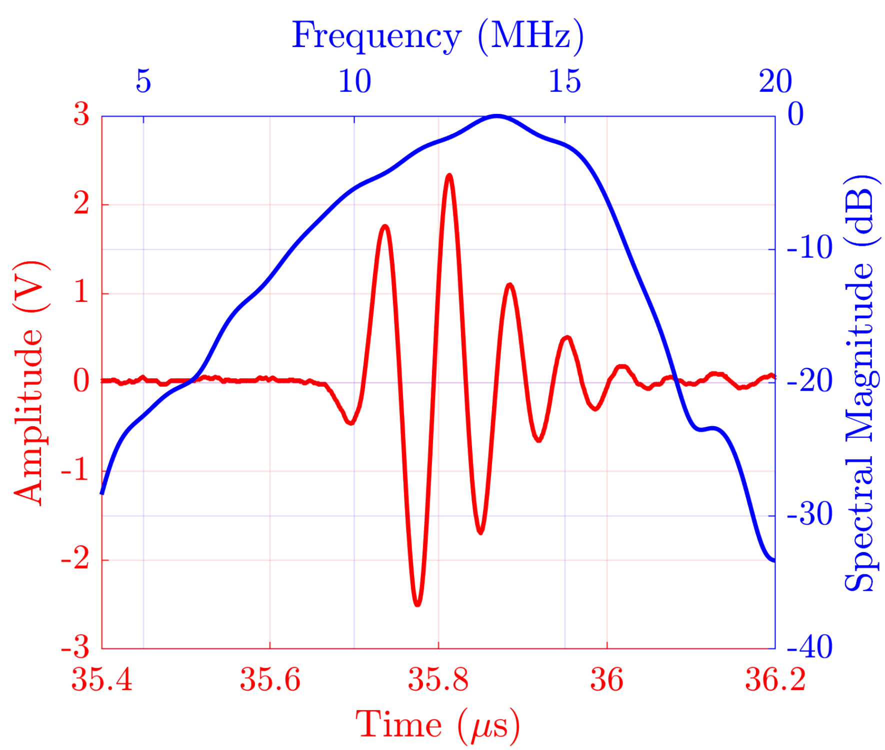

Figure 4.9: Temporal and frequency response of a single channel from the fabricated array in pulse-echo experiment.

with three different transmit elevational focal zones. Here we implemented uFORCES with 32 transmits per elevational focal depth. This array had 20-25 dead elements per side and improved results are expected with an improved array. We also performed the same imaging scheme on a tissue-mimicking phantom with a hole in the center. uFORCES with 32 transmit events and an elevantional focal zone at 16 mm was used for the imaging as shown in Fig. 4.11. This is the preliminary result obtained by an array with a considerable number of the channels shorted. A higher quality image is desired with a well performing array.

4.5 Conclusions

This chapter introduces ultrafast orthogonal row-column electronic scanning (uFORCES) as a means to form images much faster than with FORCES, but with little degradation in image quality. Whereas FORCES requires N transmit events for an N×N array, uFORCES requires less, and we used as few as 8 such transmit events for a 128×128 TOBE array. This represents a speedup of 16-fold using uFORCES compared to FORCES for this array.

Our uFORCES simulations demonstrate improved in-plane spatial resolution compared to similar dimension fully-wired matrix probes with a walking aperture imaging scheme. We believe this can be explained by two key reasons. First, uFORCES effectively implements in-plane synthetic aperture imaging, which achieves focusing in transmit and in receive everywhere in the scan plane. This is in contrast to the scanning scheme used by our matrix probe simulations, where a single transmit focal depth is used per transmit event, and away from this focal zone, the transmit wave is unfocused. Second, the matrix beamforming is limited to a quadratic delay profile as constrained by the paraxial approximation. As such, focusing is not well achieved without artifacts for f-numbers smaller than unity. In contrast, uFORCES achieves synthetic aperture imaging, which is not limited by the paraxial approximation and can achieve fine focusing even for low f-numbers.

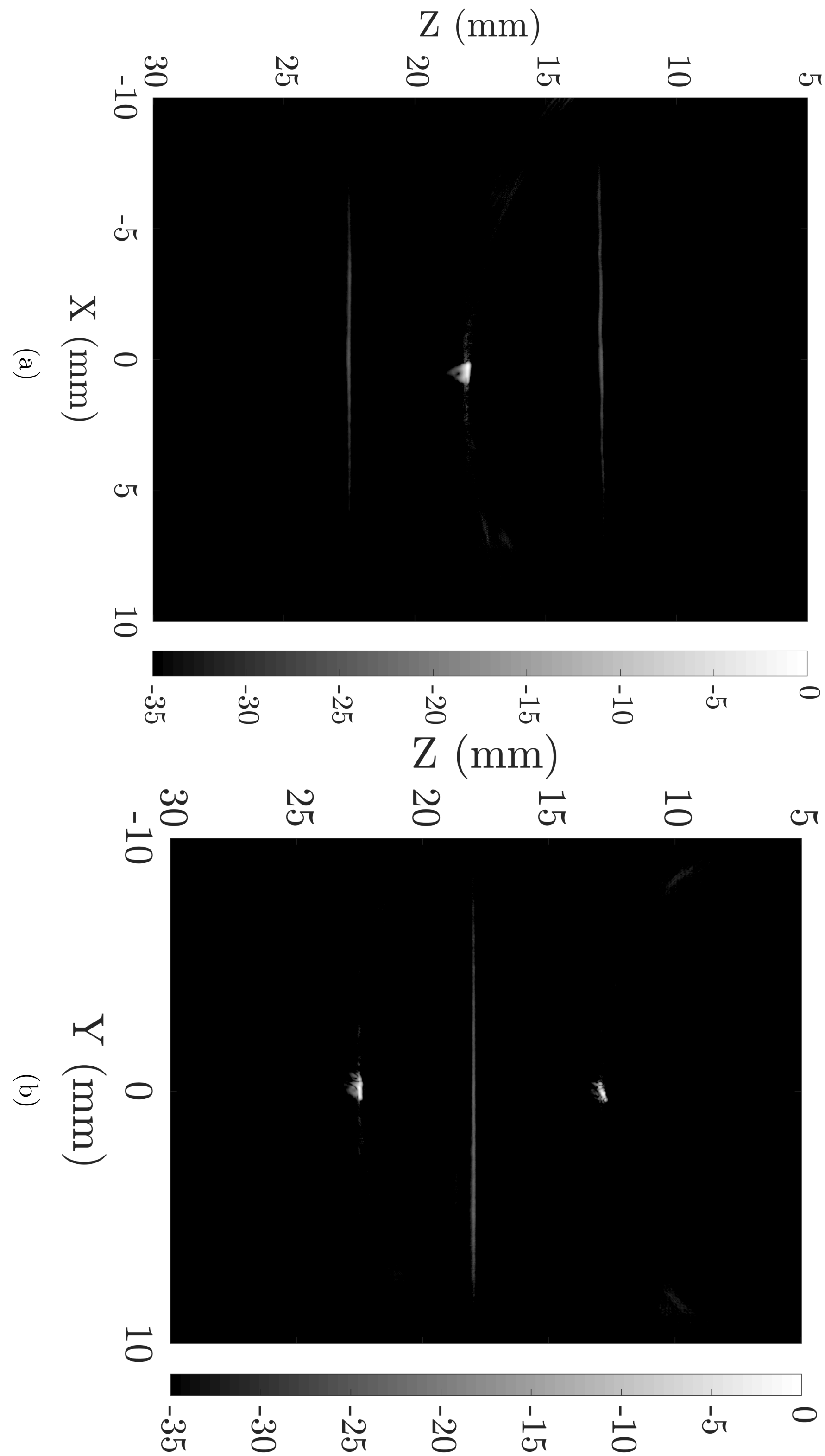

Figure 4.10: Experimental cross-plane uFORCES images of a cross-wire phantom using 32-transmits per elevational focal zone and three such focal zones at 12, 18, and 22 mm depths, (a) XZ-plane, (b) YZ-plane. These images were obtained by electronically reversing the roles of rows and columns and were obtained without mechanically moving the transducer.

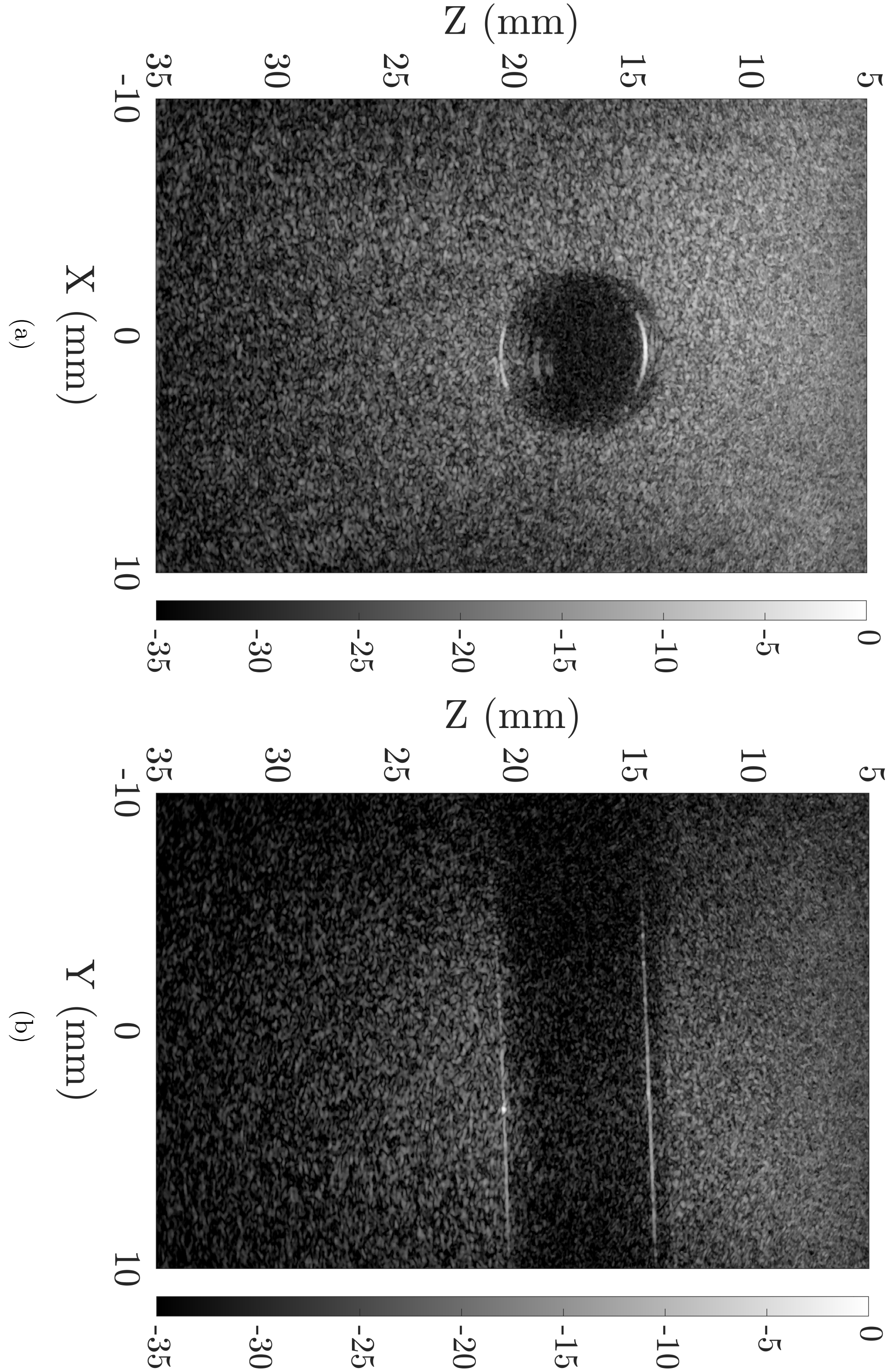

Figure 4.11: Cross-plane experimental uFORCES image of a tissue-mimicking phantom using 32-transmits with elevational focal zone at 16 mm depth, (a) XZ-plane, (b) YZ-plane. These images were obtained by electronically reversing the roles of rows and columns and were obtained without mechanically moving the transducer.

Elevational focusing with uFORCES is seen to exhibit more beamforming artifacts compared to matrix simulations but resolution is comparable. uFORCES is limited by unfocused elevational receive elements, even though there is an elevational transmit focus. As such, we used multiple elevational transmit focal zones to improve the depth of field. It should be noted that elevation stitching using multiple transmit focal zones could be achieved without the need for coherent compounding. Thus, even though we used a total of 24 transmit events, coherent compounding was needed over only 8 such transmit events. This is important as tissue motion can lead to degradation of coherent compounding unless it can be done quickly relative to tissue motion.

With current bias tees with a switching time of 300-400 μs, we achieved an imaging rate of >300 fps when using 8-transmit uFORCES. With future improvements in bias switching electronics, we anticipate thousands of frames per second. Thus, with improved electronics and bias tees, 8-transmit uFORCES with an 8 kHz PRF, would result in kHz B-scan imaging rates. In principle matrix probes can transmit wide beams and execute parallel receive focusing to reconstruct many lines at once. However, the fine delays in the microbeamformer stage are technically valid for a single receive line-of-sight, and the more parallel beamforming the worse the reconstruction error.

In practice, matrix probes will probably not use the walking aperture scheme simulated here. They will likely use all the elements and implement a sector-scanning approach. However, sector-scanning will lead to even more artifacts owing to grating lobes becoming more significant at higher steering angles. The purpose of using a walking aperture scheme here was to compare TOBE uFORCES against the best possible theoretical matrix probe and associated imaging scheme.

Imaging advantages over matrix probes are only demonstrated in simulation for now. These simulations further included array apodization. This apodization was not yet implemented in array fabrication, but work is underway to do so. Such apodization is important to mitigate edge-wave artifacts and improve imaging point-spread functions.

Experiments were conducted with un-apodized 128×128 arrays. Fabrication of these large arrays was found to be highly non-trivial and the tested arrays had 20-25 shorted or dead channels per side, which was a source of some image quality degradation. If a robust fabrication procedure for large TOBE arrays can be developed, these arrays could hold great promise for significant developments in pre-clinical and clinical imaging applications.

Signal-to-noise is degraded using uFORCES compared to FORCES since uFORCES uses a sparse synthetic aperture imaging scheme. Strategies for improving signal-to-noise ratio should be investigated in future work, and could include coded excitation schemes, element binning, etc.

2D arrays for high-frequency applications do not yet exist commercially. Our technology could achieve this and lead to advances in pre-clinical ultrasound.

Our current experimental results were achieved using a tabletop testbed setup with an integrated water-tank. This enables rapid prototyping of new arrays and new imaging schemes, but is not yet practical for imaging. Future work should develop handheld, endoscopic, and other form factors for clinical and pre-clinical applications.

TOBE arrays, unlike matrix probes, also have great potential for scaling up to large arrays of unprecedented size. For this, a robust fabrication process is needed. If successful, this could lead to better deep imaging because the numerical aperture will be improved. It will also enable greatly expanded fields of view and we envision future large 1024×1024 or larger arrays for whole organ imaging.

For TOBE probes and uFORCES to be realized, non-trivial fast bias-switching electronics are needed, which are absent in conventional ultrasound systems. While there will be additional development complexity and cost associated with these electronics, they can be used with any TOBE array. By taking the electronics complexity out of the probe head, it should greatly simplify the development costs of the probes.

TOBE arrays are additionally simple enough to be wearable. This prospect could

Table 4.2: In-Plane SNR and Resolution Measurements for each Imaging Scheme with and without the Noise

Scheme	Total Number of Transmits	Point distance (mm)	Lateral FWHM Resolution (μm)	Axial FWHM Resolution (μm)
Walking Aperture (Narrow Beam)	501 (Focusing at 25 mm)	15	544	92
		20	556	91
		25	284	95
		30	334	91
		35	706	91
Walking Aperture (Wide Beam)	501 (Focusing at 25 mm)	15	476	100
		20	488	93
		25	528	995
		30	598	94
		35	658	93
	24 (Focusing at 25 mm)	15	554	94
		20	570	97
		25	588	97
		30	648	95
		35	722	94
FORCES	3×128 (Focusing at 15, 25, 35 mm)	15	266	101
		20	258	93
		25	340	99
		30	384	100
		35	410	96
uFORCES	3×8 (Focusing at 15, 25, 35 mm)	15	233	114
		20	256	94
		25	296	94
		30	370	96
		35	390	93

open up opportunities for longitudinal imaging that were previously not possible.

Future work should take advantage of the ultrafast imaging capabilities demonstrated with uFORCES for novel flow-imaging and shear-wave imaging opportunities.

For the full potential of TOBE arrays to be realized, highly-parallelized computing architectures will be needed which may be absent on even state-of-the-art ultrasound platforms. However, the massive explosion of GPU-computing accelerated by the deep-learning era will surely prove essential to future high-resolution, massive field-of-view 3D and 4D imaging technologies of the future. We envision that TOBE array technology will be an important component of this future wave. Successful realization of uFORCES depends on several practical factors. Ideally, the sensitivity of elements will be uniform but practically, process variations may lead to different responses from different elements. These variations may lead to image quality degradation. Calibration and compensation algorithms could help mitigate some of these problems. Shorted channels could be a source of imaging artifacts. In practice, we assigned the shorted channels to high impedance with our custom bias-switching electronics.

As a conclusion for this chapter, we have simulated and experimentally-demonstrated our newly proposed uFORCES imaging scheme using 128x128 TOBE arrays. One might presume that since these arrays provide only row- and column addressing the achievable image quality might be compromised compared to a fully-wired matrix probe with integrated microbeamformers. However, we have shown the opposite, since our approach can achieve transmit and receive focusing everywhere in the scan plane and since we are not limited by the paraxial approximation. Also, in traditional imaging schemes, beamforming is done by keeping the f-number constant for different imaging depths to provide a uniform resolution and prevent imaging artifacts for smaller f-numbers. However, our implemented FORCES and uFORCES imaging schemes provide SAI, which technically, everywhere in the imaging plane is in focus during the transmit and receive and is not limited to f-number. Moreover, our approach can achieve ultrafast imaging rates, unlike matrix probes. With these

Table 4.3: Comparison of uFORCES and matrix probe in Cyst Phantom Simulation in terms of Contrast and Contrast-to-speckle Ratio

Scheme	Cyst Phantom											
	Z = 15 mm				Z = 20 mm				Z = 25 mm			
	Left		Right		Left		Right		Left		Right	
	Contrast	CSR	Contrast	CSR	Contrast	CSR	Contrast	CSR	Contrast	CSR	Contrast	CSR
Narrow Beam	6.7	1.4	-0.8	-1.3	13	1.4	-0.8	-0.8	8.1	1.5	-0.5	-0.6
Wide Beam (601)	7.6	1.4	-0.8	-1.4	11.2	1.6	-0.7	-0.9	8.4	1.6	-0.5	-0.7
Wide Beam (24)	7.6	1.4	-0.8	-1.4	11.3	1.6	-0.7	-0.9	8.4	1.6	-0.5	-0.7
Wide Beam (8)	5.1	1.4	-0.8	-1.4	11.9	1.4	-0.6	-0.6	9	1.5	-0.5	-0.6
uFORCES	10.5	1.4	-0.8	-1.1	8.9	1.4	-0.7	-0.9	8.6	1.6	-0.5	-0.6

promising results, we believe that there is a bright future for TOBE arrays as a potential candidate to finally provide clinicians with the 3D image quality they need. We also envision a future with large-scale and wearable TOBE arrays, which will bring new opportunities for the future of medicine.

With some of the approaches for improving the DC biasing electronics, we envision reaching a bias switching time of less than 50μs, which would result in a kilo hertz imaging frame rate for uFORCES with 8 transmit events. To mitigate the lower SNR on such an ultrafast imaging scheme, coded excitation can be used on the transmit. Also, the intention of ultrafast imaging is for improved and fast volumetric imaging, flow estimation, etc.

Chapter 5

Transparent Bias-Sensitive TOBE Array for Photoacoustic Applications

Although fully-wired 2D ultrasound arrays can provide idealistic ultrasound (US) image quality, commercial piezo-based 2D arrays still remain opaque for through-illumination photoacoustic (PA) applications. Also, fabricating a fully-wired N×N 2D array would become impractical for large arrays. Alternatively, top-orthogonal-to-bottom electrode (TOBE) arrays, also known as row-column arrays (RCA), significantly reduce the number of active channels from N×N channels down to 2×N with some applications in volumetric imaging [36–38]. This makes the fabrication of large-area TOBE arrays possible for a more excellent spatial resolution compared to the state-of-the-art Matrix probes [79]. However, transparent TOBE arrays would be desirable for PA applications facilitating through-illumination light delivery[91, 95]. This could enable improved SNR compared to opaque ultrasound arrays with oblique illumination and also lead to compact US/PA probe design. Electrostrictive lead magnesium niobate (PMN) with low lead titanate (PT) doping can be a good candidate for these PA applications. Ultrasound transducer arrays made of PMN-PT have shown promise for transparent arrays [96]. These electrostrictive materials do not exhibit a piezoelectric effect without an applied bias voltage and have acceptable optical transparency when polished on both sides. TOBE arrays made of these electrostrictive PMN-PT can be used for 3D aperture-coded PA imaging.

5.1 Introduction

Photoacoustic (PA) imaging stands at the confluence of optical contrast and ultrasonic spatial resolution, combining the best of both worlds for unprecedented imaging capabilities. This technique is especially powerful in biomedical applications, offering a non-invasive means of visualizing biological tissues with high contrast and resolution [55]. The crux of PA imaging lies in its ability to capture ultrasound signals generated by the absorption of short-pulse laser beams by biological tissues. PA imaging can be performed by illuminating a large tissue area with a pulsed laser beam and receiving the ultrasound signals on a linear or 2D ultrasound array. Alternatively, a focused laser beam can be rastered on a tissue and receive the signals with a single-element ultrasound transducer, known as optical resolution. However, most photoacoustic imaging techniques use non-optimal light delivery methods where optical and acoustic paths are separated because of opaque ultrasound transducers [97]. Transparent transducers would enable light delivery through the transducer rather than around it. Hence, transparent ultrasound transducers could improve light delivery, leading to high signal-to-noise (SNR) ratios and compact imaging probes, as we have shown in [91]. Transparent ultrasound transducers have been developed and fabricated based on lithium niobate piezoelectric and capacitive micromachined ultrasound transducers (CMUT) in the last few years [51, 92] and used in PAT applications [98, 99]. Nevertheless, they are mostly manufactured in a single-element form or a 1D linear array with a limited aperture size.

In the specific context of PA imaging, the optical properties of the medium play a crucial role. Optical imaging is known for its high contrast but is significantly hampered by scattering in biological tissues. Conversely, ultrasound imaging can provide excellent spatial resolution, mainly using a dense focused probe. PA imaging bridges these two domains, leveraging short-pulse lasers to excite tissues and generate

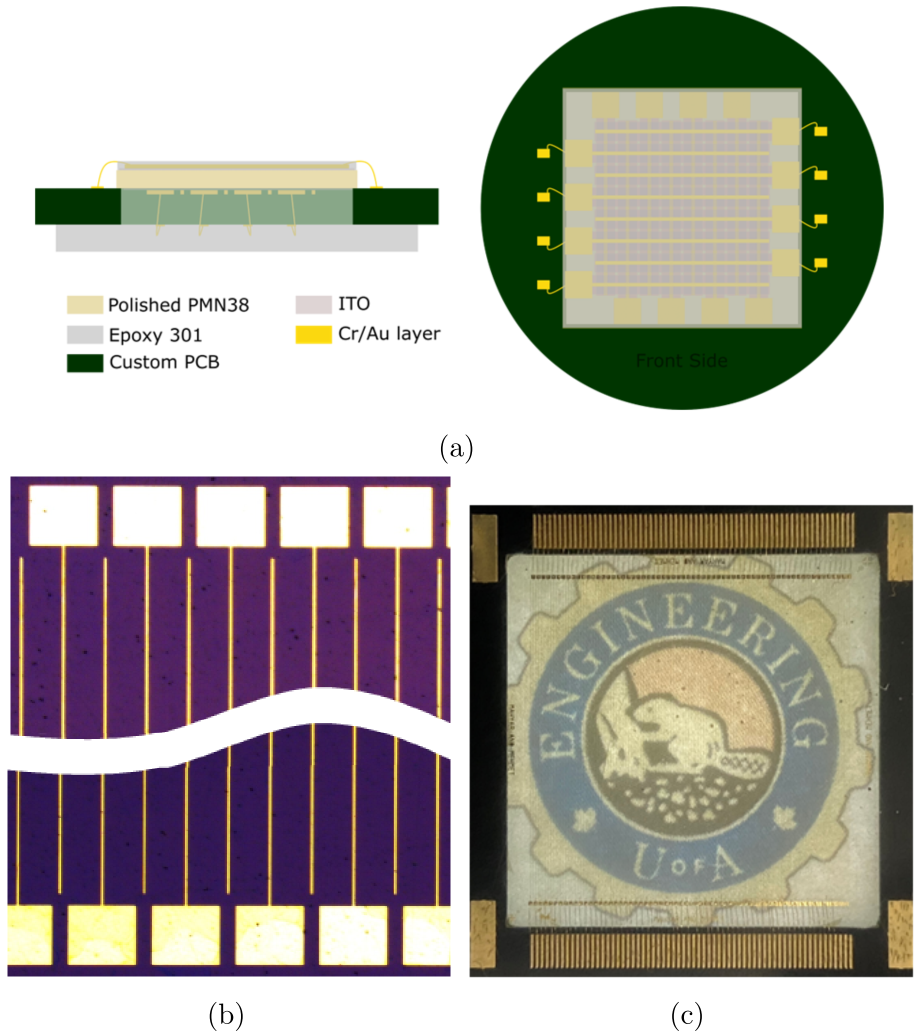

Figure 5.1: The fabricated transparent 128×128 PMN-PT TOBE array; (a) the schematic of the fabricated array on a custom PCB, (b) the Cr/Au stripes on the ITO layer to improve the electrical conductivity; (c) the fabricated transparent array with clear Epoxy backing. The logo of the University of Alberta can be seen through the array.

acoustic waves via thermal expansion.

This chapter briefly describes the fabrication and preliminary PA imaging results of an unprecedented 128×128 transparent TOBE array made of electrostrictive lead magnesium niobate - lead titanate (PMN-PT) [100]. The PA imaging on the array was performed using a Hadamard Matrix coding/decoding as described in [101]. Therefore, 128 laser shots are needed to decode the aperture and read the ultrasound data from each individual element of the array to form a 3D PA image.

5.2 Methods and Procedure

The fabrication of the transparent TOBE array is a meticulous process very similar to the fabrication of the opaque TOBE arrays we have developed, except for some differences in the steps. The fabrication of the transparent TOBE array starts with the mounting of bulk PMN-PT material on a carrier wafer. This is followed by lapping and fine polishing to achieve optical transparency. Indium tin oxide (ITO) is then sputtered and patterned to form the top electrodes, with thin Cr/Au strips enhancing electrical conductivity while maintaining transparency. The array is then flipped, and similar processes are applied to the backside to complete the TOBE array structure. Finally, wire bonding connects the array to custom biasing electronics and a programmable ultrasound platform. As mentioned in previous chapters and shown through KLM modeling, an ultrasound transducer with 1-3 composite fashion is desirable for obtaining the best acoustical matching and improved electromechanical performance. However, the fabrication of a transparent TOBE array required patterning the electrodes via lithography. This step requires soft-baking the photoresist, which results in thermal expansion and cracking in 1-3 composite material. So for the sake of simplicity of the fabrication process, the transparent TOBE array is fabricated with bulk PMN38.

Fig. 5.1 illustrates the schematic and the actual fabricated transparent 128×128 TOBE array with a pitch size of 150μm. Unlike the opaque version of the TOBE

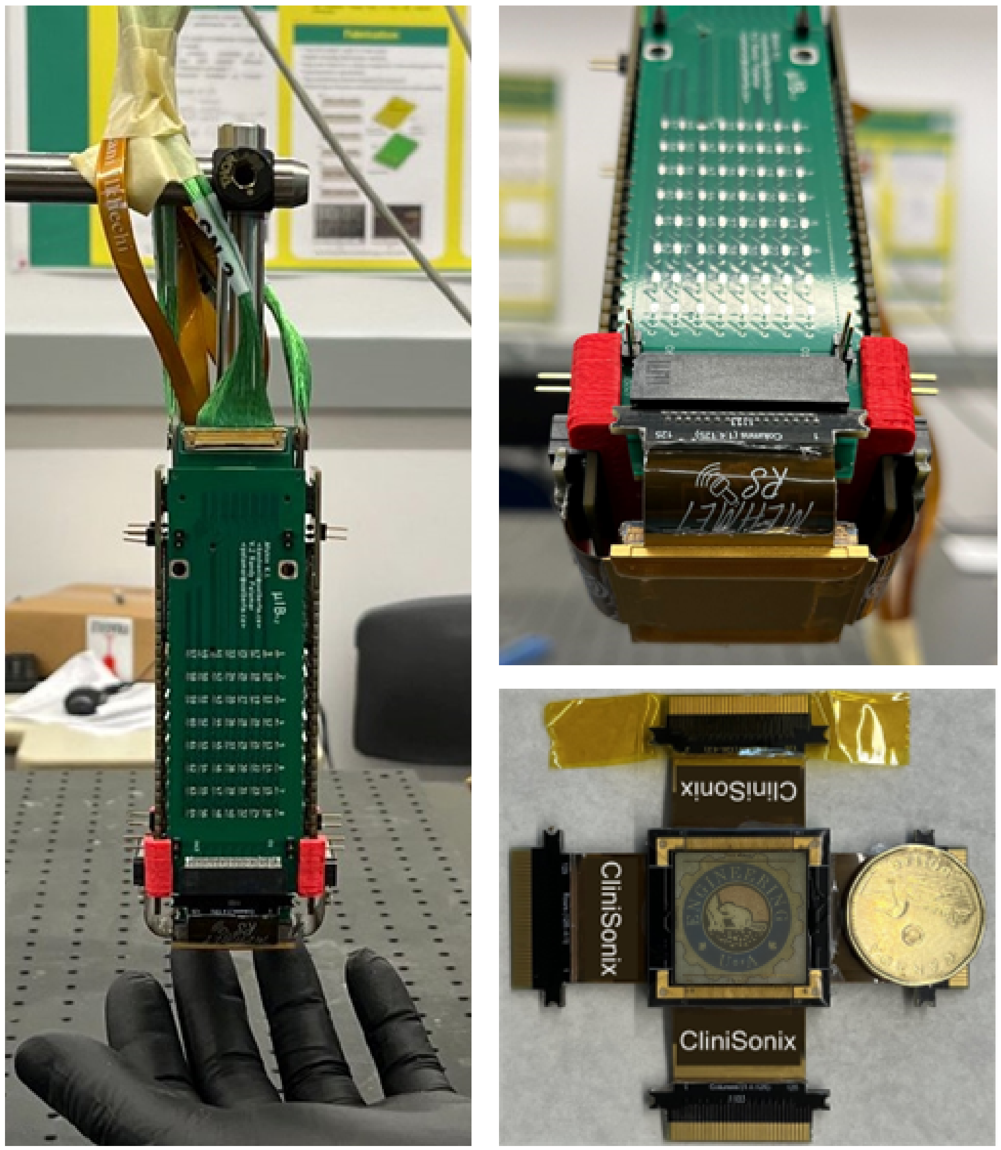

Figure 5.2: The fabricated transparent 128×128 PMN-PT TOBE array in the handheld form of the factor

array that was made of 1-3 composite (electrostrictive PMN-PT and Epoxy301), the transparent version was made with bulk electrostrictive PMN-PT material (commercially called PMN38, TRS Technology). The reason for that was the optical diffraction that we observed when the laser beam was passing through the 1-3 composite material. Also, patterning the Cr/Au strips requires a lithography step, and soft photoresist baking is crucial. So, the difference between the thermal expansion coefficients of PMN38 and epoxy was causing some problems, such as cracking or making the surface uneven. So, we decided to fabricate the transparent TOBE array only with bulk PMN38 material. However, further development in the fabrication process, where elimination of any heating is possible, can mitigate the fabrication of a TOBE transparent array out of 1-3 composite with the benefit of better electromechanical coefficient of the array and improved mechanical and electrical cross-talk between adjacent elements. However, it was not the main objective of this thesis, and we emphasized mainly on the fabrication of the opaque TOBE array, which has broader applications in the biomedical field.

5.3 Results and Discussion

The fabricated 128×128 transparent TOBE array demonstrated a notable 65% optical transparency at 532 nm wavelength with a center frequency of 13.6 MHz. The fabricated transparent TOBE array was connected to our custom handheld interface board containing the bias-tee circuitry, as shown in Fig 5.2. The fabricated TOBE array can be used for 2D/3D aperture-coded ultrasound and photoacoustic (PA) imaging.

The PA imaging is done by applying different bias patterns from the Hadamard matrix on the rows and collecting the data from columns for each laser shot. As shown in Fig. 5.3, four laser shots are needed to read out the data from all the elements of the TOBE grid for a 4×4 TOBE array. Since using a Hadamard-encoded aperture for this specific method gives the raw data for each element of the TOBE grid in 2 dimensions, then a 3D photoacoustic image can be obtained by only four laser shots.

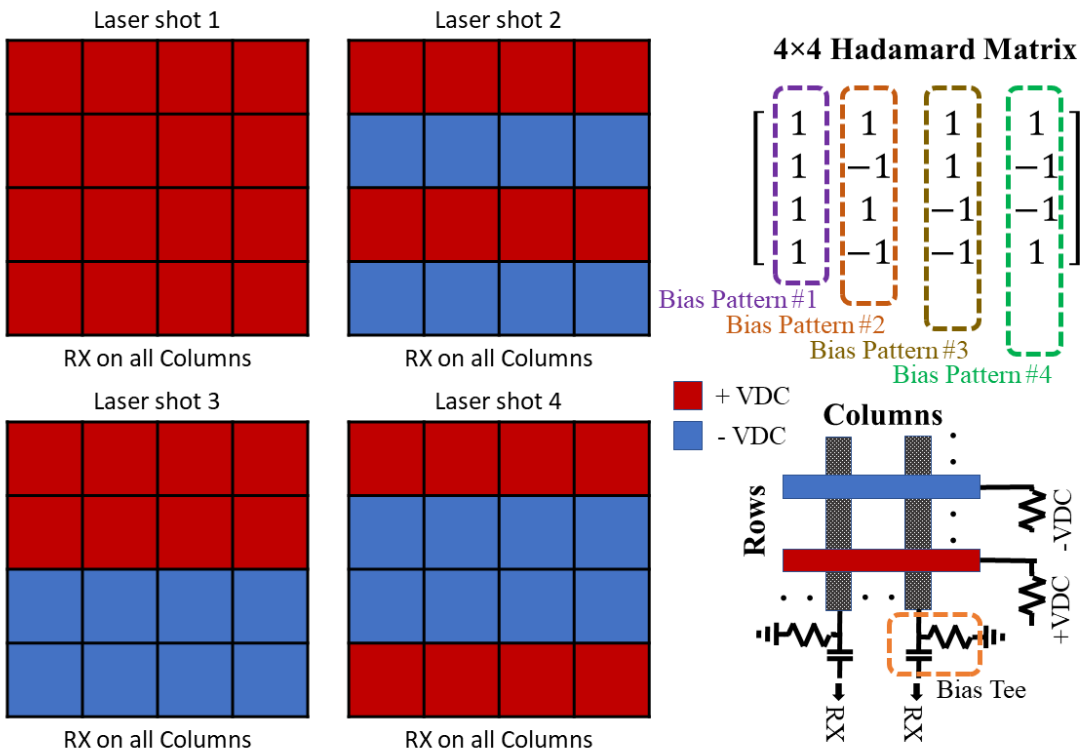

Figure 5.3: The Hadamard aperture encoding for a 4×4 TOBE array for photoacoustic imaging.

Also, the Hadamard encoding/decoding of the aperture improves the SNR compared to the identity encoding, as shown in [88].

Preliminary ultrasound and photoacoustic imaging experiments on 25μm crossed gold wires yield clear images using Hadamard bias-encoding, where for the ultrasound imaging, we performed FORCES scheme [1] and for the photoacoustic scheme what described in Fig. 5.3 with 128 laser shots. For the fabricated 128×128 TOBE arays, 128 transmit events or laser shots are needed to form a 2D ultrasound or 3D photoacoustic imaging, respectively.

Fig. 5.4 illustrates the ultrasound and photoacoustic images of the crossed 25μm gold wires. Transparent epoxy as the backing layer provides good optical transparency, while the acoustic impedance is less than ideal, which may lead to poor axial resolution for some applications. However, this is less important for C-scan projection imaging (Fig. 5.4(d)). In contrast, further improvements are possible by

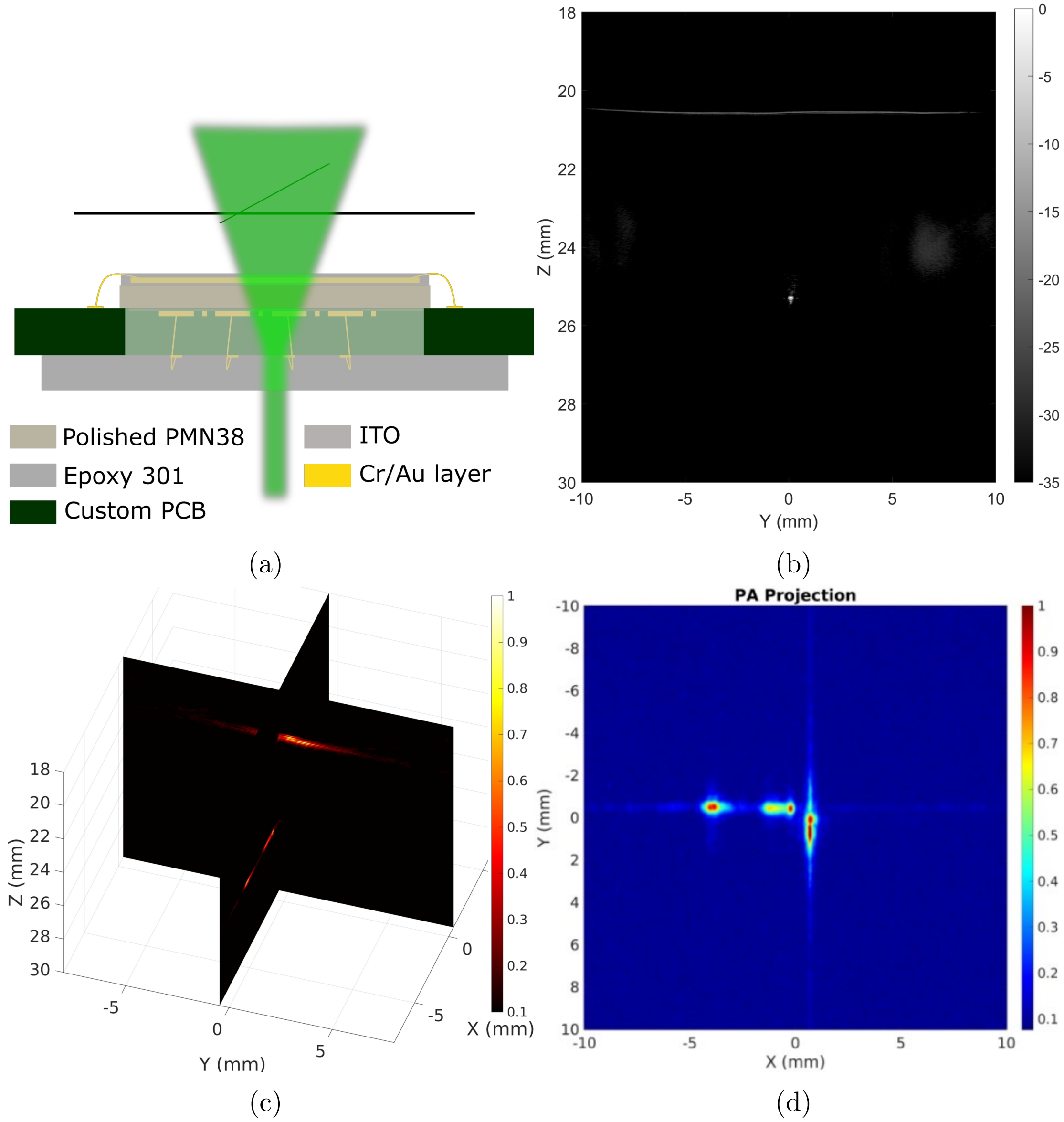

Figure 5.4: The ultrasound/photoacoustic images of 25μm crossed gold wires; (a) the cross-view of the transparent TOBE arrays, (b) a 2D ultrasound image of the crossed wires using FORCES scheme, (c) cross-plane PA image, (d) the maximum PA projection in XY plane (C-scan).

using a bulk glass delay line as a backing layer. However, it was not pursued in this thesis as the main objective was on the development of the opaque TOBE arrays.

5.4 Conclusions

In conclusion, the transparent TOBE array represents a significant advancement over traditional opaque ultrasound arrays, particularly in the field of biomedical imaging. In applications such as blood oxygenation measurement, vessel imaging, and the use of optical contrast agents, the array's ability to deliver light directly through the transducer enables more efficient and precise imaging. This direct illumination approach, combined with the high spatial resolution afforded by the dense focused ultrasound probe, makes the TOBE array a powerful tool for a wide range of PA imaging applications. Also, the through-illumination approach shortens the optical path that the laser beam needs to travel inside the tissue, hence more energy is delivered to the desired imaging area, improving the SNR.

Our prototype transparent TOBE array demonstrated good transparency in the visible light range, reaching as high as 65% around 532 nm. However, a non-ideal but transparent epoxy as the backing layer resulted in a poor axial resolution for some applications, which would be less critical for PAT C-scan projection imaging or PAM with a focused laser beam rastering on the transducer. Further development of the transparent TOBE array should include considering a glass delay line as a backing material, which would improve the axial resolution by providing ideal acoustical matching. Also, making a transparent TOBE array in a 1-3 composite form should be considered for an ideal array to obtain the maximum electromechanical coefficient, higher sensitivity, and improved electrical/mechanical cross-talk. However, the main objective of this chapter was to investigate the feasibility of making a transparent/-translucent TOBE array out of electrostrictive PMN38, where we previously showed a fabricated transparent single-element form factor of this material.

Chapter 6

A Handheld TOBE Array vs. Commercial Ultrasound Probes

As mentioned before, bias-sensitive Top-Orthogonal-to-Bottom-Electrode (TOBE) arrays made of electrostrictive materials have shown great potential in reducing the electrical channel counts and system complexity compared to fully-connected 2D arrays and state-of-the-art Matrix probes. The preliminary results from a large area bias-sensitive 128×128 TOBE array have been reported in [79]. However, those results were from a testbench, not a handheld probe, and experimental comparisons with commercial Matrix probes were not yet performed. This chapter is the final goal of this thesis by aiming to fabricate a handheld form of the TOBE arrays, making it easier to achieve more realistic comparisons with the commercially available linear arrays and state-of-the-art Matrix probes.

6.1 Introduction

The field of ultrasound imaging is growing, with demands for higher resolution and deeper penetration pushing the boundaries of traditional technology. Linear and state-of-the-art ultrasound Matrix probes have served as the backbone of ultrasound diagnostics, while they have their own limitations. Linear probes, with their 1D smaller apertures, are limited in the depth and resolution of the images they can produce. They also use an acoustic lens for elevational focusing, which is only optimum for some imaging depths. On the other hand, the advanced and complex 2D Matrix probes with ASIC micro beamformers implement wide-beam walking aperture (WA) imaging schemes (or similar imaging schemes) as investigated in [79]. The Matrix probes can adjustably focus at specific depths during the transmit phase, which can still be restrictive and less dynamic regarding focusing capabilities with smaller aperture sizes. Although the Matrix probes successfully reduced the cabling complexity, they are still challenging to fabricate, especially for larger arrays.

These conventional probes, while helpful, are constrained by the imaging schemes they employ. For instance, Matrix probes, despite their 2D array design, are bound by the paraxial approximation, which limits their focusing ability, thus leading to potential reconstruction artifacts. Furthermore, the WA imaging schemes implemented on the linear and Matrix probes focus on a single depth at a time, which is suboptimal for comprehensive imaging, where a broader, more uniform focus across multiple depths is advantageous. Such a uniform focusing across the imaging plane is possible, usually with a synthetic aperture (SA) imaging scheme. Implementing SAI on a linear array will compromise the SNR as only one small active element transmitting at a time. Also, it may not be fully implementable on the Matrix probes as they use some approximations and multiplexing, limiting the access to each individual element on their 2D grid.

In contrast, our bias-switchable TOBE array employs our cutting-edge aperture-encoded FORCES and uFORCES imaging schemes. These schemes implemented on the bias-sensitive TOBE arrays offer aperture-encoded full and sparse synthetic aperture imaging capabilities where the entire imaging plane is ideally in focus during both the transmit and receive phases. This is a significant advancement over the WA imaging schemes as it does not limit the focus to a single depth (at least in a 1-way imaging plane), thereby providing clinicians with a more detailed and uniform image across various depths. Also, unlike 1D linear probes with a fixed acoustic lens and unlike Matrix probes with limited f-number and implemented ap-

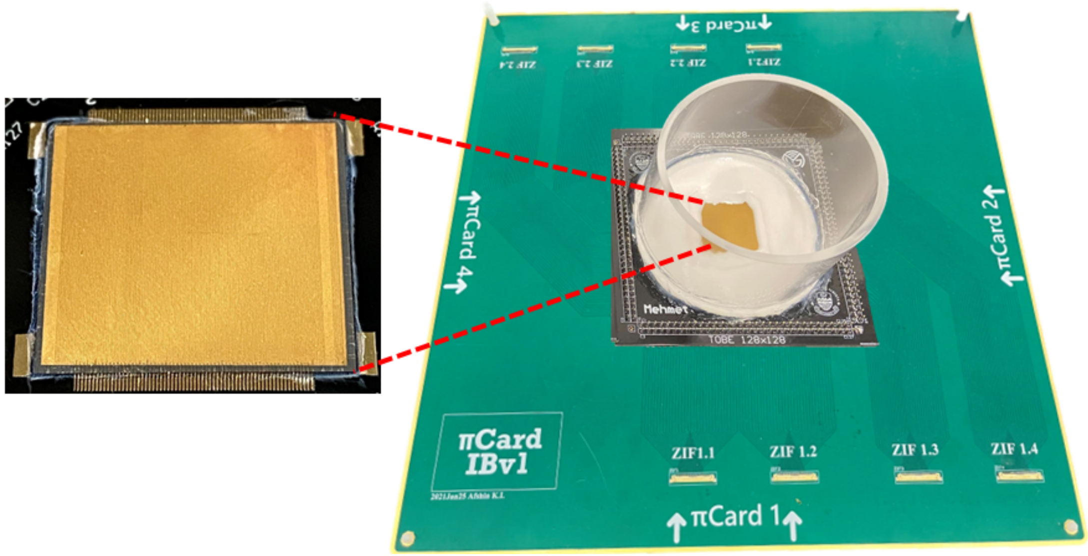

(a)

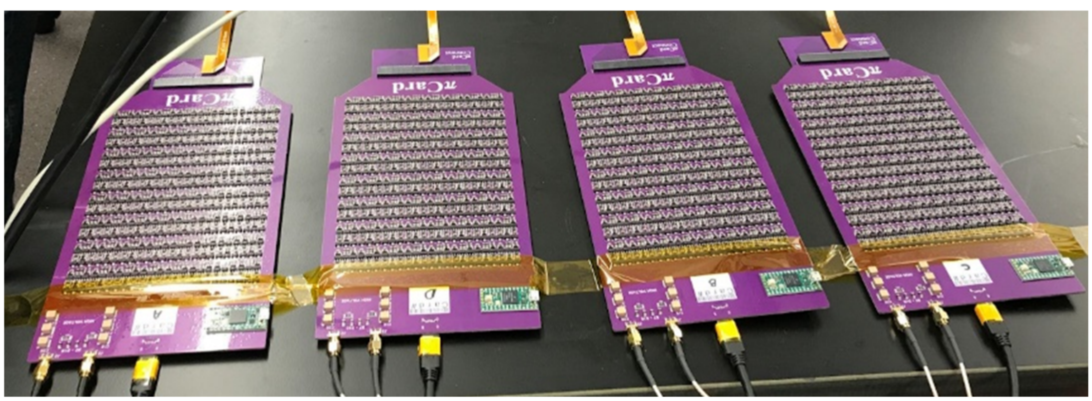

(b)

Figure 6.1: The old benchtop setup for the TOBE arrays; (a) the bulky interface PCB board with bias-tee circuitry and a connected TOBE array, (b) the bias-switching electronics for a total of 256 channels. each biasing PCB handles 64 channels.

proximations, TOBE arrays offer 1-way adjustable/steerable transmit beams at the elevational plane. So, bias-sensitive TOBE arrays with implemented FORCES or uFORCES imaging schemes, on the transmit can provide 2-way focusing (azimuthal focusing everywhere because of the SA imaging scheme, plus electronically focusing the beam in the elevational plane). Likewise, they provide only 1-way focusing on the receive in the azimuthal plane because receiving the beam on all the long columns (or rows). Moreover, the bias-sensitive TOBE array's design permits a reduction in channel count without compromising signal quality, unlike traditional multiplexing techniques that can decrease SNR. This design allows for larger apertures without the typical trade-off in imaging speed or cabling complexity, paving the way for a new generation of high-quality, high-speed ultrasound imaging.

The potential of the bias-sensitive TOBE array and its associated imaging schemes is shown in previous chapters, mostly with simulation results. However, performing a realistic comparison with commercial linear and Matrix probes due to the benchtop setup and design was challenging so far. In this chapter, we propose the handheld form of the factor for our bias-sensitive TOBE arrays and compare the imaging results performed on resolution and cyst phantoms.

6.2 Methods and Procedure

Our previous TOBE arrays were all mounted on a bulky interface PCB with all the bias-tee circuitry and connection to an ultrasound platform (Verasonics). Also, a water tank was glued on the PCB of each TOBE array to facilitate the immersion testing, as shown in Fig. 6.1 (a). The DC biasing electronics for a total number of 256 channels [102] is shown in Fig. 6.1 (b).

To perform more realistic imagings with the TOBE arrays and make them comparable with the commercial ultrasound machines, we shrank down the design to the hand-held form. So, the bias-tee circuitries are implemented on a small handheld interface where the TOBE array fabricated on a custom Rigid-Flex PCB connects

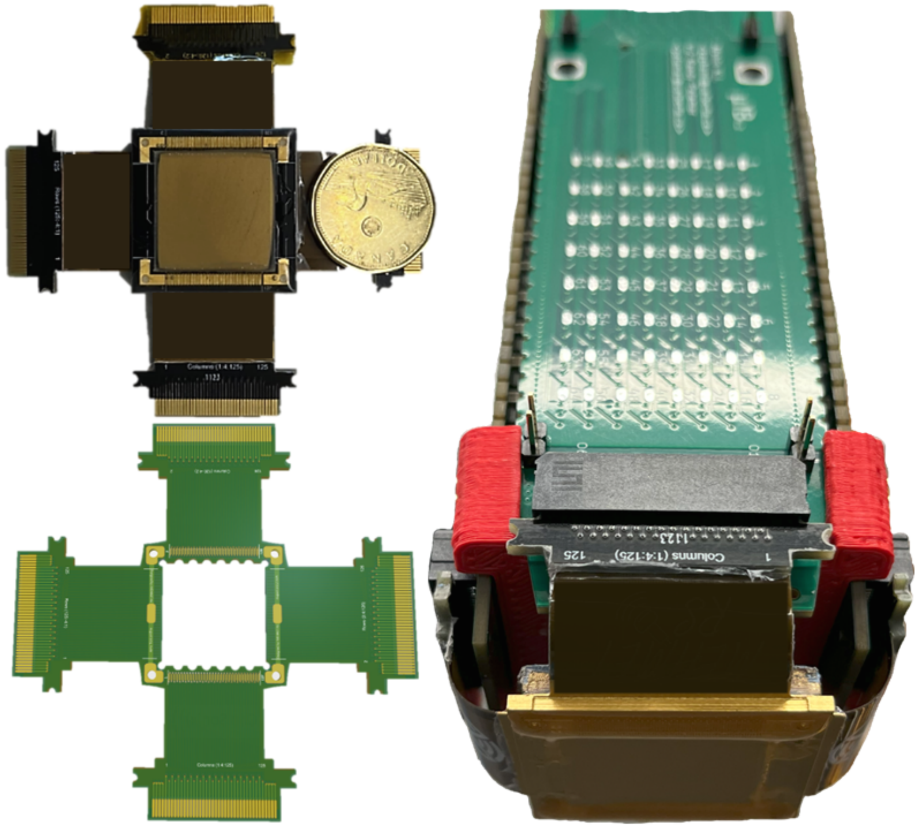

(a)

(b)

Figure 6.2: The handheld form of the factor for TOBE array; (a) the handheld interface board with a fabricated TOBE array on a custom rigid-flex, (b) the bias-switching electronics placed in a 3D-printed box.

to that as shown in Fig 6.2 (a). To further improve the overall SNR of the system and to eliminate the risk of electrocution for the operator, we placed the high-voltage biasing electronics inside a 3D-printed box with extra shielding as shown in 6.2 (b).

As for the imaging, the FORCES imaging scheme was implemented on the fabricated TOBE arrays to obtain the full synthetic imaging dataset, as described in the previous chapters and briefly shown in 6.3 for a simplified 4×4 TOBE array. In summary, for the data acquisition, three main steps are needed: 1) biasing the columns with Hadamard patterns, 2) for each bias pattern, transmitting a focused beam along rows, and 3) receiving data along columns. Similarly, for the reconstruction: 1) decoding data using an inverted Hadamard matrix (the result is a synthetic aperture dataset with improved SNR), 2) coherently adding low-resolution images to obtain a high-resolution image. The order of rows and columns can be electronically swapped to obtain cross-plane or 3D images.

With the current electronics and the biasing circuitries, the FOCRES imaging scheme on a 128×128 TOBE array, with 128 transmit events, can provide up to 30 frames per second (FPS). Likewise, uFORCES with as low as 8 transmit events can go up to 480 FPS.

6.3 Results and Discussion

The fabrication of the TOBE arrays in a handheld form was done with a unique technique on a custom rigid-flex PCB with a total of 4 edge connectors, 1 on each side of the array handling 64 channels. A few different TOBE arrays were fabricated with the size of ∼19×19 m^2 and ∼32×32 m^2. Only a layer of Parylene C as a matching layer and electrical shielding was used on all the fabricated arrays for simplicity.

6.3.1 Array Characterization and Insertion Loss

Before doing any ultrasound imaging, the pulse-echo (PE) measurement was done on the fabricated TOBE arrays to estimate their operational center frequency. For

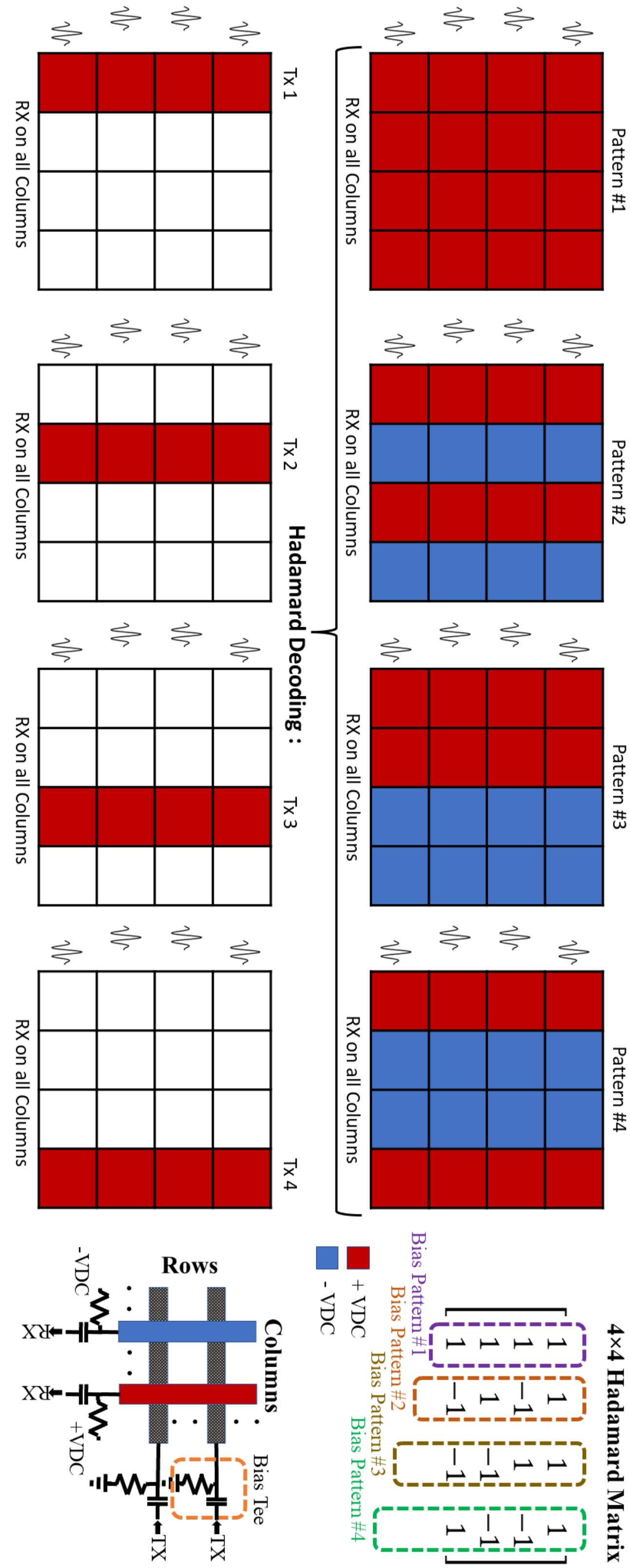

Figure 6.3: FORCES imaging scheme using a 4×4 Hadamard matrix.

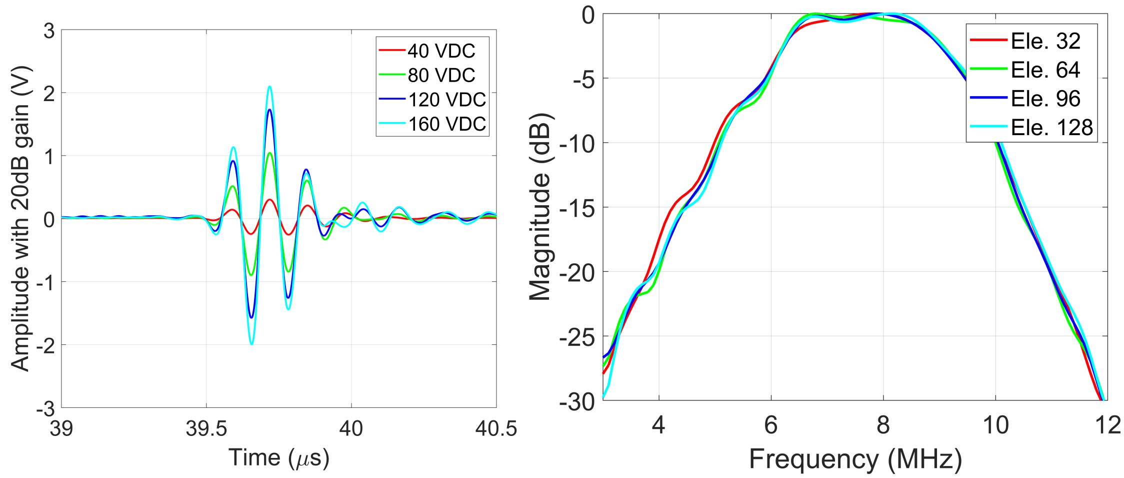

(a) (b)

Figure 6.4: The pulse-echo measurement of a 128×128 TOBE array; (a) the PE response for an individual element on the array for different DC biasing voltages, (b) the PE spectrum for a few individual elements on the array at 120VDC, showing the PE response uniformity across the array.

this test, a single channel of the array was used to transmit ultrasound, which was reflected from a thick steel plate to be received by the same channel. To this end, a pulser/receiver with an excitation negative spike voltage and a receive gain of 20 dB at a frequency range of 5 to 20 MHz was used (PANAMETRICS-NDT, 5073PR). Fig. 6.4(a), (b) shows the PE response of the array for an individual element on the array for different DC bias voltages, and the PE spectrum uniformity for a few elements all at 120 VDC, respectively. For this particular TOBE array with an active aperture of ∼19×19 m^2, we measured a center frequency of ∼7.5 MHz with a bandwidth of ∼60% at 120 VDC.

Another useful characterization method of the fabricated TOBE arrays was insertion loss. The measurement of ultrasound insertion loss (IL) is an important factor in evaluating the performance of ultrasound imaging arrays. This parameter determines the amount of acoustic energy lost as ultrasound waves travel through a medium and back, which is critical in assessing the efficiency and effectiveness of the ultrasound array in producing clear images. High insertion loss can cause poor image quality due to insufficient signal strength reaching the target tissue or being reflected back to the detectors.

We performed the IL measurements on two fabricated TOBE arrays, with center frequencies of 2.5 MHz (64×64, ∼19×19 mm^2) and 7 MHz (128×128, ∼19×19 mm^2) at different distances from a steel plate inside the water tank. We ignored the effect of attenuation in water. For a fair comparison, we did the same measurements on commercially available single-element transducers with a center frequency of 2.25 MHz (Olyumpus, V323-SM) and 10 MHz (Olympus, V312-SM). These transducers are Videoscan transducers with heavily damped broadband performance suitable for applications with good axial resolution and improved SNR. Fig. 6.5 shows the IL measurements for a few arrays and single-element transducers. The results for the fabricated TOBE arrays are comparable with the reported -43 dB insertion loss for a 20 MHz array made of single-crystal PMN-PT [103]. Only a single column is used for the IL measurements on the fabricated TOBE arrays. So as we go far from the still plate, less power perpendicularly hits the target and reflects back to the transducer. This can be seen clearly in the shown image as the IL drastically drops by distance for a long narrower transducer.

6.3.2 Resolution and Cyst Phantom Imaging

A commercial phantom containing the resolution and cyst sections was used to perform the imaging. A couple of millimeters thick layer of water (instead of ultrasound gel) was used to ensure a perfect coupling between the arrays and the phantom. The phantom had a speed of sound around 1460 mm/s. So far, we have not been able to perform such imaging on the phantoms because of the benchtop setup. However, the fabricated handheld form of the array facilitated this imaging, as shown in Fig. 6.6.

To obtain the optimum image quality on the fabricated TOBE arrays, we set the DC biasing voltages around 4 to 5 kV/cm, where the maximum piezoelectric coefficient is reported for the PMN38 material. This is roughly equivalent to 90, 120,

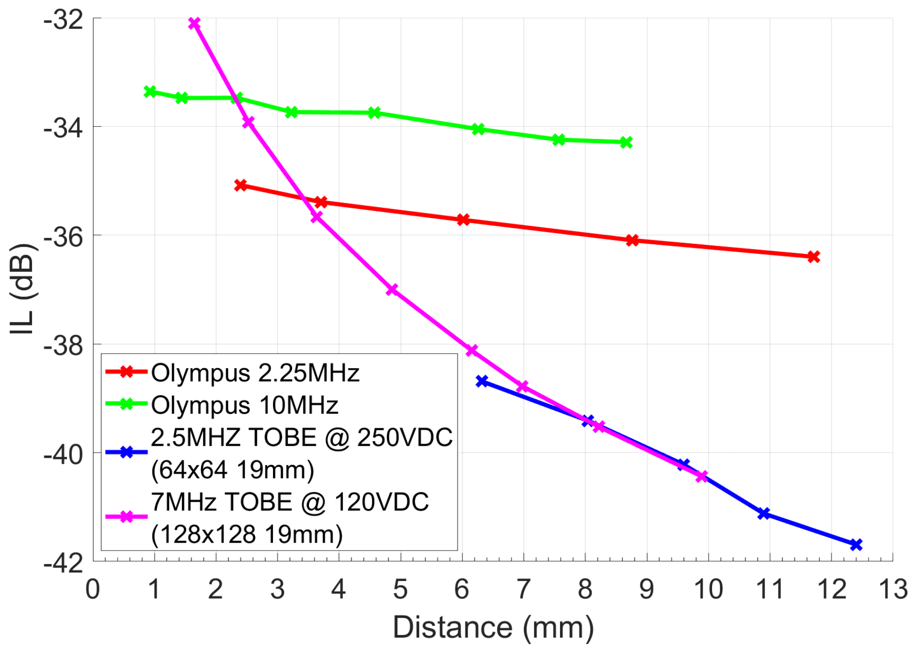

Figure 6.5: The measured insertion loss (IL) for two fabricated TOBE arrays and comparing the results with commercial single-element transducers.

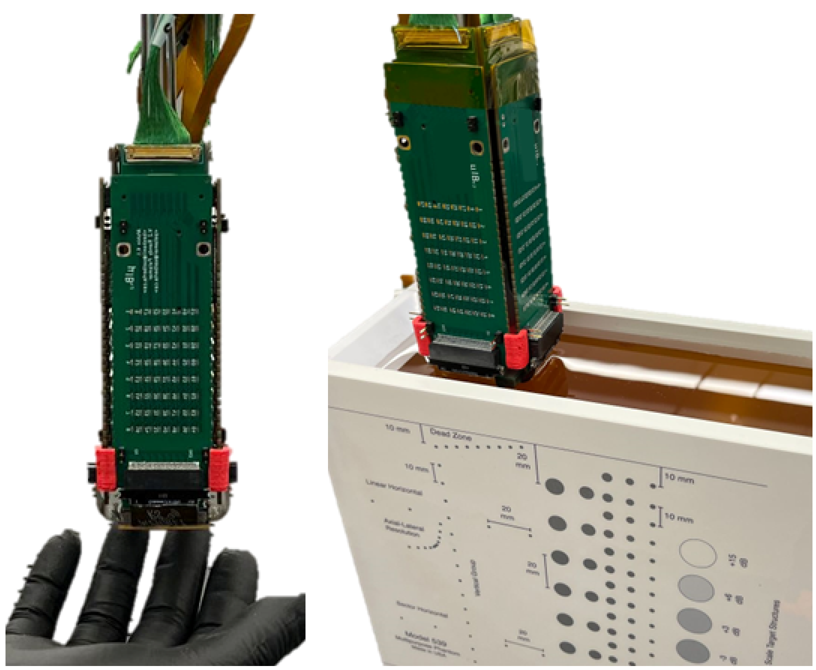

Figure 6.6: A commercial resolution-cyst phantom and the fabricated handheld TOBE array for imaging.

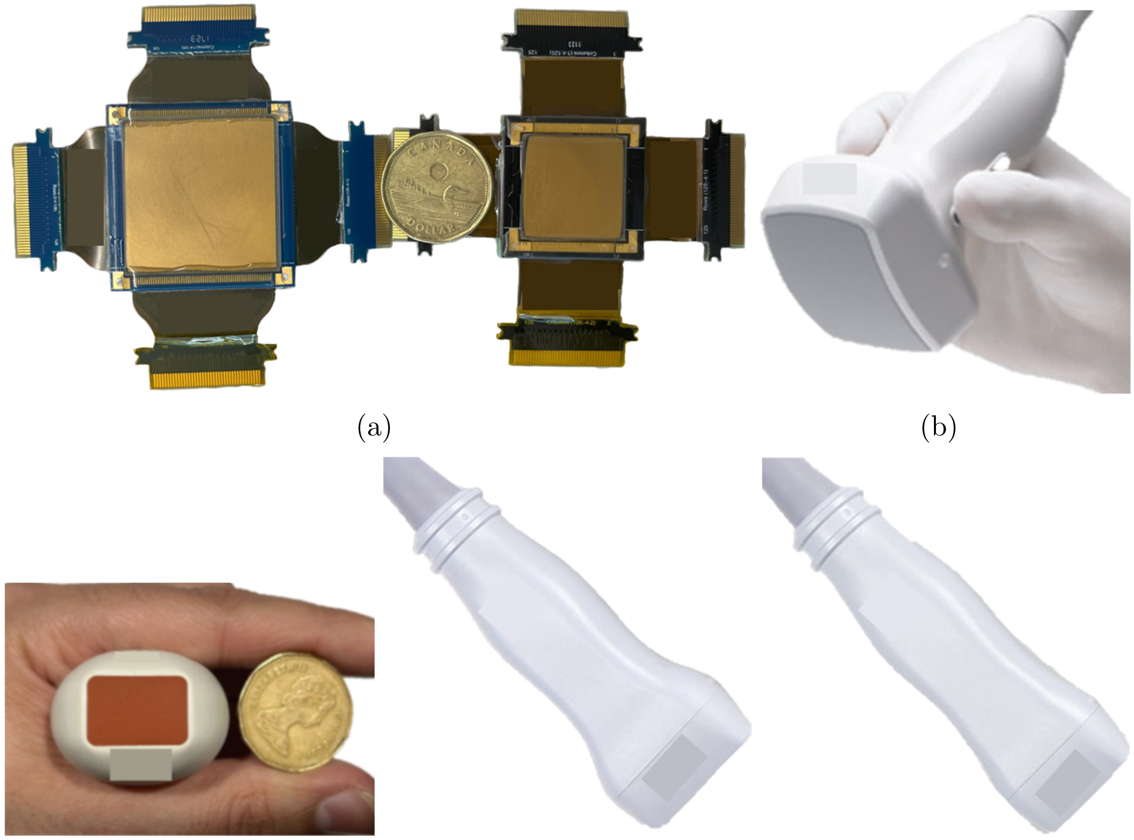

(a) (b)

(c) (d) (e)

Figure 6.7: The commercial and fabricated arrays used for the comparison: (a) the fabricated 128×128 TOBE arrays with two different active aperture sizes, ∼19×19 m^2 and ∼32×32 m^2, (b) a commercial volume probe: 13-5 MHz, (c) a commercial Matrix probe: 7-2 MHz, (d) a commercial linear probe: 10-22 MHz, and (e) a commercial linear probe: 15-30 MHz.

and 140 DC voltages for the fabricated 10 MHz, 7.5 MHz, and 6 MHz TOBE arrays, respectively, regardless of their physical dimensions.

First, we performed the imaging on the resolution/cyst phantom with two commercial ultrasound machines and different probes. Experienced sonographers performed the imaging on commercial ultrasound machines to ensure the best quality images were collected from the phantom. Then we performed the FORCES imaging scheme on the Verasonics platform with our different fabricated handheld TOBE arrays and compared the results. Fig. 6.7 illustrates all the probes used for this comparison.

The preliminary results of the fabricated TOBE Arrays are compared with the commercial Matrix and linear probes, as shown in Fig. 6.8. FORCES imaging scheme was implemented on the fabricated TOBE array with an elevational focus at 40 mm. Fig. 6.8 (a) and (d) illustrate the results for the TOBE arrays with the same physical active aperture size ($\sim$19$\times$19 m^2), but different frequencies of 7 and 10 MHz, respectively, with a dynamic range of 50dB. Figures 6.8 (b),(c), (e), and (f) are all shown in 50 dB, respectively. The maximum depth of the imaging for the high-frequency linear arrays was 38 and 30 mm, as shown in (e) and (f), respectively.

As expected from the simulations we conducted in the previous chapters, the aperture-coded full synthetic aperture implemented on the bias-sensitive TOBE array offers better in-plane resolution than the commercial probes where the walking aperture is the primary imaging scheme. The lateral resolution obtained from the TOBE arrays is superior compared to other probes. However, the axial resolution is mostly frequency/bandwidth dependent, as for a higher frequency, the axial resolution increases. Calculating the spatial resolutions for the images obtained by commercial machines is challenging, as we could not export the image data in raw format. However, we calculated -6 dB resolution for our TOBE arrays for the 5th point in the middle. We calculated the axial resolution of $\sim$350μm and $\sim$310μm, and the lateral resolution of $\sim$400μm and $\sim$390μm for the 7 MHz and 10 MHz TOBE arrays, respectively. As it is obvious in Fig. 6.8, the fabricated TOBE arrays outperform the commercial probes in lateral resolution and image quality.

The same probes were used again for another imaging comparison on the cyst phantom with the same imaging settings. Fig. 6.9 (a) and (d) illustrate the images obtained by the fabricated TOBE arrays with the same physical active aperture size ($\sim$19$\times$19 m^2) but different frequencies of 7 and 10 MHz, respectively, with a dynamic range of 50dB. Figures 6.9 (b),(c), (e), and (f) are all shown in the 50 dB dynamic range. The maximum depth of the imaging for the high-frequency linear arrays was 38 and 30 mm, as shown in (e) and (f), respectively. Table 6.1 summarizes the calculated

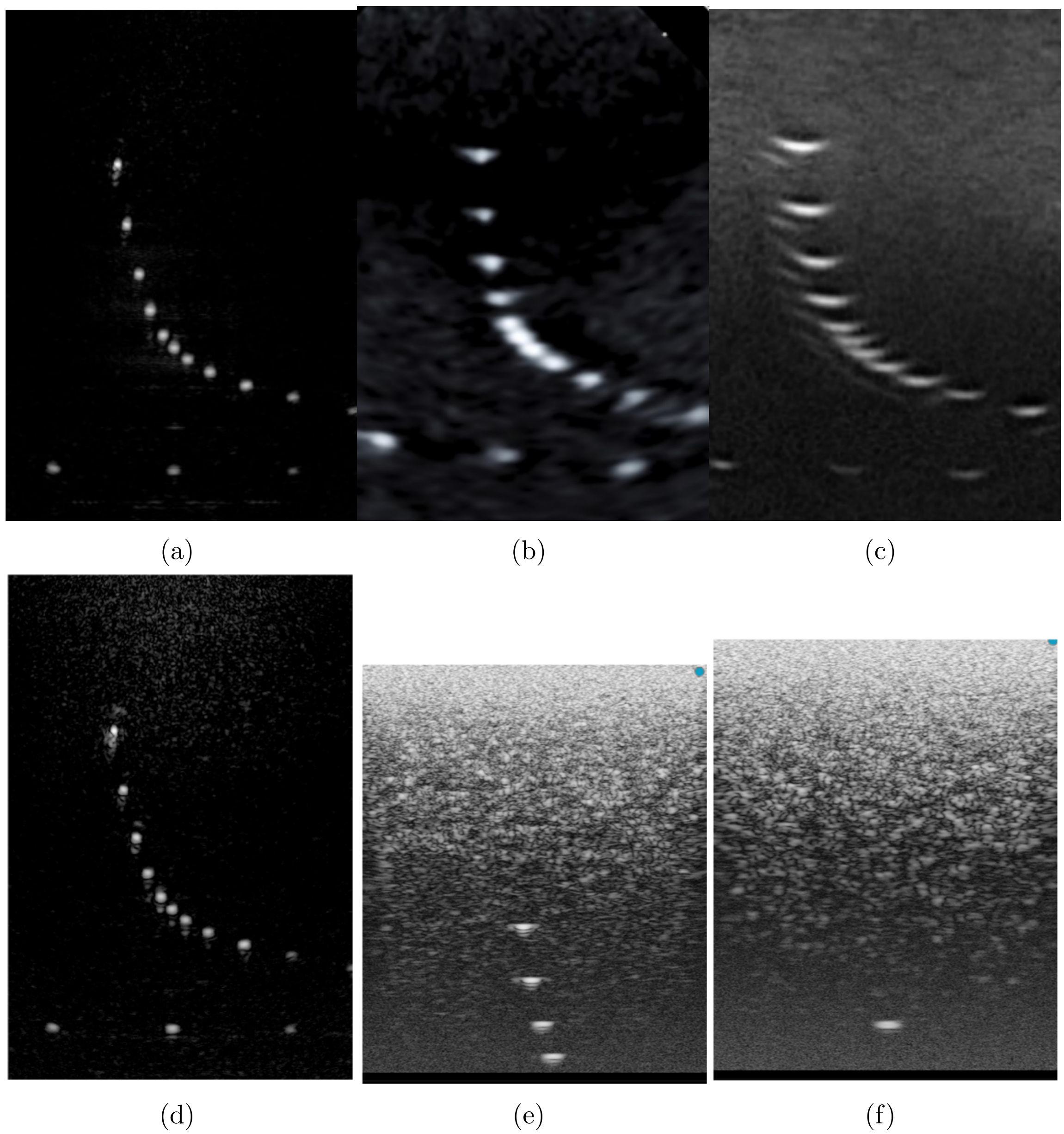

Figure 6.8: The comparison of resolution phantom imaging: (a) the fabricated 128×128 TOBE arrays at 7 MHz (∼19×19 m^2), (b) commercial Matrix probe: 7-2 MHz, (c) commercial volume probe: 13-5 MHz, (d) the fabricated 128×128 TOBE arrays at 10 MHz (∼19×19 m^2), (e) commercial linear probe: 10-22 MHz, and (f) commercial linear probe: 15-30 MHz.

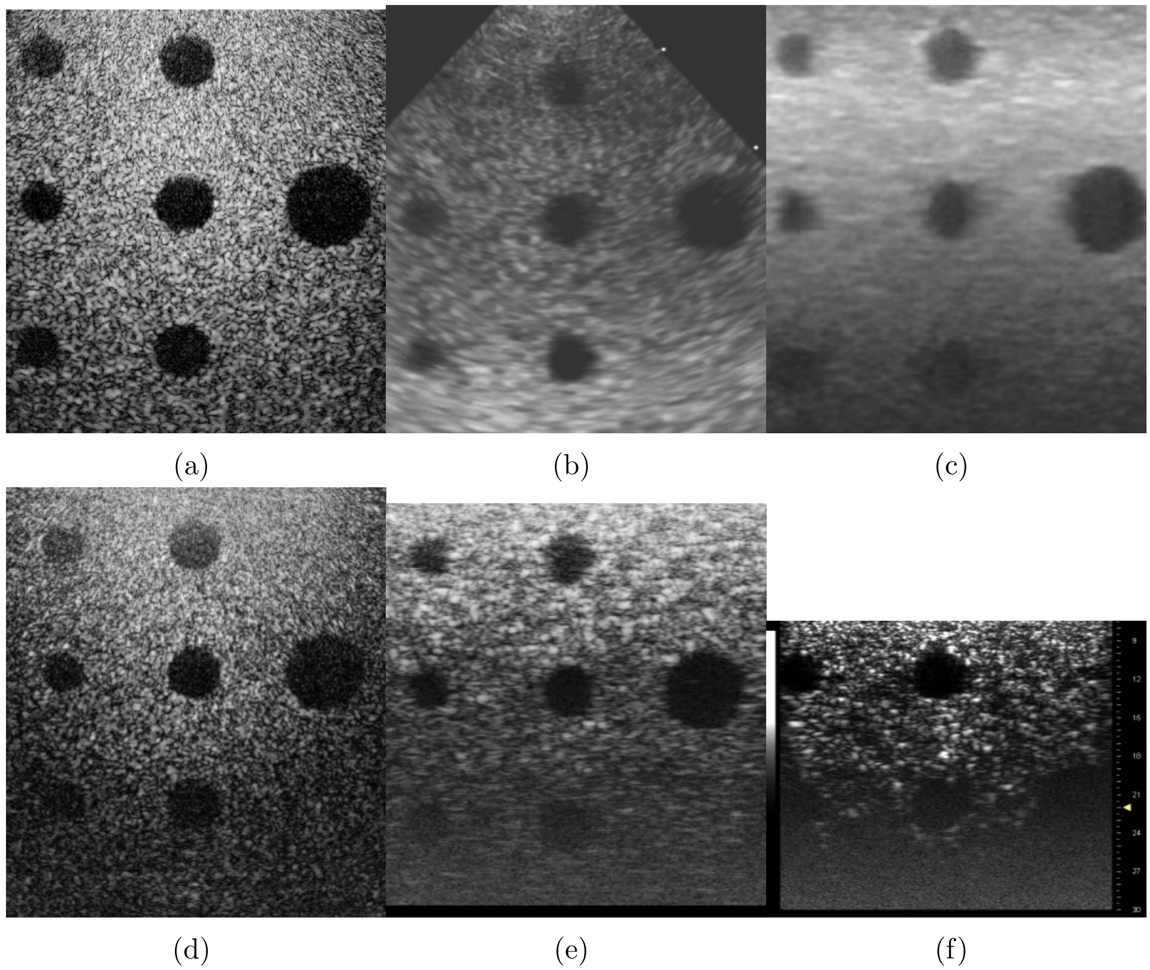

Figure 6.9: The comparison of cyst phantom imaging: (a) the fabricated 128×128 TOBE arrays at 7 MHz (∼19×19 m^2), (b) commercial Matrix probe: 7-2 MHz, (c) commercial volume probe: 13-5 MHz, (d) the fabricated 128×128 TOBE arrays at 10 MHz (∼19×19 m^2), (e) commercial linear probe: 10-22 MHz, and (f) commercial linear probe: 15-30 MHz.

signal-to-speckle ratio (SNR) and contrast for the middle cyst at 20 mm depth with the equations provided in Chapter 4.

To the best of our knowledge, frame averaging is one of the main processing steps implemented on commercial ultrasound machines, and the obtained results may have gone through internal processing steps before storing. In contrast, the FORCES imaging results from the fabricated TOBE arrays are reported without post-processing.

We conducted the same imaging scheme (FORCES) on another fabricated TOBE array with an active aperture of ∼32×32 m^2 and a center frequency of ∼6 MHz as

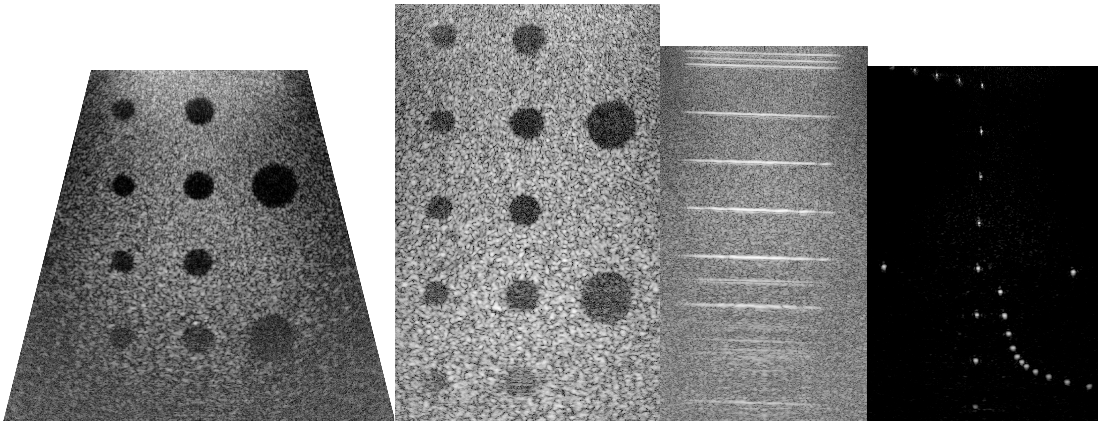

(a) (b) (c) (d)

Figure 6.10: The comparison of cyst and resolution phantom imaging for a bigger TOBE array: (a) the fabricated 128×128 TOBE arrays at 7 MHz (∼19×19 m^2), (b) the fabricated 128×128 TOBE arrays at 6 MHz (∼32×32 m^2), (c) YZ-plane image of resolution phantom for the fabricated 128×128 TOBE arrays at 6 MHz (∼32×32 m^2), (d) XZ-plane image of resolution phantom for the fabricated 128×128 TOBE arrays at 6 MHz (∼32×32 m^2). All are shown in a 50 dB dynamic range with the same imaging scheme (FORCES).

shown in Fig. 6.10. As expected, a bigger TOBE array offers more penetration and improved lateral resolution for the roughly same operating center frequency. The imaging frame rate stays the same, requiring only 128 transmit events for the fabricated TOBE array. Also, unlike commercial linear arrays, the order of the columns and rows can be electronically swapped to obtain crossed-plane imaging, as shown in Fig. 6.10 (c) and (d). In contrast, this is impossible for the linear probe without mechanically rotating it by 90 degrees. As mentioned before, conventional RCAs are restricted to obtaining an image below the shadow of the aperture because of their implemented imaging schemes and lower SNR. However, our TOBE arrays can provide a wider field of view (FOV), as an example demonstrated in Fig. 6.10 (a).

Fig. 6.11 illustrates another set of images from the resolution phantom with calculated spatial resolution and SNR reported in Table 6.2. We used the 5th point form left at a depth of around 70 mm for these calculations.

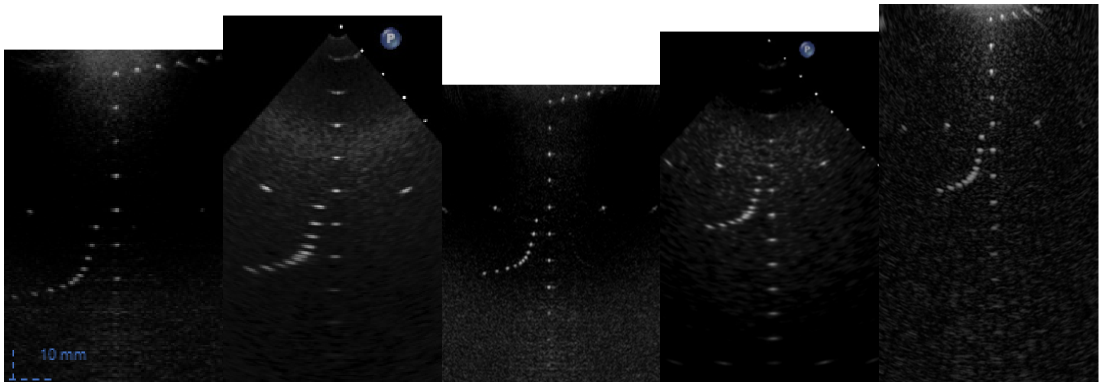

(a) (b) (c) (d) (e)

Figure 6.11: The comparison or resolution phantom imaging for (a) the fabricated 128×128 TOBE arrays at 7 MHz (∼19×19 m^2), (b) commercial Matrix probe: 7-2 MHz, (c) the fabricated 128×128 TOBE arrays at 6 MHz (∼32×32 m^2), (d) commercial Matrix probe: 3-1 MHz, (e) the fabricated 64×64 TOBE arrays at 2.5 MHz (∼19×19 m^2). All are shown in a 50 dB dynamic range with the same imaging scheme (FORCES) on the TOBE arrays. The vertical points are separated by 10 mm.

6.4 Conclusions

In conclusion, we successfully showed the fabrication of a handheld bias-sensitive TOBE array with unprecedented big active aperture sizes. The preliminary results were in good agreement with our initial simulation results, showing the superiority of our fabricated TOBE arrays compared to the commercial ultrasound probes in terms of in-plane resolution and potential for higher imaging speed. The developed ultrasound system still requires better EMI shielding to further improve the SNR and image quality. The preliminary results showed some reverberation inside the backing material that degraded the image quality, especially at some specific depths around 30 mm. Also, some imaging artifacts have been seen on the TOBE arrays that we believe are mostly due to the non-ideal backing and matching layers and unmatched electrical impedance between the array and the imaging platform. Further improvement of the TOBE arrays is possible by using multiple matching layers and using a quarter-wavelength thick array instead of a conventional half-wavelength design. These would result in improved sensitivity, fractional bandwidth, and lower required

Table 6.1: Comparison of Contrast and Contrast-to-speckle Ratio for the Fabricated TOBE and Commercial Arrays

Arrays	Cyst Phantom @ 20 mm	
	Contrast	CSR
TOBE Array: 7 MHz	-0.86	-2.83
TOBE Array: 10 MHz	-0.78	-2
Matrix Probe: 7-2 MHz	-0.46	-3
Volume Probe: 13-5 MHz	-0.48	-3.2
Linear Probe: 10-22 MHz	-0.71	-2.11
Linear Probe: 15-30 MHz	-0.3	-0.94

DC biasing voltages to promote electrical safety. At the time of writing this dissertation, high-frequency Matrix probes were absent, as their fabrication is challenging with embedded microbeamforming electronics. In contrast, our TOBE arrays have no technical limitations for fabricating high-frequency arrays. Also, our TOBE arrays are massively scalable. As future work, the suggested TOBE array can be fabricated in a tiled fashion, as shown in Fig. 6.12, which can be customized for each application with the benefits of bigger aperture size and greater penetration suitable for whole organ imaging user-independently. Also, the wearable variant of the TOBE arrays is a good candidate for bedsite monitoring, where the superiority of the imaging resolution would result in efficient and precise diagnosis.

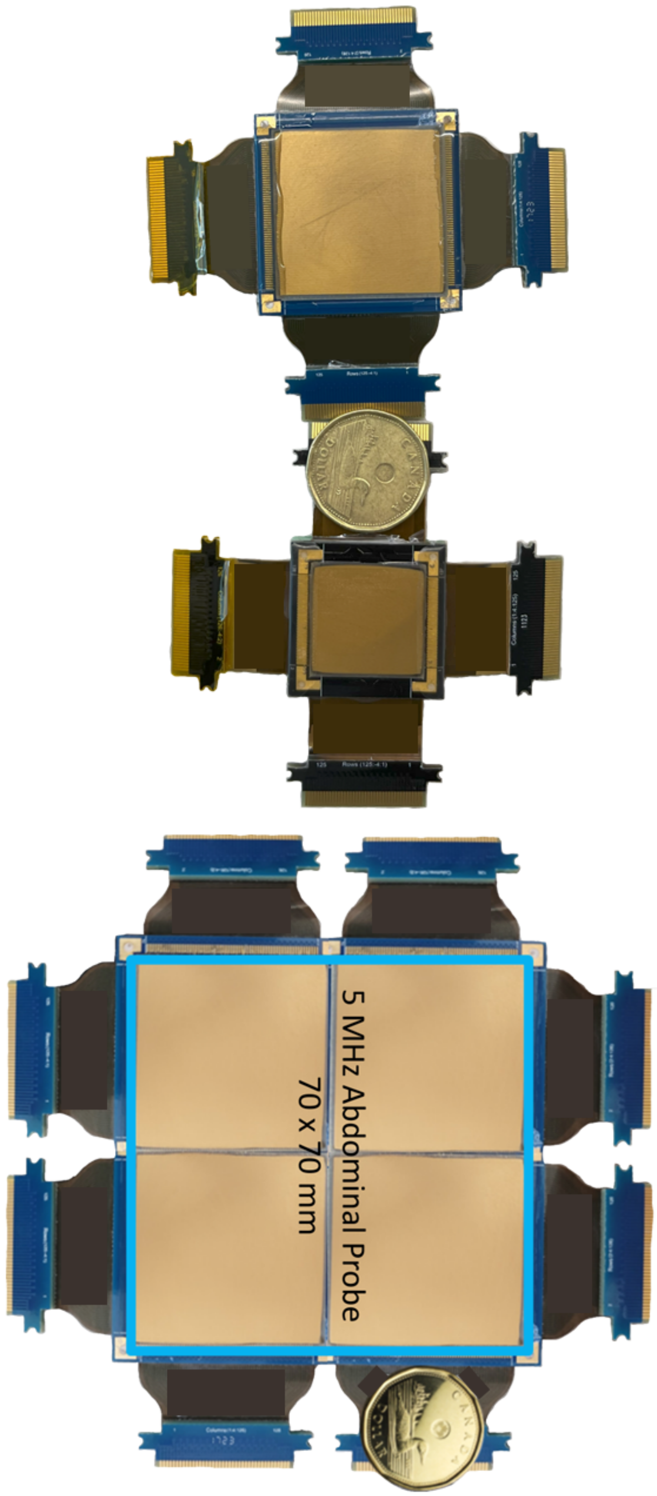

Figure 6.12: The proposed 2×2 tiled TOBE array for making a bigger aperture for abdominal imaging applications.

Table 6.2: Comparison of Spatial Resolutions and SNR for the Fabricated TOBE and Commercial Arrays

Arrays	5th point from left @ ~70 mm depth		
	Axial Res. (μm)	Lateral Res. (μm)	SNR (dB)
TOBE Array: 7 MHz	~350	~400	30.13
Big TOBE Array: 6 MHz	~580	~350	32.8
Matrix Probe: 7-2 MHz	~396	~904	31
Matrix Probe: 3-1 MHz	~473	~786	30.25
TOBE Array: 2.5 MHz	~600	~710	23.76

Chapter 7

Conclusion and Future Work

Some of the challenges that need to be considered are edge artifacts and the electrical safety of the TOBE arrays. Fast bias-voltage switching could result in unsafe AC leakage currents, even when an insulating matching layer is present. To address these two unmet needs, we investigated a TOBE architecture that involves tapered electrodes to implement apodization. Additionally, we introduce a thin grounded conducting layer sandwiched between two matching layers to reduce the coupled leakage currents while further improving the bandwidth. To investigate the proposed advantages of apodization on imaging, we used Field II simulations to implement row-column imaging schemes such as Ultrafast Orthogonal Row-Column Electronic Scanning (uFORCES) with and without apodization present.

Also, we used KLM modeling and circuit models to investigate the benefits of the grounded metal shielding layer as part of the matching layers. The schematic of the proposed transducer is shown in Fig. 7.1. The electrodes are patterned on both sides of the sample such that an apodization is applied by lithographically tapering each electrode. However, this fabrication method with the tapered electrode was not the main objective of this thesis and required further development for precise fabrication. With good progress in making variable DC biasing electronics in our lab, apodization can be dynamically applied to a regular bias-sensitive TOBE array without the need to pattern the electrodes. A microscope with a sample back-light is used to capture

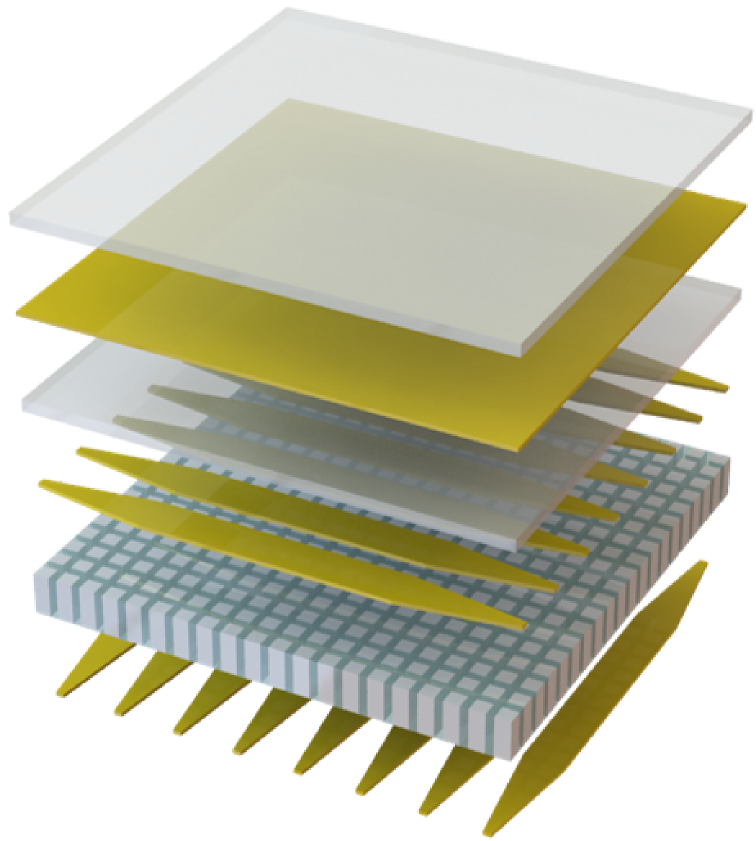

Figure 7.1: Schematic of Shielded TOBE array with tapered electrodes.

the images of the fabricated 128×128 TOBE array at 10 MHz (pitch=150μm) with tapered electrodes as shown in Fig. 7.2.

The performance of the transducer and the leakage currents were investigated with and without a grounding metal layer as part of the matching layer stack. The effect of the coupling current was simulated on the array with a switching DC bias of +/-200 volts at a repetition rate of 10 kHz. The maximum simulated AC leakage current through a patient's body has been reduced drastically from 4.5 mA to 40 nA for a single and triple layer of matching layers, respectively, as shown in Fig. 7.3 .

Additionally, from the simulations, we found out that the edge-wave artifacts are reduced by ~13dB in imaging simulations. Also, the shielded matching layer improved the bandwidth of the transducer and increased that from 79% to 103% as shown in Fig. 7.4. For the single layer of insulation, we used Parylene C with a thickness of

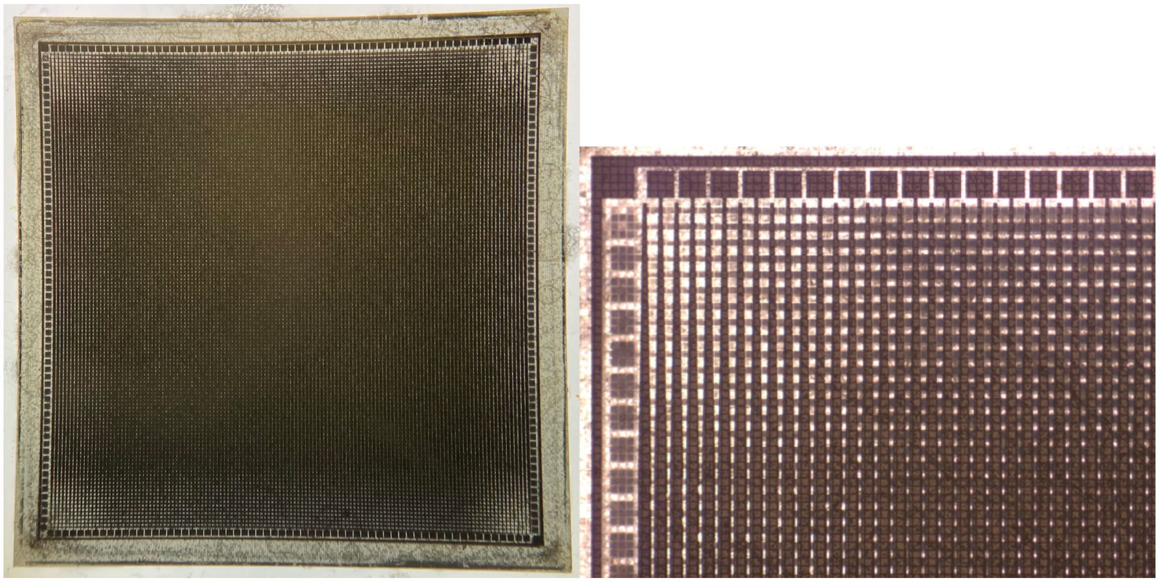

(a) (b)

Figure 7.2: Fabricated 128×128 TOBE arrays with tapered electrodes, (a) showing the entire array, (b) left top corner

46μm, which resulted in a center frequency of ∼8.2 MHz. For the shielded matching layers, we used Parylene C, Copper, and Parylene C layers with the thickness of 11.6μm, 5.1μm, and 13.6μm, respectively. In practice, copper with such a thickness can be deposited via the evaporation method in multiple steps to prevent heating the array.

As a conclusion and suggestion for future works, the proposed method for electrical shielding and tapering the electrodes can be implemented on TOBE arrays to improve performance further. Still, it will require a reliable method for the lithography, such as heating the 1-3 composite material for baking the photoresist, which may result in cracking the array. Alternatively, laser micromachining can create those patterns on the array. although with good progress in making variable DC biasing electronics in our lab, apodization can be dynamically applied to a regular bias-sensitive TOBE array without the need to pattern the electrodes. However, finding a reliable way to pattern the electrodes would also facilitate the fabrication of the transparent TOBE arrays in the handheld format. So ideally, the ultrasound results demonstrated in the

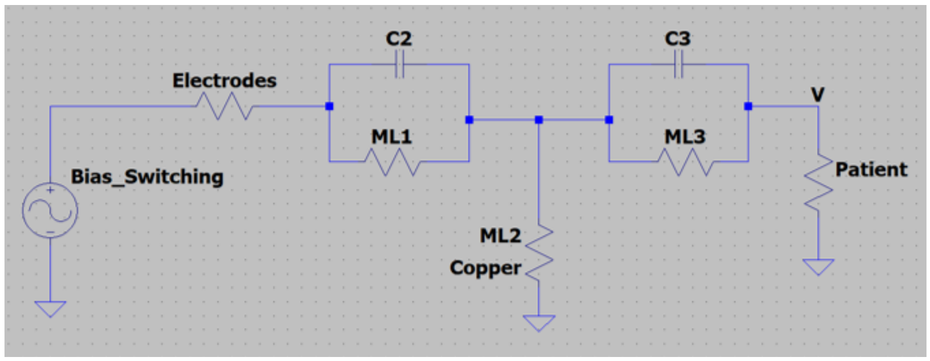

(a)

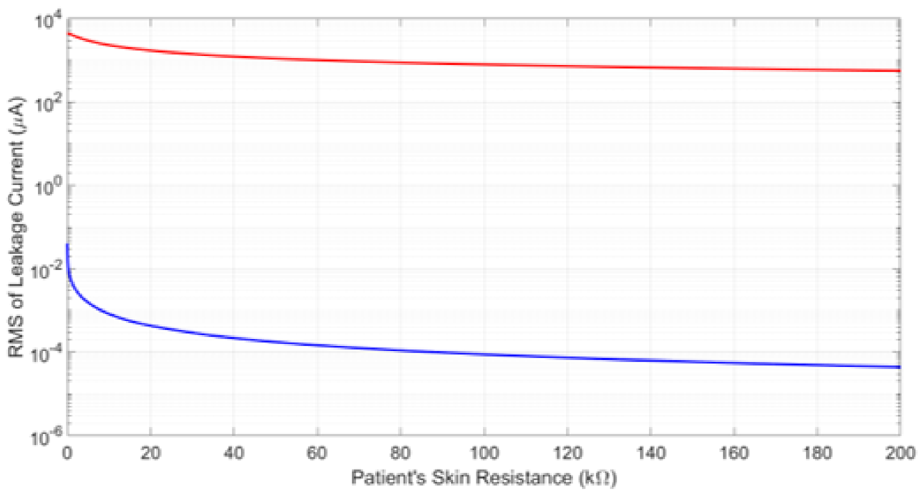

(b)

Figure 7.3: Electrical AC leakage current, (a) A simplified electrical schematic of TOBE array for safety investigation, (b) Induced electrical current through patient's body. The red curve presents the single insulation layer, and the blue curve represents the shielded transducer.

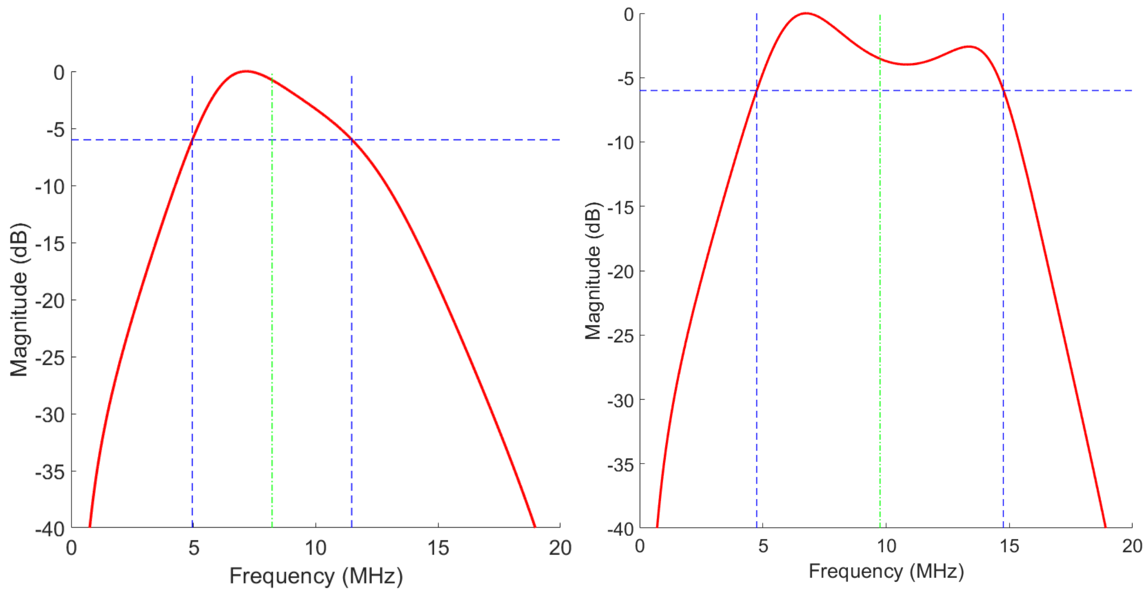

(a) (b)

Figure 7.4: Pulse echo spectrum of the simulated arrays with tapered electrodes and with (a) A single matching layer and (b) A shielded matching layer.

previous chapter would be possible with the transparent version of the bias-sensitive TOBE array with an extra thorough-illumination PA imaging capability.

Lastly, the main objective of this thesis was to fabricate unprecedentedly large handheld bias-sensitive TOBE arrays and compare the ultrasound results with the commercial ultrasound probes. However, the electrical shielding, tapering of the electrodes, and the further development of the transparent TOBE arrays were not pursued in this thesis.

The usage of a quarter-wavelength transducer with a clamped backing instead of a traditional half-wavelength has been initially considered. A backing layer with a huge acoustic impedance is required to satisfy the clamped condition to ensure all the acoustic energy reflects back and only emits into the medium. Such a transducer brings the benefits of lower required DC biasing voltage (half voltage), improved sensitivity, and broader bandwidth but requires further development of fabrication processes, which, however, was not pursued in this thesis.

In the fabricated TOBE arrays, no major difference was noticed when imaging on rows or columns. However, any difference or non-uniformity in the sensitivity of the rows and columns is expected as the backing layer has a slightly greater dielectric constant rather than the front matching layer. This results in more parasitic capacitance on the back side of the TOBE array and would result in dropped sensitivity. However, a coating with the same material as the front matching layer, before using the backing layer would mitigate this non-uniformity issue in the sensitivity. Also, using precise lapping machines with less human-involved technology would also minimize the non-uniformity thickness across the TOBE array and result in uniform frequency response as we have demonstrated in Fig. 6.4(b).

Bibliography

[1] C. Ceroici, T. Harrison, and R. J. Zemp, "Fast orthogonal row–column electronic scanning with top-orthogonal-to-bottom electrode arrays," *IEEE transactions on ultrasonics, ferroelectrics, and frequency control*, vol. 64, no. 6, pp. 1009–1014, 2017.

[2] C. Ceroici, K. Latham, B. A. Greenlay, J. A. Brown, and R. J. Zemp, "Fast orthogonal row–column electronic scanning experiments and comparisons," *IEEE transactions on ultrasonics, ferroelectrics, and frequency control*, vol. 66, no. 6, pp. 1093–1101, 2019.

[3] S. R. F. R. E. Davidsen and B. J. Savord, "Matrix ultrasound probe with passive heat dissipation," May 2012.

[4] B. Savord and R. Solomon, "Fully sampled matrix transducer for real time 3d ultrasonic imaging," in *IEEE Symposium on Ultrasonics, 2003*, IEEE, vol. 1, 2003, pp. 945–953.

[5] D. Shattuck, M. D. Weinshenker, S. W. Smith, and O. T. von Ramm, "Explososcan: A parallel processing technique for high speed ultrasound imaging with linear phased arrays," *The Journal of the Acoustical Society of America*, vol. 75, pp. 1273–1282, 4 1984, ISSN: 0001-4966. DOI: 10.1121/1.390734. [Online]. Available: https://pubmed.ncbi.nlm.nih.gov/6725779/.

[6] M. F. Rasmussen, G. Férin, R. Dufait, and J. A. Jensen, "Comparison of 3d synthetic aperture imaging and explososcan using phantom measurements," in *2012 IEEE International Ultrasonics Symposium*, 2012, pp. 113–116. DOI: 10.1109/ULTSYM.2012.0028.

[7] K. E. Thomenius, "Evolution of ultrasound beamformers," *1996 IEEE Ultrasonics Symposium. Proceedings*, vol. 2, 1615–1622 vol.2, 1996. [Online]. Available: https://api.semanticscholar.org/CorpusID:122729423.

[8] J. Huang, J. K. Triedman, N. V. Vasilyev, Y. Suematsu, R. O. Cleveland, and P. E. Dupont, "Imaging artifacts of medical instruments in ultrasound-guided interventions," *Journal of Ultrasound in Medicine*, vol. 26, no. 10, pp. 1303–1322, 2007. DOI: https://doi.org/10.7863/jum.2007.26.10.1303. eprint: https://onlinelibrary.wiley.com/doi/pdf/10.7863/jum.2007.26.10.1303. [Online]. Available: https://onlinelibrary.wiley.com/doi/abs/10.7863/jum.2007.26.10.1303.

[9] M. R. Sobhani, H. Ozum, G. Yaralioglu, A. Ergun, and A Bozkurt, "Portable low cost ultrasound imaging system," in *2016 IEEE International Ultrasonics Symposium (IUS)*, IEEE, 2016, pp. 1–4.

[10] B. Yin, D. Xing, Y. Wang, Y. Zeng, Y. Tan, and Q. Chen, "Fast photoacoustic imaging system based on 320-element linear transducer array," *Physics in Medicine Biology*, vol. 49, no. 7, p. 1339, 2004. DOI: 10.1088/0031-9155/49/7/019. [Online]. Available: https://dx.doi.org/10.1088/0031-9155/49/7/019.

[11] "3d ultrasound imaging of the carotid arteries," *Current Drug Targets - Cardiovascular Hematological Disorders*, vol. 4, no. 2, pp. 161–175, 2004, ISSN: 1568-0061/1568-0061. DOI: 10.2174/1568006043336311.

[12] O. V. Solberg, F. Lindseth, H. Torp, R. E. Blake, and T. A. N. Hernes, "Freehand 3d ultrasound reconstruction algorithms—a review," *Ultrasound in medicine & biology*, vol. 33, no. 7, pp. 991–1009, 2007.

[13] J. Provost *et al.*, "3d ultrafast ultrasound imaging in vivo," *Physics in Medicine & Biology*, vol. 59, no. 19, p. L1, 2014.

[14] M. M. Nguyen *et al.*, "Real-time x-plane shear wave elastography feasibility on philips 2d xmatrix transducer," in *2018 IEEE International Ultrasonics Symposium (IUS)*, 2018, pp. 1–9. DOI: 10.1109/ULTSYM.2018.8580080.

[15] A. Austeng and S. Holm, "Sparse 2-d arrays for 3-d phased array imaging-design methods," *IEEE transactions on ultrasonics, ferroelectrics, and frequency control*, vol. 49, no. 8, pp. 1073–1086, 2002.

[16] A. Ramalli, E. Boni, E. Roux, H. Liebgott, and P. Tortoli, "Design, Implementation, and Medical Applications of 2-D Ultrasound Sparse Arrays," *IEEE Transactions on Ultrasonics, Ferroelectrics and Frequency Control*, vol. 69, no. 10, pp. 2739–2755, Oct. 2022. DOI: 10.1109/TUFFC.2022.3162419. [Online]. Available: https://hal.science/hal-04212919.

[17] G. Lockwood and F. Foster, "Optimizing sparse two-dimensional transducer arrays using an effective aperture approach," in *1994 Proceedings of IEEE Ultrasonics Symposium*, vol. 3, 1994, 1497–1501 vol.3. DOI: 10.1109/ULTSYM.1994.401874.

[18] G. Lookwood and F. Foster, "Optimizing the radiation pattern of sparse periodic two-dimensional arrays," *IEEE Transactions on Ultrasonics, Ferroelectrics, and Frequency Control*, vol. 43, no. 1, pp. 15–19, 1996. DOI: 10.1109/58.484458.

[19] S. I. Nikolov and J. A. Jensen, "Application of different spatial sampling patterns for sparse array transducer design," *Ultrasonics*, vol. 37, no. 10, pp. 667–671, 2000, ISSN: 0041-624X. DOI: https://doi.org/10.1016/S0041-624X(00)00013-5. [Online]. Available: https://www.sciencedirect.com/science/article/pii/S0041624X00000135.

[20] T. Sumanaweera, J. Schwartz, and D. Napolitano, "A spiral 2d phased array for 3d imaging," in *1999 IEEE Ultrasonics Symposium. Proceedings. International Symposium (Cat. No.99CH37027)*, vol. 2, 1999, 1271–1274 vol.2. DOI: 10.1109/ULTSYM.1999.849228.

[21] O. Martínez-Graullera, C. J. Martín, G. Godoy, and L. G. Ullate, "2d array design based on fermat spiral for ultrasound imaging," *Ultrasonics*, vol. 50, no. 2, pp. 280–289, 2010, Selected Papers from ICU 2009, ISSN: 0041-624X. DOI: https://doi.org/10.1016/j.ultras.2009.09.010. [Online]. Available: https://www.sciencedirect.com/science/article/pii/S0041624X09001115.

[22] H. Yoon and T.-K. Song, "Sparse rectangular and spiral array designs for 3d medical ultrasound imaging," *Sensors*, vol. 20, no. 1, 2020, ISSN: 1424-8220. DOI: 10.3390/s20010173. [Online]. Available: https://www.mdpi.com/1424-8220/20/1/173.

[23] M. H. Masoumi, T. Kaddoura, and R. J. Zemp, "Costas sparse 2-d arrays for high-resolution ultrasound imaging," *IEEE Transactions on Ultrasonics, Ferroelectrics, and Frequency Control*, vol. 70, no. 5, pp. 460–472, 2023. DOI: 10.1109/TUFFC.2023.3256339.

[24] F. Cassaing and L. M. Mugnier, "Optimal sparse apertures for phased-array imaging," *Opt. Lett.*, vol. 43, no. 19, pp. 4655–4658, 2018. DOI: 10.1364/OL.43.004655. [Online]. Available: https://opg.optica.org/ol/abstract.cfm?URI=ol-43-19-4655.

[25] G. Lockwood, J. Talman, and S. Brunke, "Real-time 3-d ultrasound imaging using sparse synthetic aperture beamforming," *IEEE Transactions on Ultrasonics, Ferroelectrics, and Frequency Control*, vol. 45, no. 4, pp. 980–988, 1998. DOI: 10.1109/58.710573.

[26] M. Karaman, I. O. Wygant, Oralkan, and B. T. Khuri-Yakub, "Minimally redundant 2-d array designs for 3-d medical ultrasound imaging," *IEEE Transactions on Medical Imaging*, vol. 28, no. 7, pp. 1051–1061, 2009. DOI: 10.1109/TMI.2008.2010936.

[27] A. Ramalli, E. Boni, A. S. Savoia, and P. Tortoli, "Density-tapered spiral arrays for ultrasound 3-d imaging," *IEEE Transactions on Ultrasonics, Ferroelectrics, and Frequency Control*, vol. 62, no. 8, pp. 1580–1588, 2015. DOI: 10.1109/TUFFC.2015.007035.

[28] V. F. P. L. C. C. T. P. L. H. Roux Emmanuel, "Experimental 3-d ultrasound imaging with 2-d sparse arrays using focused and diverging waves," *Scientific Reports*, 2018. DOI: 10.1038/s41598-018-27490-2. [Online]. Available: https://doi.org/10.1038/s41598-018-27490-2.

[29] B. Qi *et al.*, "Deep learning assisted sparse array ultrasound imaging," *PLOS ONE*, vol. 18, no. 10, pp. 1–17, Oct. 2023. DOI: 10.1371/journal.pone.0293468. [Online]. Available: https://doi.org/10.1371/journal.pone.0293468.

[30] C. Chen *et al.*, "A front-end asic with receive sub-array beamforming integrated with a 32×32 pzt matrix transducer for 3-d transesophageal echocardiography," *IEEE Journal of Solid-State Circuits*, vol. 52, no. 4, pp. 994–1006, 2017. DOI: 10.1109/JSSC.2016.2638433.

[31] J. Janjic *et al.*, "A 2-d ultrasound transducer with front-end asic and low cable count for 3-d forward-looking intravascular imaging: Performance and characterization," *IEEE Transactions on Ultrasonics, Ferroelectrics, and Frequency Control*, vol. 65, no. 10, pp. 1832–1844, 2018. DOI: 10.1109/TUFFC.2018.2859824.

[32] G. Matrone, A. S. Savoia, M. Terenzi, G. Caliano, F. Quaglia, and G. Magenes, "A volumetric cmut-based ultrasound imaging system simulator with integrated reception and -beamforming electronics models," *IEEE Transactions on Ultrasonics, Ferroelectrics, and Frequency Control*, vol. 61, no. 5, pp. 792–804, 2014. DOI: 10.1109/TUFFC.2014.2971.

[33] S. Blaak *et al.*, "Design of a micro-beamformer for a 2d piezoelectric ultrasound transducer," in *2009 IEEE International Ultrasonics Symposium*, 2009, pp. 1338–1341. DOI: 10.1109/ULTSYM.2009.5441534.

[34] B. Savord and R. Solomon, "Fully sampled matrix transducer for real time 3d ultrasonic imaging," in *IEEE Symposium on Ultrasonics, 2003*, vol. 1, 2003, 945–953 Vol.1. DOI: 10.1109/ULTSYM.2003.1293556.

[35] H. M. H. T. Toshio Kondo Yutaka Sato, "Ultrasonic diagnostic apparatus," pat. US5060651A, 1990.

[36] C. E. Demore, A. W. Joyce, K. Wall, and G. R. Lockwood, "Real-time volume imaging using a crossed electrode array," *IEEE transactions on ultrasonics, ferroelectrics, and frequency control*, vol. 56, no. 6, pp. 1252–1261, 2009.

[37] C. H. Seo and J. T. Yen, "A 256 x 256 2-d array transducer with row-column addressing for 3-d rectilinear imaging," *IEEE transactions on ultrasonics, ferroelectrics, and frequency control*, vol. 56, no. 4, pp. 837–847, 2009.

[38] C. E. Morton and G. R. Lockwood, "Theoretical assessment of a crossed electrode 2-d array for 3-d imaging," in *IEEE Symposium on Ultrasonics, 2003*, IEEE, vol. 1, 2003, pp. 968–971.

[39] M. F. Rasmussen, T. L. Christiansen, E. V. Thomsen, and J. A. Jensen, "3-d imaging using row-column-addressed arrays with integrated apodization - part i: Apodization design and line element beamforming," *IEEE Transactions on Ultrasonics, Ferroelectrics, and Frequency Control*, vol. 62, no. 5, pp. 947–958, 2015. DOI: 10.1109/TUFFC.2014.006531.

[40] C.-S. Mei and M.-L. Li, "Improved row-column-addressed array imaging by leveraging ghost echoes," in *2023 IEEE International Ultrasonics Symposium (IUS)*, 2023, pp. 1–3. DOI: 10.1109/IUS51837.2023.10306432.

[41] M Flesch *et al.*, "4d in vivo ultrafast ultrasound imaging using a row-column addressed matrix and coherently-compounded orthogonal plane waves," *Physics in Medicine & Biology*, vol. 62, no. 11, p. 4571, 2017.

[42] J. A. Jensen *et al.*, "Anatomic and functional imaging using row–column arrays," *IEEE Transactions on Ultrasonics, Ferroelectrics, and Frequency Control*, vol. 69, no. 10, pp. 2722–2738, 2022, ISSN: 1525-8955. DOI: 10.1109/TUFFC.2022.3191391.

[43] M. Engholm, C. Beers, H. Bouzari, J. A. Jensen, and E. V. Thomsen, "Increasing the field-of-view of row–column-addressed ultrasound transducers: Implementation of a diverging compound lens," *Ultrasonics*, vol. 88, pp. 97–105, 2018, ISSN: 0041-624X. DOI: https://doi.org/10.1016/j.ultras.2018.02.001. [Online]. Available: https://www.sciencedirect.com/science/article/pii/S0041624X17309265.

[44] A. Salari, M. Audoin, B. G. Tomov, E. Vilain Thomsen, and J. A. Jensen, "Increasing penetration depth and field-of-view in 3d ultrasound imaging with a lensed row-column array," in *2023 IEEE International Ultrasonics Symposium (IUS)*, 2023, pp. 1–4. DOI: 10.1109/IUS51837.2023.10307409.

[45] M. Audoin, A. Salari, B. G. Tomov, K. F. Pedersen, J. A. Jensen, and E. V. Thomsen, "Diverging polymer acoustic lens design for high-resolution row-column array ultrasound transducers," *IEEE Transactions on Ultrasonics, Ferroelectrics, and Frequency Control*, pp. 1–1, 2023. DOI: 10.1109/TUFFC.2023.3327567.

[46] M. Audoin, A. Salari, B. G. Tomov, J. Arendt Jensen, and E. V. Thomsen, "Novel diverging acoustic lens geometries for row-column array transducers," in *2023 IEEE International Ultrasonics Symposium (IUS)*, 2023, pp. 1–4. DOI: 10.1109/IUS51837.2023.10306503.

[47] A. Sampaleanu, P. Zhang, A. Kshirsagar, W. Moussa, and R. J. Zemp, "Top-orthogonal-to-bottom-electrode (tobe) cmut arrays for 3-d ultrasound imaging," *IEEE transactions on ultrasonics, ferroelectrics, and frequency control*, vol. 61, no. 2, pp. 266–276, 2014.

[48] K. Latham, C. Ceroici, C. A. Samson, R. J. Zemp, and J. A. Brown, "Simultaneous azimuth and fresnel elevation compounding: A fast 3-d imaging technique for crossed-electrode arrays," *IEEE transactions on ultrasonics, ferroelectrics, and frequency control*, vol. 65, no. 9, pp. 1657–1668, 2018.

[49] C. Ceroici, K. Latham, R. Chee, J. A. Brown, and R. J. Zemp, "Bias-sensitive crossed-electrode relaxor 2d arrays for 3d photoacoustic imaging," in *Photons Plus Ultrasound: Imaging and Sensing 2018*, International Society for Optics and Photonics, vol. 10494, 2018, p. 1 049 420.

[50] C. Ceroici *et al.*, "3d photoacoustic imaging using hadamard-bias encoding with a crossed electrode relaxor array," *Opt. Lett.*, vol. 43, no. 14, pp. 3425–3428, 2018. DOI: 10.1364/OL.43.003425. [Online]. Available: https://opg.optica.org/ol/abstract.cfm?URI=ol-43-14-3425.

[51] M. Ghavami, M. R. Sobhani, and R. Zemp, "Transparent row-column CMUT arrays for volumetric photoacoustic imaging (Withdrawal Notice)," C. Kim, J. Laufer, V. Ntziachristos, and R. J. Zemp, Eds., International Society for Optics and Photonics, vol. 12631, SPIE, 2023, 126310O. DOI: 10.1117/12.2670786. [Online]. Available: https://doi.org/10.1117/12.2670786.

[52] Y. Wang, S. Hu, K. Maslov, Y. Zhang, Y. Xia, and L. V. Wang, "In vivo integrated photoacoustic and confocal microscopy of hemoglobin oxygen saturation and oxygen partial pressure," *Opt. Lett.*, vol. 36, no. 7, pp. 1029–1031, 2011. DOI: 10.1364/OL.36.001029. [Online]. Available: https://opg.optica.org/ol/abstract.cfm?URI=ol-36-7-1029.

[53] P. Beard, "Biomedical photoacoustic imaging," *Interface Focus*, vol. 1, no. 4, pp. 602–631, 2011. DOI: 10.1098/rsfs.2011.0028. eprint: https://royalsocietypublishing.org/doi/pdf/10.1098/rsfs.2011.0028. [Online]. Available: https://royalsocietypublishing.org/doi/abs/10.1098/rsfs.2011.0028.

[54] K. W. R. J. Paproski A. Heinmiller and R. J. Zemp, "Multi-wavelength photoacoustic imaging of inducible tyrosinase reporter gene expression in xenograft tumors," *Scientific reports*, vol. 4, 2014. DOI: https://doi.org/10.1038/srep05329.

[55] M. Xu and L. V. Wang, "Photoacoustic imaging in biomedicine," *Review of Scientific Instruments*, vol. 77, no. 4, p. 041 101, 2006. DOI: 10.1063/1.2195024. eprint: https://doi.org/10.1063/1.2195024. [Online]. Available: https://doi.org/10.1063/1.2195024.

[56] L. V. Wang and H. Wu, *Biomedical Optics*. John Wiley Sons, Inc., Publication, New Jersey, 2007.

[57] R. S. Cobbold, *Foundations of biomedical ultrasound*. Oxford university press, 2006.

[58] S. AR. and S. Gehlhach, "Klm transducer model implementation using transfer matrices," *IEEE Ultrasonics Symp*, 1985.

[59] G. M. R. Krimholtz D.A. Leedom, "New equivalent circuits for elementary piezoelectric transducers," *Electronics Letters*, vol. 6, 398–399(1), 13 1970. [Online]. Available: https://digital-library.theiet.org/content/journals/10.1049/el_19700280.

[60] D. Leedom, R. Krimholtz, and G. Matthaei, "Equivalent circuits for transducers having arbitrary even- or odd-symmetry piezoelectric excitation," *IEEE Transactions on Sonics and Ultrasonics*, vol. 18, no. 3, pp. 128–141, 1971. DOI: 10.1109/T-SU.1971.29608.

[61] W. Smith and B. Auld, "Modeling 1-3 composite piezoelectrics: Thickness-mode oscillations," *IEEE Transactions on Ultrasonics, Ferroelectrics, and Frequency Control*, vol. 38, no. 1, pp. 40–47, 1991. DOI: 10.1109/58.67833.

[62] W. Smith, "Modeling 1-3 composite piezoelectrics: Hydrostatic response," *IEEE Transactions on Ultrasonics, Ferroelectrics, and Frequency Control*, vol. 40, no. 1, pp. 41–49, 1993. DOI: 10.1109/58.184997.

[63] M. Xu and L. V. Wang, "Photoacoustic imaging in biomedicine," *Review of Scientific Instruments*, vol. 77, no. 4, p. 041 101, Apr. 2006, ISSN: 0034-6748. DOI: 10.1063/1.2195024. eprint: https://pubs.aip.org/aip/rsi/article-pdf/doi/10.1063/1.2195024/14017374/041101_1_online.pdf. [Online]. Available: https://doi.org/10.1063/1.2195024.

[64] M. W. Schellenberg and H. K. Hunt, "Hand-held optoacoustic imaging: A review," *Photoacoustics*, vol. 11, pp. 14–27, 2018, ISSN: 2213-5979. DOI: https://doi.org/10.1016/j.pacs.2018.07.001. [Online]. Available: https://www.sciencedirect.com/science/article/pii/S2213597918300077.

[65] G. W. Brodie, Y. Qiu, S. Cochran, G. C. Spalding, and M. P. Macdonald, "Letters: Optically transparent piezoelectric transducer for ultrasonic particle manipulation," *IEEE Transactions on Ultrasonics, Ferroelectrics, and Frequency Control*, vol. 61, no. 3, pp. 389–391, 2014. DOI: 10.1109/TUFFC.2014.2923.

[66] Z. Li, A. K. Ilkhechi, and R. Zemp, "Transparent capacitive micromachined ultrasonic transducers (cmuts) for photoacoustic applications," *Opt. Express*, vol. 27, no. 9, pp. 13 204–13 218, 2019. DOI: 10.1364/OE.27.013204. [Online]. Available: https://opg.optica.org/oe/abstract.cfm?URI=oe-27-9-13204.

[67] A. Dangi, S. Agrawal, and S.-R. Kothapalli, "Lithium niobate-based transparent ultrasound transducers for photoacoustic imaging," *Opt. Lett.*, vol. 44, no. 21, pp. 5326–5329, 2019. DOI: 10.1364/OL.44.005326. [Online]. Available: https://opg.optica.org/ol/abstract.cfm?URI=ol-44-21-5326.

[68] H. Chen *et al.*, "Optical-resolution photoacoustic microscopy using transparent ultrasound transducer," *Sensors*, vol. 19, no. 24, 2019, ISSN: 1424-8220. DOI: 10.3390/s19245470. [Online]. Available: https://www.mdpi.com/1424-8220/19/24/5470.

[69] R. Chen *et al.*, "Transparent high-frequency ultrasonic transducer for photoacoustic microscopy application," *IEEE Transactions on Ultrasonics, Ferroelectrics, and Frequency Control*, vol. 67, no. 9, pp. 1848–1853, 2020. DOI: 10.1109/TUFFC.2020.2985369.

[70] J. Park *et al.*, "Seamlessly integrated multi-modal imaging system through transparent ultrasound transducer in vivo," in *Photons Plus Ultrasound: Imaging and Sensing 2021*, A. A. Oraevsky and L. V. Wang, Eds., International Society for Optics and Photonics, vol. 11642, SPIE, 2021, 116420B. DOI: 10.1117/12.2577208. [Online]. Available: https://doi.org/10.1117/12.2577208.

[71] A. K. Ilkhechi, C. Ceroici, Z. Li, and R. Zemp, "Transparent capacitive micromachined ultrasonic transducer (cmut) arrays for real-time photoacoustic applications," *Opt. Express*, vol. 28, no. 9, pp. 13 750–13 760, 2020. DOI: 10.1364/OE.390612. [Online]. Available: https://opg.optica.org/oe/abstract.cfm?URI=oe-28-9-13750.

[72] A. K. Ilkhechi, C. Ceroici, and R. J. Zemp, "High sensitivity transparent capacitive micromachined ultrasound transducer linear arrays for optical, photoacoustic and ultrasound imaging," in *Photons Plus Ultrasound: Imaging and Sensing 2021*, A. A. Oraevsky and L. V. Wang, Eds., International Society for Optics and Photonics, vol. 11642, SPIE, 2021, 116421Z. DOI: 10.1117/12.2578919. [Online]. Available: https://doi.org/10.1117/12.2578919.

[73] C. Ceroici, K. Latham, B. A. Greenlay, J. A. Brown, and R. J. Zemp, "Fast orthogonal row–column electronic scanning experiments and comparisons," *IEEE Transactions on Ultrasonics, Ferroelectrics, and Frequency Control*, vol. 66, no. 6, pp. 1093–1101, 2019. DOI: 10.1109/TUFFC.2019.2906599.

[74] H. Jiang *et al.*, "Transparent electro-optic ceramics and devices," in *Optoelectronic Devices and Integration*, H. Ming, X. Zhang, and M. Y. Chen, Eds., International Society for Optics and Photonics, vol. 5644, SPIE, 2005, pp. 380 –394. DOI: 10.1117/12.582105. [Online]. Available: https://doi.org/10.1117/12.582105.

[75] C. Ceroici, K. Latham, R. Chee, J. A. Brown, and R. J. Zemp, "Bias-sensitive crossed-electrode relaxor 2D arrays for 3D photoacoustic imaging," in *Photons Plus Ultrasound: Imaging and Sensing 2018*, A. A. Oraevsky and L. V. Wang, Eds., International Society for Optics and Photonics, vol. 10494, SPIE, 2018, p. 1 049 420. DOI: 10.1117/12.2288854. [Online]. Available: https://doi.org/10.1117/12.2288854.

[76] K. Latham, C. Samson, J. Woodacre, and J. Brown, "A 30-mhz, 3-d imaging, forward-looking miniature endoscope based on a 128-element relaxor array," *IEEE Transactions on Ultrasonics, Ferroelectrics, and Frequency Control*, vol. 68, no. 4, pp. 1261–1271, 2021. DOI: 10.1109/TUFFC.2020.3027907.

[77] C. Zhang, K. I. Maslov, J. Yao, and L. V. Wang, "In vivo photoacoustic microscopy with 7.6-µm axial resolution using a commercial 125-MHz ultrasonic transducer," *Journal of Biomedical Optics*, vol. 17, no. 11, p. 116 016, 2012. DOI: 10.1117/1.JBO.17.11.116016. [Online]. Available: https://doi.org/10.1117/1.JBO.17.11.116016.

[78] Y. Jiang, A. Forbrich, T. Harrison, and R. J. Zemp, "Blood oxygen flux estimation with a combined photoacoustic and high-frequency ultrasound microscopy system: a phantom study," *Journal of Biomedical Optics*, vol. 17, no. 3, p. 036 012, 2012. DOI: 10.1117/1.JBO.17.3.036012. [Online]. Available: https://doi.org/10.1117/1.JBO.17.3.036012.

[79] M. R. Sobhani, M. Ghavami, A. K. Ilkhechi, J. Brown, and R. Zemp, "Ultrafast orthogonal row–column electronic scanning (uforces) with bias-switchable top-orthogonal-to-bottom electrode 2-d arrays," *IEEE Transactions on Ultrasonics, Ferroelectrics, and Frequency Control*, vol. 69, no. 10, pp. 2823–2836, 2022. DOI: 10.1109/TUFFC.2022.3189345.

[80] G. Lockwood, J. Talman, and S. Brunke, "Real-time 3-d ultrasound imaging using sparse synthetic aperture beamforming," *IEEE Transactions on Ultrasonics, Ferroelectrics, and Frequency Control*, vol. 45, no. 4, pp. 980–988, 1998. DOI: 10.1109/58.710573.

[81] M. Correia, J. Provost, M. Tanter, and M. Pernot, "4d ultrafast ultrasound flow imaging: In vivo quantification of arterial volumetric flow rate in a single heartbeat," *Physics in Medicine & Biology*, vol. 61, no. 23, p. L48, 2016.

[82] A. S. Logan, L. L. Wong, A. I. Chen, and J. T. Yeow, "A 32 x 32 element row-column addressed capacitive micromachined ultrasonic transducer," *IEEE transactions on ultrasonics, ferroelectrics, and frequency control*, vol. 58, no. 6, pp. 1266–1271, 2011.

[83] H. Bouzari, M. Engholm, S. I. Nikolov, M. B. Stuart, E. V. Thomsen, and J. A. Jensen, "Imaging performance for two row–column arrays," *IEEE Transactions on Ultrasonics, Ferroelectrics, and Frequency Control*, vol. 66, no. 7, pp. 1209–1221, 2019. DOI: 10.1109/TUFFC.2019.2914348.

[84] S. Holbek, T. L. Christiansen, M. B. Stuart, C. Beers, E. V. Thomsen, and J. A. Jensen, "3-d vector flow estimation with row–column-addressed arrays," *IEEE Transactions on Ultrasonics, Ferroelectrics, and Frequency Control*, vol. 63, no. 11, pp. 1799–1814, 2016. DOI: 10.1109/TUFFC.2016.2582536.

[85] A. Savoia *et al.*, "P2b-4 crisscross 2d cmut array: Beamforming strategy and synthetic 3d imaging results," in *2007 IEEE Ultrasonics Symposium Proceedings*, 2007, pp. 1514–1517. DOI: 10.1109/ULTSYM.2007.381.

[86] A. Stuart Savoia *et al.*, "A 120+ 120- element crisscross cmut probe's with real-time switchable electronic and fresnel focusing capabilities," in *2018 IEEE International Ultrasonics Symposium (IUS)*, 2018, pp. 1–4. DOI: 10.1109/ULTSYM.2018.8580084.

[87] J. Brown, C. Samson, and K. Latham, "Systems and methods for ultrasound beamforming using coherently compounded fresnel focussing," pat. WO 2018/107299, 2017.

[88] C. Ceroici *et al.*, "3d photoacoustic imaging using hadamard-bias encoding with a crossed electrode relaxor array," *Optics letters*, vol. 43, no. 14, pp. 3425–3428, 2018.

[89] J. A. Jensen and N. B. Svendsen, "Calculation of pressure fields from arbitrarily shaped, apodized, and excited ultrasound transducers," *IEEE transactions on ultrasonics, ferroelectrics, and frequency control*, vol. 39, no. 2, pp. 262–267, 1992.

[90] M. Patterson and F. Foster, "The improvement and quantitative assessment of b-mode images produced by an annular array/cone hybrid," *Ultrasonic Imaging*, vol. 5, no. 3, pp. 195–213, 1983.

[91] M. R. Sobhani, K. Latham, J. Brown, and R. J. Zemp, "Bias-sensitive transparent single-element ultrasound transducers using hot-pressed pmn-pt," *OSA Continuum*, vol. 4, no. 10, pp. 2606–2614, 2021.

[92] M. Ghavami, A. K. Ilkhechi, and R. Zemp, "Flexible transparent cmut arrays for photoacoustic tomography," *Opt. Express*, vol. 30, no. 10, pp. 15 877–15 894, 2022.

[93] R. S. Cobbold, *Foundations of biomedical ultrasound*. Oxford university press, 2006.

[94] A. Kashani Ilkhechi, "Transparent transducers and fast electronics for next-generation ultrasound and photoacoustic imaging," Ph.D. dissertation, Department of Electrical and Computer Engineering, University of Alberta, Edmonton, AB, Canada, 2022.

[95] M. Ghavami, A. K. Ilkhechi, and R. Zemp, "Flexible transparent cmut arrays for photoacoustic tomography," *Opt. Express*, vol. 30, no. 10, pp. 15 877–15 894, 2022. DOI: 10.1364/OE.455796. [Online]. Available: https://opg.optica.org/oe/abstract.cfm?URI=oe-30-10-15877.

[96] M. R. Sobhani, K. Latham, J. Brown, and R. J. Zemp, "Bias-sensitive transparent single-element ultrasound transducers using hot-pressed pmn-pt," *OSA Continuum*, vol. 4, no. 10, pp. 2606–2614, 2021. DOI: 10.1364/OSAC.426779. [Online]. Available: https://opg.optica.org/osac/abstract.cfm?URI=osac-4-10-2606.

[97] M. W. Schellenberg and H. K. Hunt, "Hand-held optoacoustic imaging: A review," *Photoacoustics*, vol. 11, pp. 14–27, 2018, ISSN: 2213-5979. DOI: https://doi.org/10.1016/j.pacs.2018.07.001. [Online]. Available: https://www.sciencedirect.com/science/article/pii/S2213597918300077.

[98] M. Ghavami, M. R. Sobhani, and R. Zemp, "Transparent dual-frequency cmut arrays for photoacoustic imaging," *IEEE Transactions on Ultrasonics, Ferroelectrics, and Frequency Control*, vol. 70, no. 12, pp. 1621–1630, 2023. DOI: 10.1109/TUFFC.2023.3331356.

[99] A. Omidvar, E. Cretu, R. Rohling, M. Cresswell, and A. J. Hodgson, "Flexible polycmuts: Fabrication and characterization of a flexible polymer-based capacitive micromachined ultrasonic array for conformal ultrasonography," *Advanced Materials Technologies*, vol. 8, no. 5, p. 2 201 316, 2023. DOI: https://doi.org/10.1002/admt.202201316. eprint: https://onlinelibrary.wiley.com/doi/pdf/10.1002/admt.202201316. [Online]. Available: https://onlinelibrary.wiley.com/doi/abs/10.1002/admt.202201316.

[100] M. R. Sobhani, M. Ghavami, and R. Zemp, "Bias-Sensitive 128x128 hand-held TOBE ultrasound probe based on electrostrictive PMN-PT for photoacoustic applications (Withdrawal Notice)," in *Opto-Acoustic Methods and Applications in Biophotonics VI*, C. Kim, J. Laufer, V. Ntziachristos, and R. J. Zemp, Eds., International Society for Optics and Photonics, vol. 12631, SPIE, 2023,

p. 126310V. DOI: 10.1117/12.2671017. [Online]. Available: https://doi.org/10.1117/12.2671017.

[101] C. Ceroici *et al.*, "3d photoacoustic imaging using hadamard-bias encoding with a crossed electrode relaxor array," *Opt. Lett.*, vol. 43, no. 14, pp. 3425–3428, 2018. DOI: 10.1364/OL.43.003425. [Online]. Available: https://opg.optica.org/ol/abstract.cfm?URI=ol-43-14-3425.

[102] A. K. Ilkhechi *et al.*, "High-voltage bias-switching electronics for volumetric imaging using electrostrictive row–column arrays," *IEEE Transactions on Ultrasonics, Ferroelectrics, and Frequency Control*, vol. 70, no. 4, pp. 324–335, 2023. DOI: 10.1109/TUFFC.2023.3246424.

[103] C. Wong *et al.*, "20-mhz phased array ultrasound transducer for in vivo ultrasound imaging of small animals," *Ultrasonics*, vol. 126, p. 106 821, 2022, ISSN: 0041-624X. DOI: https://doi.org/10.1016/j.ultras.2022.106821. [Online]. Available: https://www.sciencedirect.com/science/article/pii/S0041624X22001275.

Appendix A: KLM Modeling

The following MATLAB code is a simplified script used for calculating the input impedance and the P/E spectrum of a transducer for given matching layers and properties of the active layer (piezoelectric or electrostrictive). The properties of the PMN38 are estimated here and may not be accurate.

```
%   | Medium 1 | Backing | Electrode | ...
%   Active Element | Electrode | ML1 | ML 2 | ML 3 | Medium 2 |
%   Last Update: Oct 6, 2020
%   Written By: Mohammad R. Sobhani

clear all;
close all;
clc;

eps = 1e-30;
fmin = eps;
fmax = 40e6;
fstep = 5e3;
f = fmin:fstep:fmax;
PI = 3.14159265;

A = (8e-3) * (107e-6);        % area of the active element
PE_t = 157e-6;                % thickness of the active elemnt ,
   Piezoelectric ...
w = (2 .* PI .* f);
eS0 = 8.854178e-12;       %[F/m]
C_Par = 0;                % Input Parasitic Cap

%% Back and Front Electrode Layers
alpha_Cond_Layer = eps;        % Attenuation : Unit = [Nepers/m]   ,
      (dB/m = 8.686*alpha)
Cond_Layer_t = 500e-9;
vL_Cond_Layer =  4660;         % Unit = [m/s] , Gold ~  3240 ,
   Copper ~  4660 , Al ~ 6320 ,
```

```
Z0_Cond_Layer =  41.61e6;        % Unit = [Rayl] , Gold ~  62.6e6
    , Copper ~  41.61e6  , Al ~ 617.1e6

%% Backing Layer
alpha_Backing_Layer = eps;     % Epoxy301 : ~1300 Nepers/m or ~12
    dB/mm @ 30 MHz>>
Backing_Layer_t = eps;
vL_Backing_Layer = 1850;         % Epoxy301 ~ 2650 , E-Solder3022
    ~ 1850
Z0_Backing_Layer = 5.75e6;       % Epoxy301_Alumina ~ 5.5-6e6 ,
    Epoxy301 ~ 3.05e6  , E-Solder3022 ~ 5.9e6

%% Matching Layer #1:
alpha_Matching_Layer_1 = eps;
Matching_Layer_t_1 = 46e-6;
vL_Matching_Layer_1 = 2135;        % Parylene C ~ 2135 - 2200 ,
    Copper ~  4660
Z0_Matching_Layer_1 = 2.65e6;       % Parylene C ~ 2.6e6-2.65e6  ,
    Copper ~  41.61e6

%% Matching Layer #2:
alpha_Matching_Layer_2 = eps;
Matching_Layer_t_2 = eps;
vL_Matching_Layer_2 = 4660;        % Parylene C ~ 2135 - 2200 ,
    Copper ~  4660
Z0_Matching_Layer_2 = 41.61e6;       % Parylene C ~ 2.6e6-2.65e6  ,
     Copper ~  41.61e6

%% Matching Layer #3:
alpha_Matching_Layer_3 = eps;
Matching_Layer_t_3 = eps;
vL_Matching_Layer_3 = 2135;        % Parylene C ~ 2135 - 2200 ,
    Copper ~  4660
Z0_Matching_Layer_3 = 2.65e6;       % Parylene C ~ 2.6e6-2.65e6  ,
    Copper ~  41.61e6

%% Mediums
count = 3;
[x y] = size(f);
Alpha_Np_Total = zeros(count,y); %Water, Blood, Air
Acous_Pro_Total = zeros(count,4); %rho (Kg/m^3), VL (m/s), u (Pa.
    s), k (Pa^-1)
Acous_Pro_Total(1, :) = [998 1489 0.89e-3 0.455e-9];
Acous_Pro_Total(2, :) = [1055 1580 3.5e-3 0.38e-9];
Acous_Pro_Total(3, :) = [1.204 343.3 0.01813e-3 7047e-9];
R = zeros(count,y);
X = zeros(count,y);
```

```
Z0_Total = zeros(count,y);

for i=1:count
    Alpha_Np_Total(i, :) = (2.*w.^2.*Acous_Pro_Total(i, 4)*
        Acous_Pro_Total(i, 3))./(3*Acous_Pro_Total(i, 2));
    R(i,:) = (Acous_Pro_Total(i, 1)*Acous_Pro_Total(i, 2).*w.^2)
        /(w.^2 + (Alpha_Np_Total(i, :).^2 .* Acous_Pro_Total(i, 2)
        ^2));
    X(i,:) = (Acous_Pro_Total(i, 1) * Acous_Pro_Total(i, 2)^2 .*
        w .* Alpha_Np_Total(i, :))/(w.^2 + (Alpha_Np_Total(i, :)
        .^2 .* Acous_Pro_Total(i, 2)^2));
    Z0_Total(i,:) = R(i,:) + j.*X(i,:);
end

Z0_Medium_Back = Z0_Backing_Layer .* ones(1,y);     % Alumina-
    Loaded Epoxy
Z0_Medium_Front = Z0_Total(1,:);    % Water

%% Active Layer, Parameters are estimated for the PMN38-Epoxy301
    1-3 Composite
alpha_PE = eps;
tan_sigma_PE = eps;
kt_square_PE = 0.775^2;     % 36 Y-Cut Lithium Niobate ~ 0.46 -
    0.485
eS33 = 1308 * eS0;          % 36 Y-Cut Lithium Niobate ~
    27.9-28.7
vL_PE = 3376.35;            % HP-PMN ~ 4770 , 36 Y-Cut Lithium
    Niobate ~ 7340
CS0 = A * eS33 / PE_t;
w0 = (PI/PE_t) * vL_PE;     % unloaded Antiresonant Freq
Z0_PE = 18.1e6;             % 36 Y-Cut Lithium Niobate ~ 34.13e6
Za_PE = Z0_PE * A;
Rs = 50;                    % Source impedance on the transmit
    side [Ohm]
Rl = 50;                    % Load Impedance on the receive side
    [Ohm]

%% Calculations based on ABCD matrix
Gamma_PE(1,1:length(w)) = alpha_PE + j.*(w(1,:))./vL_PE;
Gamma_Backing_Layer(1,1:length(w)) = alpha_Backing_Layer + j.*(w
    (1,:))./vL_Backing_Layer;
Gamma_Cond_Layer(1,1:length(w)) = alpha_Cond_Layer + j.*(w(1,:))
    ./vL_Cond_Layer;
Gamma_Matching_Layer_1(1,1:length(w)) = alpha_Matching_Layer_1 +
    j.*(w(1,:))./vL_Matching_Layer_1;
Gamma_Matching_Layer_2(1,1:length(w)) = alpha_Matching_Layer_2 +
    j.*(w(1,:))./vL_Matching_Layer_2;
```

```
Gamma_Matching_Layer_3(1,1:length(w)) = alpha_Matching_Layer_3 +
    j.*(w(1,:))./vL_Matching_Layer_3;

for i = 1 : length(w)
    C_prime(1,i) = - (CS0/kt_square_PE) * (PI*w(1,i)/w0)/sin(PI*w
        (1,i)/w0);
    Phi_PE2(1,i) = sqrt(kt_square_PE) * sqrt(PI/(w0*CS0*Za_PE)) *
         sin(PI*w(1,i)/(2*w0))/(PI*w(1,i)/(2*w0));
    tmp = (w(1,i)*CS0);
    A_C0(:,:,i) = [1 ((1/(j*tmp))+(tan_sigma_PE*(1/tmp))); 0 1];
    A_C_prime(:,:,i) = [1 1/(j*w(1,i).*C_prime(1,i)); 0 1];
    A_xf(:,:,i) = [Phi_PE2(1,i) 0; 0 1/Phi_PE2(1,i)];
    A_T(:,:,i) = [cosh(Gamma_PE(1,i)*PE_t/2) Za_PE*sinh(Gamma_PE
        (1,i)*PE_t/2); sinh(Gamma_PE(1,i)*PE_t/2)/Za_PE cosh(
        Gamma_PE(1,i)*PE_t/2)];
    A_B(:,:,i) = [cosh(Gamma_Backing_Layer(1,i)*Backing_Layer_t)
        Z0_Backing_Layer*A*sinh(Gamma_Backing_Layer(1,i)*
        Backing_Layer_t); sinh(Gamma_Backing_Layer(1,i)*
        Backing_Layer_t)/(Z0_Backing_Layer*A) cosh(
        Gamma_Backing_Layer(1,i)*Backing_Layer_t)];
    A_M1(:,:,i) = [cosh(Gamma_Matching_Layer_1(1,i)*
        Matching_Layer_t_1) Z0_Matching_Layer_1*A*sinh(
        Gamma_Matching_Layer_1(1,i)*Matching_Layer_t_1); sinh(
        Gamma_Matching_Layer_1(1,i)*Matching_Layer_t_1)/(
        Z0_Matching_Layer_1*A) cosh(Gamma_Matching_Layer_1(1,i)*
        Matching_Layer_t_1)];
    A_M2(:,:,i) = [cosh(Gamma_Matching_Layer_2(1,i)*
        Matching_Layer_t_2) Z0_Matching_Layer_2*A*sinh(
        Gamma_Matching_Layer_2(1,i)*Matching_Layer_t_2); sinh(
        Gamma_Matching_Layer_2(1,i)*Matching_Layer_t_2)/(
        Z0_Matching_Layer_2*A) cosh(Gamma_Matching_Layer_2(1,i)*
        Matching_Layer_t_2)];
    A_M3(:,:,i) = [cosh(Gamma_Matching_Layer_3(1,i)*
        Matching_Layer_t_3) Z0_Matching_Layer_3*A*sinh(
        Gamma_Matching_Layer_3(1,i)*Matching_Layer_t_3); sinh(
        Gamma_Matching_Layer_3(1,i)*Matching_Layer_t_3)/(
        Z0_Matching_Layer_3*A) cosh(Gamma_Matching_Layer_3(1,i)*
        Matching_Layer_t_3)];
    A_Cond(:,:,i) = [cosh(Gamma_Cond_Layer(1,i)*Cond_Layer_t)
        Z0_Cond_Layer*A*sinh(Gamma_Cond_Layer(1,i)*Cond_Layer_t);
        sinh(Gamma_Cond_Layer(1,i)*Cond_Layer_t)/(Z0_Cond_Layer*A)
         cosh(Gamma_Cond_Layer(1,i)*Cond_Layer_t)];
    A_Q(:,:,i) = A_T(:,:,i)*A_Cond(:,:,i)*A_B(:,:,i)*[1 0; 1/(A*
        Z0_Medium_Back(1,i)) 1];
    A_P(:,:,i) = [1 0; A_Q(2,1,i)/A_Q(1,1,i) 1];
    A_C_Par(:,:,i) = [1 0; (j*w(1,i)*C_Par) 1];
```

```
    A_Tx(:,:,i) = A_C_Par(:,:,i) * A_C0(:,:,i) * A_C_prime(:,:,i)
        * A_xf(:,:,i) * A_P(:,:,i) * A_T(:,:,i) * A_Cond(:,:,i) *
        A_M1(:,:,i) * A_M2(:,:,i) * A_M3(:,:,i) * [1 0; 1/(A*
       Z0_Medium_Front(1,i)) 1];
    Z_in_Tx(1,i) = A_Tx(1,1,i) / A_Tx(2,1,i);
    A_Tx_Prime(:,:,i) = [1 Rs; 0 1] * A_Tx(:,:,i);
    H_Tx_F2_Vs(1,i) = 1 / A_Tx_Prime(1,1,i);
    A_Rx(:,:,i) = [1 (A*Z0_Medium_Front(1,i)); 0 1] * A_M3(:,:,i)
        * A_M2(:,:,i) * A_M1(:,:,i) * A_Cond(:,:,i) * A_T(:,:,i)
       * A_P(:,:,i) * (A_xf(:,:,i))^-1 * A_C_prime(:,:,i) * A_C0
       (:,:,i);
    A_Rx_Prime(:,:,i) = A_Rx(:,:,i) * [1 0; 1/Rl 1];
    H_Rx_Vr_2F2(1,i) = 2 * 1 / A_Rx_Prime(1,1,i);
    H_Vr_Vs(1,i) = H_Rx_Vr_2F2(1,i) * H_Tx_F2_Vs(1,i);
end

%% Plotting the results
figure(1); hold on; title("Input Impedance");
xlabel("Frequency (MHz)");
ylabel("Impedance Mag.(\Omega)");
plot(f./1e6, abs(Z_in_Tx), 'k', 'linewidth', 1.5)
xlim([1 40]);
ax = gca;
ax.XGrid = 'off';
ax.YGrid = 'on';
set(gca,'Fontsize',20);
yyaxis right
plot(f./1e6, (angle(Z_in_Tx)/PI).*180, 'b', 'linewidth', 1.5);
ylabel("Impedance Phase(\circ)");
set(gca,'Fontsize',20);

figure(3); hold on; title("Impulse Response Spectrum (H(f) : V-RX
     / V-TX)");
xlabel("Frequency (MHz)");
ylabel("Magnitude(dB)");
max_IR_dB = 20*log10(max(abs(H_Vr_Vs)))
IR_dB = 20.*log10(abs(H_Vr_Vs)./max(abs(H_Vr_Vs)));
f_6dB_LB = f(diff(round(IR_dB + 6) == 0)==1);
f_6dB_HB = f(diff(round(IR_dB + 6) == 0)==-1);
f_6dB = ((f_6dB_HB + f_6dB_LB) ./ 2) ./ 1e6;
fc = mean(f_6dB(1:2))
BW_6dB = ((f_6dB(2) - f_6dB(1)) / fc ) * 100
plot(f./1e6, IR_dB, 'r', 'linewidth', 2.5);
hold on;
line([f_6dB(1) f_6dB(1)], [-80 0], 'Color', 'b', 'LineStyle', '--
   ', 'linewidth', 1);
```

```
line([f_6dB(2) f_6dB(2)], [-80 0], 'Color', 'b', 'LineStyle', '--
   ', 'linewidth', 1);
line([0 f(end)./1e6], [-6 -6], 'Color', 'b', 'LineStyle', '--', '
   linewidth', 1);
line([fc fc], [-80 0], 'Color', 'g', 'LineStyle', '-.', '
   linewidth', 1);
ylim([-40 0]);
xlim([0 40]);
set(gca,'Fontsize',20);
```

Appendix B: uFORCES and FORCES Imaging Shcemes

The simplified MATLAB scripts are written for uFORCES and FORCES imaging scheme simulations on Filed II. The first script calculates the parameters, executes the filed simulation on the CPU's multithreaded, and saves the raw data on a predefined location on the hard drive. Similarly, the second script reads the raw data from the hard disk and performs the beamforming again using the CPU's multi threads. The updated scripts and necessary functions can be found ***Here***.

```
clear all;
close all;
clc;

CurrentFolder = pwd;

addpath(CurrentFolder,'field_II\m_files');  % location of stored
   Filed II m-files

filename = "C:\TEMP\";       % the raw data will be stored here
   generated by each CPU's thread
% ----------------------------    Parameters:
Trans.f0 = 10e6;
Trans.Tx_Freq = 10e6;
Trans.Tx_NCycles = 2;
Trans.fs = 200e6;
Trans.Freq_Att = 0.5*100/1e6;    %Freq dependent att. dB/(m Hz)
Trans.Att_centerfreq = 3e6;   %3 MHZ
Trans.Use_Att = 0;       %1=YES , 0=NO
Trans.IR_Mode = 'Gaussian';
Trans.BW = 0.7;      %Only with Gaussian beam
Trans.c = 1540;
Trans.Nelem_X = 128;     %Rx Side (X-Axis)
Trans.Nelem_Y = 128;     %Tx Side (Y-Axis)
Trans.Lambda = Trans.c / Trans.f0;
```

```
Trans.Elem_Width = 130e-6;
Trans.Elem_Kerf = 20e-6;
Trans.Apod_Mode = 'Off';     %Off = all 1, 2D = 2way Apod, 1D = 1
    Way apod,
Trans.Apod_FlatSize = 60;    %or 86

Sim.Mode = 'uFORCES8';     %uFORCES8 , uFORCES16, and FORCES
Sim.Phnt_Type = 'Cyst';
Sim.Phnt_SplitN = 5;     %Splits the phnatom into smaller phantoms
    .
% So each core can process a small portion of that. rem(number of
% pnts,Phnt_SplitN) must be zero.
Sim.Phnt_Filename = [CurrentFolder,'\PSF_15pnts.mat']; %location
    of phantom file
Sim.Tx_Array = '2D';
Sim.Rx_Array = '1D';      %1D for fast simulation, 2D for preciese
     but slow
Sim.Tx_Elev_Focus = [30e-3];
Sim.Tx_Steering = [0];     % Steering angle - not implemented yet!
Sim.N_PU = 4;   %number of Processing Unit (PU) for parfor;

% ------------------------------ Calculations:
switch Sim.Mode
    case 'FORCES'
        Sim.N_Tx = Trans.Nelem_X;
        Sim.Tx_Elem = 1:Trans.Nelem_X;
        Sim.Tx_Pattern = hadamard(Sim.N_Tx);
    case 'uFORCES8'
        Sim.N_Tx = 8;
        Sim.Tx_Elem = round(linspace(1,Trans.Nelem_X,7));
        Apo_mat = zeros(Sim.N_Tx,Trans.Nelem_X);
        H = hadamard(Sim.N_Tx);
        for pattern = 1:Sim.N_Tx
            Apo_mat(pattern,:) = H(pattern,Sim.N_Tx);
            for i = 1 : (Sim.N_Tx-1)
                Apo_mat(pattern,Sim.Tx_Elem(i)) = H(pattern,i);
            end
        end
        Sim.Tx_Pattern = Apo_mat;
        clear H Apo_mat i pattern;
    case 'uFORCES16'
        Sim.N_Tx = 16;
        Sim.Tx_Elem = round(linspace(1,Trans.Nelem_X,15));
        Apo_mat = zeros(Sim.N_Tx,Trans.Nelem_X);
        H = hadamard(Sim.N_Tx);
        for pattern = 1:Sim.N_Tx
            Apo_mat(pattern,:) = H(pattern,Sim.N_Tx);
```

```
            for i = 1 : (Sim.N_Tx-1)
                Apo_mat(pattern,Sim.Tx_Elem(i)) = H(pattern,i);
            end
        end
        Sim.Tx_Pattern = Apo_mat;
        clear H Apo_mat i pattern;
    otherwise
        disp('Tx Pattern ERROR!');
end

Sim.Total_N_Event = 0;

for i = 1 : max(size(Sim.Tx_Steering))
    for j = 1 : max(size(Sim.Tx_Elev_Focus))
        for k = 1 : Sim.N_Tx
            for l = 1 : Sim.Phnt_SplitN
                Sim.Total_N_Event = Sim.Total_N_Event + 1;
                Sim.Tx_Events(Sim.Total_N_Event, 1) = k;     %
                    pattern no
                Sim.Tx_Events(Sim.Total_N_Event, 2) = Sim.
                    Tx_Elev_Focus(j); %focus
                Sim.Tx_Events(Sim.Total_N_Event, 3) = Sim.
                    Tx_Steering(i);   %steering
                Sim.Tx_Events(Sim.Total_N_Event, 4) = l;     %
                    small portion of the phantom
            end
        end
    end
end

%  Define the impulse response of the transducer
tc = gauspuls('cutoff',Trans.f0,Trans.BW,[],-40);
Trans.IR1 = gauspuls((-tc : 1/Trans.fs : tc), Trans.f0, Trans.BW)
    ;

Trans.IR2 = sin(2*pi*Trans.f0*(0:1/Trans.fs:2/Trans.f0));
Trans.IR2 = Trans.IR2 .* hanning(max(size(Trans.IR2)))';

Trans.Tx_Excitation = sin(2*pi*Trans.Tx_Freq*(0:1/Trans.fs:Trans.
    Tx_NCycles/Trans.Tx_Freq));

switch Trans.Apod_Mode
    case 'Off'
        Trans.Tx_Apod = ones(Trans.Nelem_X, Trans.Nelem_Y);
        Trans.Rx_Apod = Trans.Tx_Apod;
    case '2D'
        switch Trans.Apod_FlatSize
```

```
            case 60
                Trans.Tx_Apod = hamming(68)';
                Trans.Tx_Apod = [Trans.Tx_Apod(1:34), ones(1,60),
                    Trans.Tx_Apod(35:end)];
                Trans.Tx_Apod = Trans.Tx_Apod .* Trans.Tx_Apod';
                Trans.Rx_Apod = Trans.Tx_Apod;
            case 86
                Trans.Tx_Apod = hamming(42)';
                Trans.Tx_Apod = [Trans.Tx_Apod(1:21), ones(1,86),
                    Trans.Tx_Apod(22:end)];
                Trans.Tx_Apod = Trans.Tx_Apod .* Trans.Tx_Apod';
                Trans.Rx_Apod = Trans.Tx_Apod;
            otherwise
                disp('Apod ERROR!');
        end
    case '1D'
        switch Trans.Apod_FlatSize
            case 60
                Trans.Tx_Apod = hanning(68)';
                Trans.Tx_Apod = [Trans.Tx_Apod(1:34), ones(1,60),
                    Trans.Tx_Apod(35:end)]';
                Trans.Tx_Apod = repmat(Trans.Tx_Apod,1,Trans.
                   Nelem_X);
                Trans.Rx_Apod = Trans.Tx_Apod';
            case 86
                Trans.Tx_Apod = hamming(42)';
                Trans.Tx_Apod = [Trans.Tx_Apod(1:21), ones(1,86),
                    Trans.Tx_Apod(22:end)]';
                Trans.Tx_Apod = repmat(Trans.Tx_Apod,1,Trans.
                   Nelem_X);
                Trans.Rx_Apod = Trans.Tx_Apod';
            otherwise
                disp('Apod ERROR!');
        end
    otherwise
        disp('Apod ERROR!');
end


figure(1);
x1 = fft(Trans.IR1,2000);
x1 = abs(x1(1:1001));
x2 = fft(Trans.IR2,2000);
x2 = abs(x2(1:1001));
x1 = x1 ./ max(x1(:));
x2 = x2 ./ max(x2(:));
f = linspace(0,Trans.fs/2/1e6,1001);
```

```
subplot(2,2,1); plot(Trans.IR1,'r'); hold on;
subplot(2,2,1); plot(Trans.IR2,'b'); hold on;
subplot(2,2,1); plot(Trans.Tx_Excitation,'g'); hold on;
legend('Gaussian Wave', '2*sin*hann', 'Excitation Wave');
subplot(2,2,2); plot(f,20*log10(x1),'r'); hold on;
subplot(2,2,2); plot(f,20*log10(x2),'b'); hold on;
legend('Gaussian Wave', '2*sin*hann');
ylim([-20 0]);

subplot(2,2,3); pcolor(Trans.Tx_Apod'); axis image; colorbar;
title('Tx Apod'); caxis([0 1]);
colormap jet; xlabel('X-Axis (# elem.)'); ylabel('Y-Axis (# elem
    .)');
subplot(2,2,4); pcolor(Trans.Rx_Apod'); axis image; colorbar;
title('Tx Apod'); caxis([0 1]);
colormap jet; xlabel('X-Axis (# elem.)'); ylabel('Y-Axis (# elem
    .)');

pause(0.1);

switch Sim.Phnt_Type
    case 'Cyst'
        load (char(Sim.Phnt_Filename));
        if Sim.Phnt_SplitN == 1
            Sim.Phnt_Pos = pos;
            Sim.Phnt_Amp = amp;
        else
            tmp = size(pos,1);
            tmp = round(tmp / Sim.Phnt_SplitN);
            for i = 0 : Sim.Phnt_SplitN-1
                Sim.Phnt_Pos(i+1,:,:) = pos(i*tmp+1:(i+1)*tmp,:);
                Sim.Phnt_Amp(i+1,:,:) = amp(i*tmp+1:(i+1)*tmp,:);
            end
        end

    otherwise
        disp('Phantom ERROR!');
end

if ~exist(filename, 'dir')
    mkdir(filename);
end
save([char(filename) 'Variables'],"Trans","Sim");
pause(0.1);

start_time = tic;
```

```
if Sim.N_PU == 1
    for Tx_Event = 1 : Sim.Total_N_Event

        Fieldii_Calculations_MohammadSobhani(filename,Tx_Event);

    end
elseif Sim.N_PU > 1
    p = parpool(parallel.defaultClusterProfile,Sim.N_PU);
    parfor Tx_Event = 1 : Sim.Total_N_Event

        Fieldii_Calculations_MohammadSobhani(filename,Tx_Event);

    end
else
    disp('Parallel Pool ERROR!');
end

total_time = toc(start_time);

if Sim.N_PU > 1
    delete(p);
end
```

Beamforming code that reads the previously generated raw data and performs delay-and-sum (DAS) operation to form a 2D image:

```
clear all;
close all;
clc;

filename = "C:\TEMP\";
load([char(filename) 'Variables']);

% ------------------------------   Parameters:
BF.noCores = 6;          % Number of phycical cores for speeding
    up the BF
BF.Accuracy = 'Approx';         % Approx , 'Precise' has not
    implemented yet.
BF.planeName = 'XZ';             %XZ and 'YZ' has not implemented
    yet.
BF.planeLoc = 0;
BF.noLines_lateral = 401;    % each core will calculate one line
    of the 2D image
BF.lateralSpan = 10e-3;
BF.lateralLines = linspace(-BF.lateralSpan,BF.lateralSpan,BF.
    noLines_lateral);
BF.noLines_axial = 1501;
```

```
BF.axialMin = 10e-3;
BF.axialMax = 40e-3;
BF.axialLines = linspace(BF.axialMin,BF.axialMax,BF.noLines_axial
    );
BF.noise = 0;
BF.c = Trans.c;
BF.fs = Trans.fs;

% ----------------------------------------- Calculations:
if Sim.Phnt_SplitN > 1
    for i = 1 : size(Sim.Phnt_Pos,1)
        Rmax(i) = max(sqrt(Sim.Phnt_Pos(i,:,1).^2 + Sim.Phnt_Pos(
            i,:,2).^2  + Sim.Phnt_Pos(i,:,3).^2));
    end
elseif Sim.Phnt_SplitN == 1
    for i = 1 : size(Sim.Phnt_Pos,1)
        Rmax(i) = max(sqrt(Sim.Phnt_Pos(i,1).^2 + Sim.Phnt_Pos(i
            ,2).^2  + Sim.Phnt_Pos(i,3).^2));
    end
end
Rmax = max(Rmax(:)) + (sqrt(2)*max(Trans.Nelem_X,Trans.Nelem_Y)*(
    Trans.Elem_Kerf+Trans.Elem_Width));
Tmax = 2*Rmax / Trans.c;
Smin = 1;
Smax = ceil(Tmax * Trans.fs);
clear Tmax Rmax;

pitch = Trans.Elem_Width+Trans.Elem_Kerf;
BF.TransPos_X = linspace(-((Trans.Nelem_X/2)*(pitch)) + pitch
    /2,((Trans.Nelem_X/2)*(pitch)) - pitch/2,Trans.Nelem_X); %
    calculates x- center positions of columns
BF.TransPos_Y = linspace(-((Trans.Nelem_Y/2)*(pitch)) + pitch
    /2,((Trans.Nelem_Y/2)*(pitch)) - pitch/2,Trans.Nelem_Y); %
    calculates y- center positions of columns

if ~exist([char(filename) 'Scat_All.mat'], 'file')
    fprintf('Generating and storing the "Scat_All.mat" file ...')
        ;
    Scat_Temp = zeros(Smax,Trans.Nelem_X);
    Scat_All = zeros(Smax,Trans.Nelem_X,Sim.N_Tx);
    for i = 1 : Sim.N_Tx
        for j = 1 : Sim.Phnt_SplitN
            counter = ((i-1)*Sim.Phnt_SplitN) + j;
            load([char(filename) 'Tx_Event_' num2str(counter)]);
            start_sample = floor(start_time * Trans.fs + 0.5);
            if start_sample < 2
                start_sample = 2;
```

```
            end
            end_sample = start_sample + size(scat,1)-1;
            Scat_Temp = Scat_Temp + [zeros(start_sample - Smin,
               Trans.Nelem_X); scat; zeros(Smax - end_sample,
               Trans.Nelem_X)];
            clear scat start_time;
        end
        Scat_All(:,:,i) = Scat_Temp;
        Scat_Temp = zeros(Smax,Trans.Nelem_X);
    end
    save([char(filename) 'Scat_All'],"Scat_All");
    fprintf(' Done!\n');
else
    fprintf('Loading "Scat_All.mat" file ...');
    load([char(filename) 'Scat_All']);
    fprintf(' Done!\n');

end

scat_tmp = reshape(Scat_All, size(Scat_All,1) * Trans.Nelem_X,
   Sim.N_Tx);

switch Sim.Mode
    case 'FORCES'
        H = hadamard(Sim.N_Tx);
        Decoded_Scat = scat_tmp/H';
    case 'uFORCES8'
        H = hadamard(Sim.N_Tx);
        Decoded_Scat = scat_tmp/H';
    case 'uFORCES16'
        H = hadamard(Sim.N_Tx);
        Decoded_Scat = scat_tmp/H';
end
RF_Data = reshape(Decoded_Scat,size(Scat_All,1),Trans.Nelem_X,Sim
   .N_Tx);
if ~exist([char(filename) 'RF_Data.mat'], 'file')
    fprintf('Saving the decoded data and BF params in "BF_Params.
       mat" file ...')
    save([char(filename) 'BF_Params'],"RF_Data", "BF");
    fprintf(' Done!\n');
end

clear Decoded_Scat H i pitch RF_Data scat_tmp Scat_All;
clear Smin Smax;

if BF.noCores == 1
    for BF_Line = 1 : BF.noLines_lateral
```

```
        DAS_BF_MohammadSobhani(filename, BF_Line);
    end
elseif BF.noCores > 1
    p = parpool(parallel.defaultClusterProfile,BF.noCores);
    parfor BF_Line = 1 : BF.noLines_lateral
        DAS_BF_MohammadSobhani(filename, BF_Line);
    end
else
    disp('Parallel Pool ERROR!');
end

BF_Image = zeros(BF.noLines_axial,BF.noLines_lateral);
for BF_Line = 1 : BF.noLines_lateral
    load ([char(filename) 'BF_Line_' num2str(BF_Line)]);
    BF_Image(:,BF_Line) = A_Scan;
    clear A_Scan;
end

BF_Image = BF_Image ./ max(BF_Image(:));
lateral = linspace(-BF.lateralSpan,BF.lateralSpan,BF.
   noLines_lateral);
axial = linspace(BF.axialMin,BF.axialMax,BF.noLines_axial);
imagesc(lateral.*1e3,axial.*1e3,20*log10(BF_Image));
caxis([-60 0]);
axis image;
colormap gray;
colorbar;

if BF.noCores > 1
    delete(p);
end
```